

APPLIED COMPUTATIONAL ELECTROMAGNETICS SOCIETY JOURNAL

**Special Issue on Antennas, Metasurfaces,
and Testing Methodologies for 5G/6G
Communication - Part II**

Guest Editor:

Yingsong Li, Harbin Engineering University

January 2023

Vol. 38 No. 1

ISSN 1054-4887

The ACES Journal is abstracted in INSPEC, in Engineering Index, DTIC, Science Citation Index Expanded, the Research Alert, and to Current Contents/Engineering, Computing & Technology.

The illustrations on the front cover have been obtained from the ARC research group at the Department of Electrical Engineering, Colorado School of Mines

Published, sold and distributed by: River Publishers, Alsbjergvej 10, 9260 Gistrup, Denmark

THE APPLIED COMPUTATIONAL ELECTROMAGNETICS SOCIETY

<http://aces-society.org>

EDITORS-IN-CHIEF

Atef Elsherbeni
Colorado School of Mines, EE Dept.
Golden, CO 80401, USA

Sami Barmada
University of Pisa, ESE Dept.
56122 Pisa, Italy

ASSOCIATE EDITORS

Maokun Li
Tsinghua University
Beijing 100084, China

Wei-Chung Weng
National Chi Nan University, EE Dept.
Puli, Nantou 54561, Taiwan

Paolo Mezzanotte
University of Perugia
I-06125 Perugia, Italy

Mauro Parise
University Campus Bio-Medico of Rome
00128 Rome, Italy

Alessandro Formisano
Seconda Università di Napoli
81031 CE, Italy

Luca Di Rienzo
Politecnico di Milano
20133 Milano, Italy

Yingsong Li
Harbin Engineering University
Harbin 150001, China

Piotr Gas
AGH University of Science and Technology
30-059 Krakow, Poland

Lei Zhao
Jiangsu Normal University
Jiangsu 221116, China

Riyadh Mansoor
Al-Muthanna University
Samawa, Al-Muthanna, Iraq

Long Li
Xidian University
Shaanxi, 710071, China

Sima Noghianian
Commscope
Sunnyvale, CA 94089, USA

Lijun Jiang
University of Hong Kong, EEE Dept.
Hong Kong

Steve J. Weiss
US Army Research Laboratory
Adelphi Laboratory Center (RDRL-SER-M)
Adelphi, MD 20783, USA

Nunzia Fontana
University of Pisa
56122 Pisa, Italy

Shinishihiro Ohnuki
Nihon University
Tokyo, Japan

Jiming Song
Iowa State University, ECE Dept.
Ames, IA 50011, USA

Stefano Selleri
DINFO - University of Florence
50139 Florence, Italy

Kubilay Sertel
The Ohio State University
Columbus, OH 43210, USA

Toni Bjorninen
Tampere University
Tampere, 33100, Finland

Yu Mao Wu
Fudan University
Shanghai 200433, China

Giulio Antonini
University of L'Aquila
67040 L'Aquila, Italy

Santanu Kumar Behera
National Institute of Technology
Rourkela-769008, India

Fatih Kaburcuk
Sivas Cumhuriyet University
Sivas 58140, Turkey

Antonio Musolino
University of Pisa
56126 Pisa, Italy

Daniele Romano
University of L'Aquila
67100 L'Aquila, Italy

Huseyin Savci
Istanbul Medipol University
34810 Beykoz, Istanbul

Abdul A. Arkadan
Colorado School of Mines, EE Dept.
Golden, CO 80401, USA

Alireza Baghai-Wadji
University of Cape Town
Cape Town, 7701, South Africa

Zhixiang Huang
Anhui University
China

Salvatore Campione
Sandia National Laboratories
Albuquerque, NM 87185, USA

Marco Arjona López
La Laguna Institute of Technology
Torreon, Coahuila 27266, Mexico

Amin Kargar Behbahani
Florida International University
Miami, FL 33174, USA

Ibrahim Mahariq
American University of the Middle East
Kuwait and University of
Turkish Aeronautical Association
Turkey

Kaikai Xu
University of Electronic Science
and Technology of China
China

Laila Marzall
University of Colorado, Boulder
Boulder, CO 80309, USA

EDITORIAL ASSISTANTS

Matthew J. Inman
University of Mississippi, EE Dept.
University, MS 38677, USA

Shanell Lopez
Colorado School of Mines, EE Dept.
Golden, CO 80401, USA

EMERITUS EDITORS-IN-CHIEF

Duncan C. Baker
EE Dept. U. of Pretoria
0002 Pretoria, South Africa

Allen Glisson
University of Mississippi, EE Dept.
University, MS 38677, USA

Ahmed Kishk
Concordia University, ECS Dept.
Montreal, QC H3G 1M8, Canada

Robert M. Bevensee
Box 812
Alamo, CA 94507-0516

Ozlem Kilic
Catholic University of America
Washington, DC 20064, USA

David E. Stein
USAF Scientific Advisory Board
Washington, DC 20330, USA

EMERITUS ASSOCIATE EDITORS

Yasushi Kanai
Niigata Inst. of Technology
Kashiwazaki, Japan

Mohamed Abouzahra
MIT Lincoln Laboratory
Lexington, MA, USA

Alexander Yakovlev
University of Mississippi, EE Dept.
University, MS 38677, USA

Levent Gurel
Bilkent University
Ankara, Turkey

Sami Barmada
University of Pisa, ESE Dept.
56122 Pisa, Italy

Ozlem Kilic
Catholic University of America
Washington, DC 20064, USA

Erdem Topsakal
Mississippi State University, EE Dept.
Mississippi State, MS 39762, USA

Alistair Duffy
De Montfort University
Leicester, UK

Fan Yang
Tsinghua University, EE Dept.
Beijing 100084, China

Rocco Rizzo
University of Pisa
56123 Pisa, Italy

Atif Shamim
King Abdullah University of Science and
Technology (KAUST)
Thuwal 23955, Saudi Arabia

William O'Keefe Coburn
US Army Research Laboratory
Adelphi, MD 20783, USA

Mohammed Hadi
Kuwait University, EE Dept.
Safat, Kuwait

Amedeo Capozzoli
Univerita di Naoli Federico II, DIETI
I-80125 Napoli, Italy

Wenxing Li
Harbin Engineering University
Harbin 150001, China

Qiang Ren
Beihang University
Beijing 100191, China

EMERITUS EDITORIAL ASSISTANTS

Khaleb ElMaghoub
Trimble Navigation/MIT
Boston, MA 02125, USA

Kyle Patel
Colorado School of Mines, EE Dept.
Golden, CO 80401, USA

Christina Bonnington
University of Mississippi, EE Dept.
University, MS 38677, USA

Anne Graham
University of Mississippi, EE Dept.
University, MS 38677, USA

Madison Lee
Colorado School of Mines, EE Dept.
Golen, CO 80401, USA

Allison Tanner
Colorado School of Mines, EE Dept.
Golden, CO 80401, USA

Mohamed Al Sharkawy
Arab Academy for Science and Technology, ECE Dept.
Alexandria, Egypt

TABLE OF CONTENTS

Research on OTA Testing Optimization of 5G IoT Devices
Xiaochen Chen, Xianhui Liu, and Siyang Sun 1

Experimental Investigation of Decoupling Effect on the Nonlinearity of Power Amplifiers in Transmitter Array
Fangyun Peng, Fei Yang, Bo Liu, and Xiaoming Chen 7

A Hybrid EMC Testing Facility: Combining Transmission Line and Reverberation Chamber Measurement System
Kai Chen, Wenjun Qi, Peng Peng, Hailong Wang, Xueqi Shen, Yongjiu Zhao, and Qian Xu 15

Reducing the Measurement Time in a Reverberation Chamber to Less than 1 Second
Wenjun Xia, Wenjun Qi, Feng Fang, Chong Li, Lei Xing, and Qian Xu 22

Uncertainty Quantification Method of Crosstalk Involving Braided-Shielded Cable
Tianhong Tan, Tao Jiang, Haolin Jiang, Tianhao Wang, and Mingjuan Cai 28

Recent Developments of Shielding Effectiveness for Electronics and Information Devices
Ping Xu, Tao Jiang, Meiyu Wang, Yingsong Li, and Zhixiang Huang 36

Combined Application of Partition Clustering Classification and Gerchberg-Papoulis Optimization Algorithm for Spherical Near Field Antenna Measurements
Fangyun Peng, Yuchen Ma, Yuxin Ren, Bo Liu, Xiaobo Liu, Zhengpeng Wang, Lei Zhao, Xiaoming Chen, and Zhiqin Wang 45

A Compact Four-way Quadrature Power Splitter for 5G Low-band Applications
Song Gao, Hao Wang, Kwok L. Chung, Yingsong Li, Kangtai Zheng, and Luqi Chen 54

Removing the Froissart Doublets in a Rational Interpolation Based on Loewner Matrix
Haobo Yuan, Jungang Ren, Yujie Li, and Xiaoming Huang 60

Super-Broadband Rectifier with Wide-band Resistance Compression Network and Harmonic Cycling for RF-Harvesting
Xin Liu, Dawei Zhang, Yingsong Li, and Zhixiang Huang 67

Research on OTA Testing Optimization of 5G IoT Devices

Xiaochen Chen, Xianhui Liu, and Siyang Sun

China Telecommunication Technology Labs
China Academy of Information and Communications Technology, Beijing, 100191, China
sunsiyang@caict.ac.cn

Abstract – Over-the-air (OTA) testing for wireless devices is crucial to guarantee actual network performance. Current OTA testing requires respectively 266 and 62 grid points for Total Radiated Power (TRP) and Total Isotropic Sensitivity (TIS) measurement. For 5G Internet of Things (IoT) devices, especially for low transmit duty-cycle devices, this number of grid points could lead to an unacceptably large amount of test time. Therefore, test time reduction is significant. The objective of this paper is to determine a suitable measurement grid for OTA testing of 5G IoT devices which balances measurement grid uncertainty/errors with test time. Two reference patterns representing a reasonable worst-case scenario of IoT devices are proposed for measurement uncertainty (MU) analysis of different grid configurations. The effects of different grid configurations on OTA testing accuracy are evaluated. The determination of associated MU term is proposed and determined based on statistical analysis. Finally, the reduction of grid points from currently required 62 (30/30 in theta/phi) to 32 (45/36) could save roughly 50% test time while requiring an uncertainty increase of less than 0.2 dB, which is acceptable for OTA testing of 5G IoT devices.

Index Terms – 5G IoT, measurement grid, MU analysis, over-the-air (OTA) testing.

I. INTRODUCTION

The Internet of Things (IoT) has become the main force driving evolution of mobile communications towards 2020 and beyond, and will penetrate into all industries and ultimately everyone's daily life. It is expected that the connections of IoT devices will exceed 1 million per square kilometer and 100 billion in total [1–5]. For applications in which global coverage and mobility are major concerns, cellular technologies, especially LTE-M and NB-IoT are preferred technologies. Meanwhile, the majority of devices use non-cellular technologies including Bluetooth, Wi-Fi, ZigBee, EnOcean, SIGFOX, LoRa and others [6–13]. Wireless connection reliability, coverage, response speed and security are factors

which heavily impact quality of experience and system performance, which in turn depends on agile and high-performance antennas. Therefore, OTA testing of the overall communications performance for IoT devices is of great significance [3–4].

OTA testing has been used as the standard method for radiated power and receiver performance evaluations of wireless devices in the 3rd Generation Partnership Project (3GPP) and Cellular Telecommunication and Internet Association (CTIA) [14–18]. Traditional single-input single-output (SISO) OTA testing includes Total Radiated Power (TRP) measurements for radiated power and Total Isotropic Sensitivity (TIS) measurements for sensitivity evaluation, requiring measurement grid resolutions of 15° and 30° respectively, for constant step grid. Typically, it takes around 60 and more than 120 minutes respectively for TRP and TIS measurement for 5G mobile phones. During both TRP and TIS measurements, devices under test (DUTs) are required to operate at maximum transmit power. However, many low-power IoT devices, including smart-watches, parking meters, pet tracking devices, etc., are designed to transmit at full power for only a short interval every hour, and as a result, typically have a very small heatsink for the power amplifier and a relatively low-capacity battery. Additionally, batteries in low-power IoT devices, such as those in smart water meters, often have to last 10 years or more. Therefore, attempts to perform OTA testing by current CTIA and 3GPP specifications for mobile phones will, in many cases, make the DUTs shut themselves off, and even become damaged due to excessive heat. Due to the proliferation of such devices, test time reduction is of great importance for OTA testing of 5G IoT. Unfortunately, no relevant research has been carried out or published.

The objective of this paper is to determine a suitable measurement grid for OTA testing of 5G IoT devices which balances measurement grid uncertainty with test time. This paper compares the effect of different grid configurations on OTA testing accuracy of IoT devices. Two reference patterns representing reasonable worst-case scenarios are proposed to mimic radiation of IoT

DUTs while a variety of different grid configurations are compared through simulations to determine how well they could accurately reconstruct reference patterns. The related MU terms are analyzed and determined based on statistical analysis. As a result, the recommended grid configuration with resolution of 45/36 (theta/phi) for constant step grid is proposed for OTA testing of IoT devices, especially for low-power IoT devices. Compared with currently-required TIS grid in 3GPP/CTIA (30/30), a roughly 50% test time saving can be realized at the expense of an uncertainty relaxation of less than 0.2 dB.

II. APPROACH FOR MEASUREMENT GRID UNCERTAINTY ANALYSIS

For a complete sphere measured with N theta intervals and M phi intervals, both with even angular spacing, TIS can be calculated as follows:

$$TIS \cong \frac{2M}{\sum_{i=0}^N \omega_i \cdot \sum_{j=0}^{M-1} \left[\frac{1}{EIS_{\theta}(\theta_i, \phi_j)} + \frac{1}{EIS_{\phi}(\theta_i, \phi_j)} \right]}, \quad (1)$$

where EIS is the radiated effective isotropic sensitivity measured at each direction and polarization, and ω_i is the weight function. In this research, the Clenshaw-Curtis weights in [19] are used. Considering that TIS requires much more test time than that of TRP, test time reduction for TIS is the first priority. In addition, the research method and its conclusion for TIS also apply to TRP due to reciprocity.

Currently, there are several quick TIS approaches being considered in industry, including the theta-dependent phi optimization [14]; device-reported receive signal strength (RSS) [14, 20–21]; grid point reduction; spiral scan [14]; device rotation during measurement [14]; single or multi-point offset in anechoic chambers and continuous-mode stirring in reverberation chambers [14, 22–25]. Among all of these methods, measurement grid reduction is a more direct and efficient one. It is obvious from (1) that the accuracy for TIS measurement depends highly on the total number and distribution of measurement grid points. The more points, the higher precision, and as a result, the longer test time. For time reduction, a trade-off must be made between accuracy and total number of grid points. Therefore, the effects of different measurement grid configurations on TIS measurement accuracy, and the determination of relevant MU are prerequisite.

In this paper, a variety of grid configurations are simulated to compare how well they could accurately reconstruct the reference patterns and determine the related MUs. Here, reference pattern refers to the worst-case pattern of IoT devices with a reasonable high directivity or narrow beamwidth as well as drastic variations. Two reference patterns are proposed to mimic radiation

of IoT DUTs and the related analysis for different grids are presented in next section.

For MU analysis, the most realistic method is to analyze the statistical distribution of the TIS for a large number of random orientations. Although this can be done experimentally, it requires a large number of independent measurements to achieve statistical significance; considering the total test time needed, it is unrealistic for industry. Therefore, in this research, the related MU analysis is performed through numerical simulations, during which the relative orientation between the reference pattern and the TIS measurement grid is altered randomly and the standard deviation (STD) between TISs for each grid configuration can be derived from a set of 10,000 random orientations. For any given grid configuration, the grid-dependent MU term for TIS testing is determined by the STD of TISs. Considering random rotations of a reference pattern with respect to grids of arbitrary resolutions, it is therefore proposed that analytical expression of radiation patterns may be used as a reference.

The random rotation mentioned here could be achieved by combinations of rotations around x, y, and z axes, as illustrated in Fig. 1. Due to the non-commutative nature of rotations, the order of rotations is important and must be pre-defined when multiple rotations are involved. The following order of rotations has been followed for the reference pattern orientations specified in this research: first, Ψ (rotation around the x axis); second, Θ (rotation around the y axis); last, Φ (rotation around the z axis).

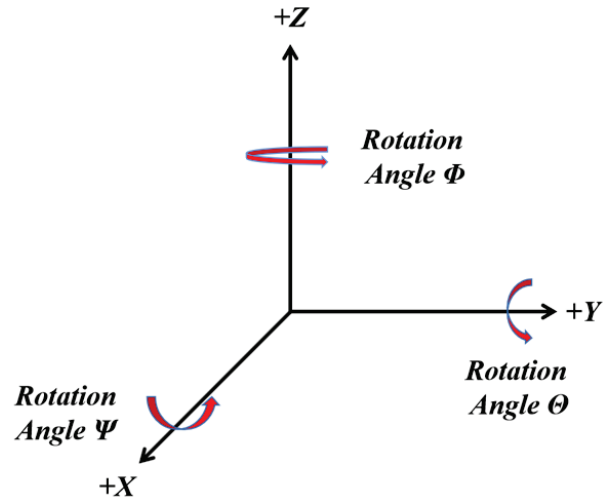


Fig. 1. Rotation angle definitions for random rotation.

III. SIMULATIONS AND ANALYSIS

A. Reference pattern 1

In this scenario, the dipole is adopted as the reference pattern to mimic the radiation property of 5G IoT

DUTs. This arrangement is based on considerations that: (i) for the majority of IoT devices, the radiation properties of installed antennas are similar to that of dipoles; (ii) dipole could provide relatively drastic variations in theta; (iii) the analytical expression of radiation patterns for dipole is available, which is adopted in this simulation as equation (2) and illustrated in Fig. 2:

$$A_E(\theta, \phi) = \left[\frac{\cos\left(\left(\frac{\pi}{2}\right)\cos\theta\right)}{\sin(\theta)} \right]. \quad (2)$$

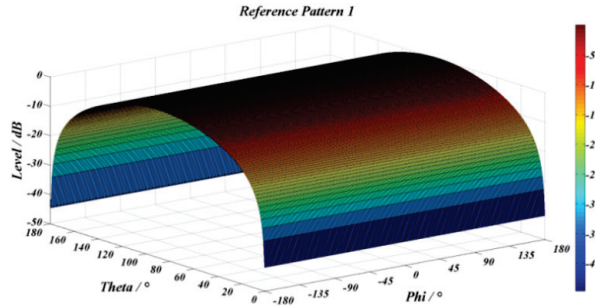


Fig. 2. Illustration of reference pattern 1.

Table 1: Statistical analyses of 10k simulations for reference pattern 1 on different grid configurations

Grids in Theta	Step Size in Theta	Grids in Phi	Step Size in Phi	STD [dB]	Total Number
19	$\Delta\theta=10^\circ$	36	$\Delta\theta=10^\circ$	0.1036	614
12	$\Delta\theta=16.36^\circ$	19	$\Delta\theta=18.95^\circ$	0.2325	192
13	$\Delta\theta=15^\circ$	24	$\Delta\theta=15^\circ$	0.1934	266
13	$\Delta\theta=15^\circ$	12	$\Delta\theta=30^\circ$	0.2507	134
7	$\Delta\theta=30^\circ$	24	$\Delta\theta=15^\circ$	0.2282	122
		12	$\Delta\theta=30^\circ$	0.3396	62
		10	$\Delta\theta=36^\circ$	0.3578	52
		9	$\Delta\theta=40^\circ$	0.4947	47
		8	$\Delta\theta=45^\circ$	0.4044	42
		7	$\Delta\theta=51.4^\circ$	0.5930	37
		6	$\Delta\theta=60^\circ$	0.5129	32
6	$\Delta\theta=36^\circ$	24	$\Delta\theta=15^\circ$	0.2938	98
		12	$\Delta\theta=30^\circ$	0.4726	50
		10	$\Delta\theta=36^\circ$	0.4152	42
		9	$\Delta\theta=40^\circ$	0.6688	38
		8	$\Delta\theta=45^\circ$	0.4937	34
		7	$\Delta\theta=51.4^\circ$	0.5993	30
5	$\Delta\theta=45^\circ$	6	$\Delta\theta=60^\circ$	0.6453	26
		24	$\Delta\theta=15^\circ$	0.3639	74
		12	$\Delta\theta=30^\circ$	0.4277	38
		10	$\Delta\theta=36^\circ$	0.4360	32
		9	$\Delta\theta=40^\circ$	0.6751	29
		8	$\Delta\theta=45^\circ$	0.6205	26
4	$\Delta\theta=60^\circ$	7	$\Delta\theta=51.4^\circ$	0.7247	23
		6	$\Delta\theta=60^\circ$	0.8224	20
		24	$\Delta\theta=15^\circ$	0.6092	50
		12	$\Delta\theta=30^\circ$	0.7202	26
		8	$\Delta\theta=45^\circ$	0.8299	18
		6	$\Delta\theta=60^\circ$	0.8751	14

Based on the settings above, we have performed simulations for different grid configurations, respec-

Table 2: Reference pattern 2

Parametric Description	Equations
Horizontal radiation pattern	$A_{E,H}(\varphi)$ $= -\min\left[12\left(\frac{\varphi}{\varphi_{3dB}}\right)^2, A_m\right] \text{ dB},$ $A_m = 30 \text{ dB}$
Horizontal HPBW	260°
Vertical radiation pattern	$A_{E,V}(\theta)$ $= -\min\left[12\left(\frac{\theta-90}{\theta_{3dB}}\right)^2, SLA_v\right],$ $SLA_v = 30 \text{ dB}$
Vertical HPBW	32.5°
Antenna radiation pattern	$A_E(\varphi, \theta)$ $= G_{E,max} - \min\{-[A_{E,H}(\varphi) + A_{E,V}(\theta)], A_m\}$
Gain without antenna losses	$G_{E,max}=6.8 \text{ dBi}$

tively. The simulated STDs are listed in Table 1 for comparison.

The highlighted grid resolutions of 15/15 (theta/phi) and 30/30 are currently required grid configurations in both 3GPP and CTIA for TRP and TIS measurements of mobile phones, which correspond to STDs of 0.1934 dB and 0.3396 dB, respectively. Based on the comparisons, the following observations can be made:

Observation 1: generally, as the grid resolution decreases, the total number of grid points decreases while the calculated STD increases;

Observation 2: as an exception, asymmetric distribution of grid points in both theta and phi could result in higher STDs, even with more grid points.

B. Reference pattern 2

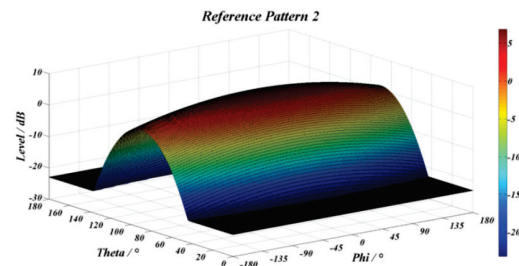


Fig. 3. Illustration of reference pattern 2.

In this scenario, equations from [18] are utilized to generate reference pattern for MU analysis of different grid configurations. The pattern with 260/32.5 HPBW's (Horizontal/Vertical) and peak directivity of around 6.8 dBi is proposed in Table 2 and illustrated in Fig. 3 for reference. This arrangement is based on

considerations that it can provide a reasonably larger directivity (i.e., narrower beamwidth) than that of IoT devices without exaggerating its influence. In addition, this pattern provides less symmetry compared with reference pattern 1.

Table 3: Statistical analyses of 10k simulations for reference pattern 2 on different grid configurations

Grids in Theta	Step Size in Theta	Grids in Phi	Step Size in Phi	STD [dB]	Total Number
19	$\Delta\theta=10^\circ$	36	$\Delta\phi=10^\circ$	2.1315e-04	614
12	$\Delta\theta=16.36^\circ$	19	$\Delta\phi=18.95^\circ$	7.6889e-04	192
13	$\Delta\theta=15^\circ$	24	$\Delta\phi=15^\circ$	5.8576e-04	266
13	$\Delta\theta=15^\circ$	12	$\Delta\phi=30^\circ$	0.0192	134
7	$\Delta\theta=30^\circ$	24	$\Delta\phi=15^\circ$	0.0295	122
		12	$\Delta\phi=30^\circ$	0.0333	62
		10	$\Delta\phi=36^\circ$	0.0867	52
		9	$\Delta\phi=40^\circ$	0.0534	47
		8	$\Delta\phi=45^\circ$	0.2487	42
		7	$\Delta\phi=51.4^\circ$	0.1344	37
		6	$\Delta\phi=60^\circ$	0.7255	32
6	$\Delta\theta=36^\circ$	24	$\Delta\phi=15^\circ$	0.0810	98
		12	$\Delta\phi=30^\circ$	0.0824	50
		10	$\Delta\phi=36^\circ$	0.1187	42
		9	$\Delta\phi=40^\circ$	0.0935	38
		8	$\Delta\phi=45^\circ$	0.2575	34
		7	$\Delta\phi=51.4^\circ$	0.1555	30
		6	$\Delta\phi=60^\circ$	0.7432	26
5	$\Delta\theta=45^\circ$	24	$\Delta\phi=15^\circ$	0.1828	74
		12	$\Delta\phi=30^\circ$	0.1866	38
		10	$\Delta\phi=36^\circ$	0.1972	32
		9	$\Delta\phi=40^\circ$	0.1904	29
		8	$\Delta\phi=45^\circ$	0.3177	26
		7	$\Delta\phi=51.4^\circ$	0.2260	23
		6	$\Delta\phi=60^\circ$	0.7414	20
4	$\Delta\theta=60^\circ$	24	$\Delta\phi=15^\circ$	0.4695	50
		12	$\Delta\phi=30^\circ$	0.4884	26
		8	$\Delta\phi=45^\circ$	0.5623	18
		6	$\Delta\phi=60^\circ$	0.8414	14

The statistical results for different grid configurations with reference pattern 2 are summarized in Table 3. Based on the comparisons, the following observations can be made:

Observation 1: for the same grid configuration, the STDs with reference pattern 2 are much lower than that with reference pattern 1;

Observation 2: the calculated STD increases as the grid resolution decreases, with the exception that the symmetry distribution of grid points in phi could increase the calculated STDs even with more grid points.

In summary, different trends for calculated STDs can be observed between reference patterns. For reference pattern 1, asymmetric distribution of grid points in both theta and phi could result in higher STDs even with more grid points, which is opposite to that of reference pattern 2. This phenomenon can be attributed to difference in symmetry between different patterns. In other words, symmetric distribution of grid points could perform better for symmetric patterns, and vice versa, which can be used as a guideline for grid configuration selection

when performing TIS testing. Compared with the STDs of currently-required 30/30 configuration with both reference patterns, one could also conclude that a proper relaxation in MU is allowed for grid reduction such that the STD is still less than 0.5 dB. Finally, according to the criteria of minimum grid points with STD no more than 0.5 dB, the grid resolution of 45/36 (theta/phi) with a STD of 0.4360 dB is recommended as the reference grid configuration for OTA testing of 5G IoT devices. Compared with currently adopted grid configuration with 62 points, a roughly 50% grid point reduction can be achieved.

IV. CONCLUSIONS

This paper proposes a suitable measurement grid configuration for OTA testing of 5G IoT devices which balances the measurement grid uncertainty with test time. During the research, two radiation patterns representing reasonable worst-case scenarios of IoT devices are proposed as reference to support the analysis of grid configurations. The effects of different grid configurations on OTA testing accuracy are compared while the grid-dependent MU terms for grid configurations are determined based on statistical analysis of the TISs for a large number of random orientations. Based on the proposed criteria, the grid configuration of 45/36 (theta/phi) with a roughly 50% grid point reduction is considered to be optimal for OTA testing of 5G IoT devices.

ACKNOWLEDGMENT

This work was supported by the Key Research and Development Project of Guangdong Province under Grant 2020B0101080001.

REFERENCES

- [1] IMT-2020 (5G) Promotion Group, "White paper on 5G concept," Feb. 2015.
- [2] ITU-R, "Recommendation ITU-R M.2083-0: IMT vision – framework and overall objectives of the future development of IMT for 2020 and beyond," Sep. 2015.
- [3] Y. Qi, G. Yang, L. Liu, J. Fan, A. Orlandi, H. Kong, W. Yu, and Z. Yang, "5G over-the-air measurement challenges: Overview," *IEEE Trans. Electromagn. Compat.*, vol. 59, no. 6, pp. 1661-1670, 2017.
- [4] P. Shen, Y. Qi, W. Yu, J. Fan, and F. Li, "OTA measurement for IoT wireless device performance evaluation: Challenges and solutions," *IEEE Internet Things J.*, vol. 6, no. 1, pp. 1223-1237, 2019.
- [5] Y. Zhang, G. Tian, S. Zhang, and C. Li, "A knowledge-based approach for multiagent collaboration in smart home: From activity recognition to guidance service," *IEEE Trans. Instrum. Meas.*, vol. 69, no. 2, pp. 317-329, 2020.

- [6] L. Chettri and R. Bera, "A comprehensive survey on Internet of Things (IoT) toward 5G wireless systems," *IEEE Internet Things J.*, vol. 7, no. 1, pp. 16-32, 2020.
- [7] K. Shafique, B. A. Khawaja, F. Sabir, S. Qazi, and M. Mustaqim, "Internet of Things (IoT) for next-generation smart systems: A review of current challenges, future trends and prospects for emerging 5G-IoT scenarios," *IEEE Access*, vol. 8, pp. 23022-23040, 2020.
- [8] S. Henry, A. Alsohaily, and E. S. Sousa, "5G is real: Evaluating the compliance of the 3GPP 5G new radio system with the ITU IMT-2020 Requirements," *IEEE Access*, vol. 8, pp. 42828-42840, 2020.
- [9] X. Chen, J. Tang, T. Li, S. Zhu, Y. Ren, Z. Zhang, and A. Zhang, "Reverberation chambers for over-the-air tests: An overview of two decades of research," *IEEE Access*, vol. 6, pp. 49129-49143, 2018.
- [10] H. T. Chattha, M. K. Ishfaq, B. A. Khawaja, A. Sharif, and N. Sheriff, "Compact multiport MIMO antenna system for 5G IoT and cellular handheld applications," *IEEE Antennas Wireless Propag. Lett.*, vol. 20, no. 11, pp. 2136-2140, 2021.
- [11] X. Chen, "Measurement uncertainty of RC and its reduction techniques for OTA tests: A review," *IET Microw. Antennas Propag.*, vol. 13, no. 15, pp. 2598-2604, 2019.
- [12] B. Xiao, H. Wong, D. Wu, and K. L. Yeung, "Design of small multiband full-screen smartwatch antenna for IoT applications," *IEEE Internet Things J.*, vol. 8, no. 24, pp. 17724-17733, 2021.
- [13] R. Rodriguez-Cano and R. W. Ziolkowski, "Single-layer, unidirectional, broadside-radiating planar quadrupole antenna for 5G IoT applications," *IEEE Trans. Antennas Propag.*, vol. 69, no. 9, pp. 5224-5233, 2021.
- [14] CTIA Certification Program, "Test plan for wireless device Over-the-Air performance," V3.9.3, Sep. 2021.
- [15] CTIA Certification Program, "Test plan for 2x2 downlink MIMO and transmit diversity Over-the-Air performance," V1.2.2, Dec. 2021.
- [16] CTIA Certification Program, "Test plan for millimeter-wave wireless device Over-the-Air performance," V1.0.2, Dec. 2020.
- [17] 3GPP, TR 37.977, "Universal Terrestrial Radio Access (UTRA) and Evolved Universal Terrestrial Radio Access (E-UTRA); Verification of radiated multi-antenna reception performance of User Equipment (UE)," V16.0.0, Jun. 2020.
- [18] 3GPP, TR 38.810, "NR; Study on test methods," V16.6.0, Sep. 2019.
- [19] C. W. Clenshaw and A. R. Curtis, "A method for numerical integration on an automatic computer," *Numerische Mathematik*, vol. 2, p. 197-205, 1960.
- [20] P. Shen, Y. Qi, W. Yu, F. Li, and J. Fan, "Fast and accurate TIS testing method for wireless user equipment with RSS reporting," *IEEE Trans. Electromagn. Compat.*, vol. 58, no. 3, pp. 887-895, 2016.
- [21] Y. Qi, P. Jarmuszewski, Q. Zhou, M. Certain, and J. Chen, "An efficient TIS measurement technique based on RSSI for wireless mobile stations," *IEEE Trans. Instrum. Meas.*, vol. 59, no. 9, pp. 2414-2419, 2010.
- [22] F. Li, S. Huang, W. Xue, Y. Ren, and X. Chen, "Signal and coherence bandwidth effects on total radiated power measurements of LTE devices in reverberation chambers," *IEEE Trans. on Instrum. Meas.*, vol. 71, pp. 1-3, 2022.
- [23] W. Xue, F. Li, and X. Chen, "Effects of signal bandwidth on total isotropic sensitivity measurements in reverberation chamber," *IEEE Trans. Instrum. Meas.*, vol. 70, pp. 1-8, 2021.
- [24] CTIA Certification Program, "Test plan for wireless Large-Form-Factor device Over-the-Air performance," V1.2.1, Feb. 2019.
- [25] W. Xue, F. Li, X. Chen, S. Zhu, A. Zhang, and T. Svensson, "A unified approach for uncertainty analyses for total radiated power and total isotropic sensitivity measurements in reverberation chamber," *IEEE Trans. Instrum. Meas.*, vol. 70, pp. 1-12, 2021.



Xiaochen Chen, Senior Engineer, Chinese Leaders of EU FP6 GO4IT, FP7 WALTER, is responsible for several key research projects at the National Development and Reform Commission and the Ministry of Industry and Information Technology. He is responsible for formulating more than 20 domestic and foreign communication standards, applying for/owning 6 patents, and has published more than 20 academic papers. He is now with China Telecommunication Technology Labs, China Academy of Information and Communication Technology.



Xianhui Liu is currently a Senior Engineer with China Telecommunication Technology Labs, China Academy of Information and Communications Technology. He is mainly engaged in 5G OTA testing, MIMO OTA and related technology research.



Siyang Sun is currently an Associate Professor with China Telecommunication Technology Labs, China Academy of Information and Communications Technology. He is mainly engaged in 5G standardization, 5G OTA testing, MIMO OTA and related technology research.

Experimental Investigation of Decoupling Effect on the Nonlinearity of Power Amplifiers in Transmitter Array

Fangyun Peng¹, Fei Yang², Bo Liu¹, and Xiaoming Chen¹

¹School of Information and Communications Engineering
Xi'an Jiaotong University, Xi'an, 710049, China

pfy2014111731@stu.xjtu.edu.cn, liuboright@stu.xjtu.edu.cn, xiaoming.chen@mail.xjtu.edu.cn

²China Academy of Space Technology
Xi'an, 711049, China
yfxjtu@163.com

Abstract – In a practical compact massive multiple-input multiple-output (MIMO) transmitter array, each antenna or subarray is connected to an independent power amplifier (PA) with a modest power capacity in order to avoid the challenging demand of high-power capacity of a single PA for the whole array and to facilitate the power dissipation of the transmitter array. In this case, there is simply not enough space for an isolator between the antenna and the PA. As a result, the array mutual coupling changes the load impedances of the PAs and thus further increases the MIMO transmitter's nonlinearity. In this work, the decoupling effect on the transmitter array's linearity is investigated experimentally by using an array prototype with PAs. The mutual coupling of the array can be effectively suppressed using a hybrid decoupling structure. Two continuous-wave (CW) signals at different frequencies are injected into the PAs, and the output signal of each PA is measured via a coupler. The measured results show that with effective mutual coupling reduction, the PA interference is greatly suppressed by up to 16 db and the amplitude of the desired signal is enhanced by up to 10 db.

Index Terms – mutual coupling, nonlinearity, power amplifier, transmitter array.

I. INTRODUCTION

The massive multi-input multi-output (MIMO) has been one of the key enablers for current and future wireless communications [1], [2]. Reduction of the power consumption and improvement of the transmitter linearity in a massive MIMO system has become a research hotspot. By configuring a large number of channels and antenna elements, the massive MIMO technique brings great performance enhancement, yet also introduces many thorny problems. Among them, the problem of nonlinear distortion of the power amplifiers (PAs) is particularly prominent [3–6]. The PAs are important

modules in a MIMO transmitter array. In a practical MIMO transmitter array, each antenna or subarray is connected with an independent power amplifier (PA) with a modest power capacity instead of using a single PA with high-power capacity to feed the whole array. In this way, the transmitter can be more robust and cost-effective, and the multi-PA scheme also facilitates the power dissipation in the transmitter front-end. Moreover, for a compact massive array, there is not enough space for an isolator between the antenna and the PA. As a result, the mutual couplings between the elements in a MIMO array will change the active port impedance, resulting in mismatch between the antenna and the PA. In the presence of mutual coupling, the outputs of the PAs will interfere with each other, increasing the nonlinearity of the PA.

Figure 1 shows a schematic model of a MIMO transmitter array with PAs. Each element in the array is connected with a PA. The incident wave in the i -th PA ($a_{2,i}$) is dependent on the mutual couplings between antenna elements and the reflected wave in j -th PA ($b_{2,j}$), as mathematically described in (1). In other words, the mutual coupling changes the load impedances of the PAs, resulting in deteriorations of the PA efficiency and linearity.

$$a_{2,i} = \sum_{j=1}^N S_{i,j} b_{2,j}, \quad (1)$$

where the $s_{i,j}$ is the S-parameter between i -th and j -th element.

Various PA behavior models have been proposed to optimize the linearity [7] where the PA parameters are characterized by signal-tone or multi-tone excitation in measurements [8], [9]. A DC behavior was extended to a PA model [5] to predict the linearization and efficiency of PA in the presence of mutual coupling. A 4×1 array with 4 PAs was designed in [6], and the spectral results at the PA output were given to show the spectral regrowth with/without mutual coupling. Nonlinear

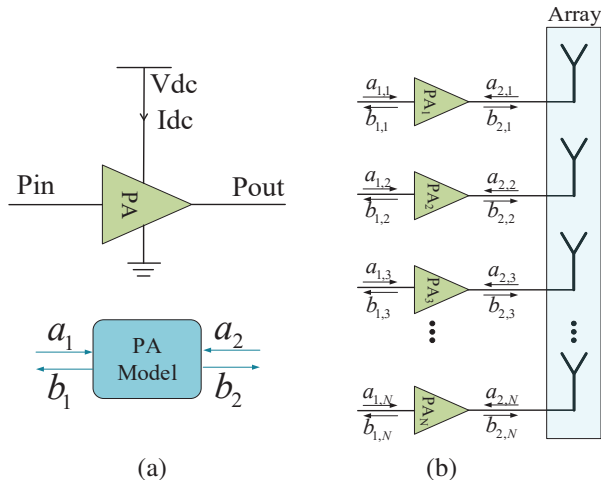


Fig. 1. Schematics of (a) a PA model with incident and reflected waves, and (b) N-element array with PAs.

distortion in phased-array transmitters was investigated in [10], simulated results therein showed that the main beam in-band distortion varies strongly with the steering angle in the presence of mutual coupling. The studies mentioned above only presented or predicted the nonlinear effect of mutual coupling on PA in transmitter arrays, without discussion on how to correct the distortions. A four-branch transmitter prototype was used in [11] to compare the spectrum distortion. It was reported that the regular linearization technique was ineffective to compensate the distortion due to the array mutual coupling. Instead of designing linearization techniques with high complexity, a cost-effective solution is to decouple the array from the antenna point of view. However, the decoupling effect on the linearity of the transmitter array has not been investigated yet.

In this paper, an antenna array prototype with a removable decoupling structure is connected with PAs. The PA output signals with and without array decoupling are measured. The experimental results show that the mutual coupling not only deteriorates the linearity but also creates strong interference. More importantly, it is shown that with effective array decoupling, both interference and spurious signals are greatly suppressed, and the desired signal is enhanced. To the best knowledge of the authors, this is the first experimental work demonstrating the decoupling effect on the linearity of a transmitter array.

II. COUPLING SUPPRESSION IN MIMO ARRAY

The MIMO array used in the test is a 4×4 base station (BS) array with a 57-mm horizontal inter-element spacing ($0.38\lambda_0$, where λ_0 is the free space wavelength at center frequency of 2.0 GHz) and a 117-mm vertical

inter-element spacing ($0.75\lambda_0$). The four dual-polarized elements in each array column are combined using a power divider into one subarray with two antenna ports (for the $\pm 45^\circ$ polarizations), which is a typical BS array configuration.

The array has an operation band of 1.7-2.2 GHz. Due to the close horizontal inter-subarray spacing, the array suffers mutual coupling up to -15 db. Different decoupling techniques have been reported in previous works, e.g., decoupling metasurfaces [12–14], decoupling resonators [15], defected ground structure [16], and dielectric decoupling superstrate [17–19]. In order to increase the decoupling bandwidth, a hybrid decoupling method has been designed to reduce the mutual couplings down to -30 db at the center frequency. Figure 2 shows the coupling wave and decoupling mechanism between a two-element array. As shown in Fig. 2 (b), both the neutralization board and metal baffle are applied to the array. The neutralization board is suspended above the antenna to produce a reflective wave that is opposite in phase to the coupling wave, reducing the mutual coupling between elements. The metal baffle is placed between the two antennas to suppress the propagation of the space electromagnetic wave. Detailed description about the BS array and the decoupling method can be found in [19].

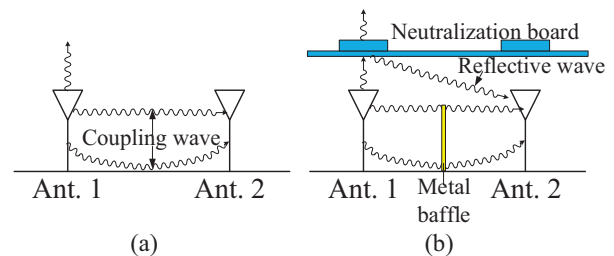


Fig. 2. Coupling wave between two-element array. (a) Array without decoupling and (b) with decoupling.

In order to realize the overall isolation enhancement of the MIMO array, a frequency domain solver based on finite element method (FEM) in an electromagnetic simulator CST 2020 [20] is used to design and optimize the array and decoupling structure. After the optimization of isolation, the array with removable decoupling structures are fabricated, as shown in Fig. 3.

This proposed decoupling method applies the combination of a metal baffle and the neutralization dielectric to the MIMO antenna array, which, compensating the insensitivity of the neutralization method to the cross-polarization coupling [21], significantly broadens the decoupling bandwidth of the compact, large-scale array. Figure 4 shows the simulated and measured S-parameters before and after decoupling. It can be seen

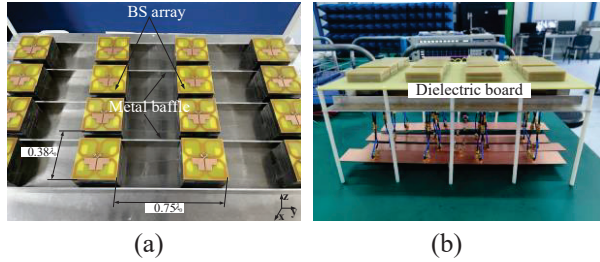


Fig. 3. (a) Photograph of fabricated array with metal baffle. (b) Fabricated array with baffle and dielectric board.

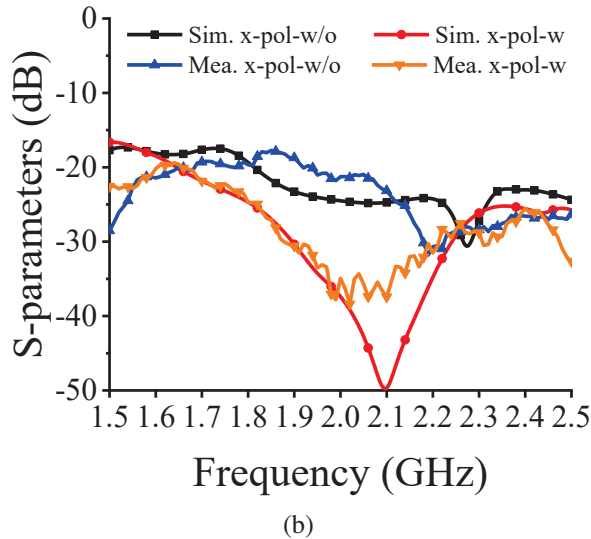
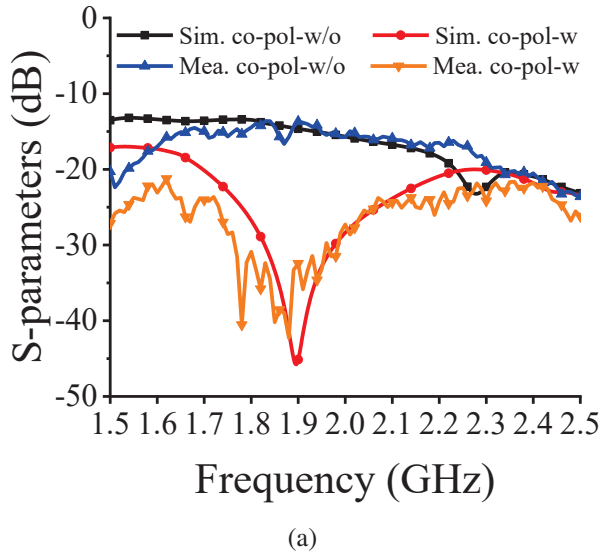


Fig. 4. Simulated and measured S-parameters before and after decoupling between antennas. (a) Co-polarized (co-pol) coupling. (b) Cross-polarized (x-pol) coupling.

that both the co-polarization and cross-polarization coupling between adjacent antennas (subarrays) has a sig-

nificant reduction across the whole frequency band. The mutual couplings between adjacent elements are reduced to below -20 dB within 1.7-2.2 GHz, and the couplings at the center frequency point are less than -30 dB with a reduction of 15 -dB.

III. MODEL DESCRIPTION OF POWER AMPLIFIER

Figure 5 shows the configuration of the PA module used in the experimental test. This PA module contains two identical PA channels, i.e., channel A and channel B. Each channel includes a coupled port at the PA output. The coupled port can be considered as a coupler, whose power is about 40 dB lower than that of the output. The signal characteristics of the PA's output can be inferred by observing the output signal from the coupled port.

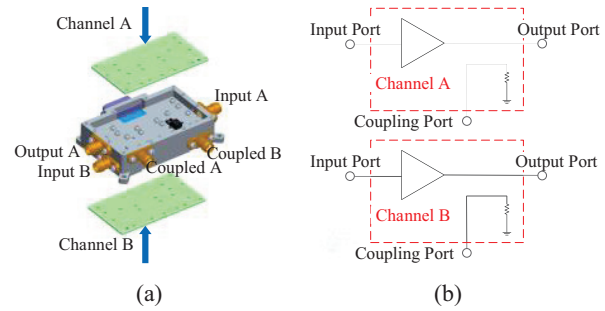


Fig. 5. Configuration of the PA module. (a) 3-D view. (b) Schematic view.

The output load-pull impedance of the PA and the corresponding waveform are shown in Figs. 6 (a) and (b), respectively. The parasitic parameters of the transistor are de-embedded during simulation and test, which means that the results are obtained from the intrinsic current source plane (I_{gen} plane). The PA is biased with a gate voltage (V_{GS}) of -3.2 V, corresponding to a Class-F condition. The drain voltage (V_{DS}) is 10 V. The fundamental impedance of $Z(f_0)$ is kept within nearly 50 Ohms from 2.03 GHz to 2.17 GHz, the corresponding second harmonic impedance $Z(2f_0)$ and the third harmonic impedance $Z(3f_0)$ are located at short and open, respectively, as shown in Fig. 6 (a). Under these impedances matching conditions, the drain voltage is approximately square wave, and the drain current is nearly half-wave rectified sinusoidal, which verifies the operation as Class-F mode [22], as shown in Fig. 6 (b). The measured results of the PA are shown in Figs. 6 (c) and (d). From 2.03 GHz to 2.17 GHz, the power added efficiency (PAE) is higher than 72%. The output power is larger than 30 dbm with a power gain larger than 11 -dB. Figure 6 (d) depicts the P_{out} , PAE and Gain performances within 10 -dB input-power range at the center

frequency of 2.1 GHz. The proposed PA is operating at the nearly P_{-3} point when $P_{in}=20$ dBm.

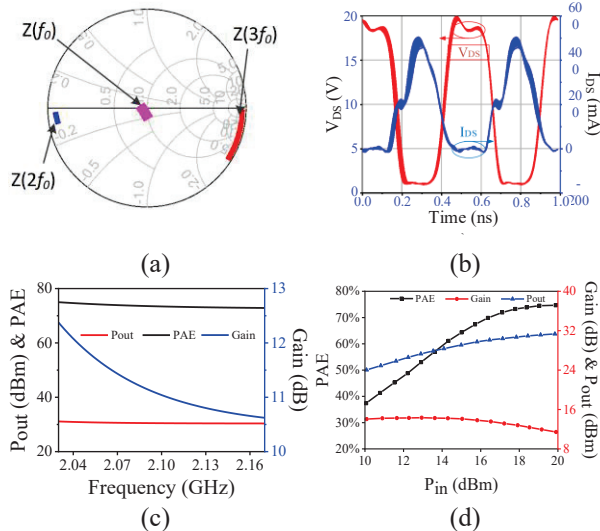


Fig. 6. (a) Output load-pull impedance. (b) Waveform in the I_{gen} plane. (c) Measurement results of the PA over frequency. (d) Measurement results of the PA over input power.

IV. MEASUREMENT SETUP AND RESULTS

A. Measurement setup

The BS array with and without the decoupling structure [19] is used to illustrate the decoupling effect on the linearity of the transmitter array. Two adjacent subarray ports of the same polarization are connected with two PAs (i.e., PA₁ and PA₂), while the rest of the subarray ports are terminated with 50-Ohm loads. Figure 7 shows the photo and schematic diagram of the measurement setup. Two continuous-wave (CW) signals with different frequencies from two signal generators are fed to the PAs. The PAs are fed by DC power supply where the DC voltage is 10 V. The coupled port of the PA is connected to a spectrum analyzer in order to observe the interference and nonlinearity of the PAs when loaded with the BS array with and without the decoupling.

The array without decoupling corresponds to the spectrum of high mutual coupling, and the array with decoupling corresponds to the spectrum of low mutual coupling.

Denote the two frequencies of the CW waves as f_1 and f_2 , respectively. Three signal cases with different frequencies and amplitudes are used to illustrate the decoupling effect on the PA output spectrum.

Case 1: The input signal frequencies are set to $f_1 = 2.05$ GHz (inject to PA₁) and $f_2 = 2.09$ GHz (inject to PA₂) with 20-dBm amplitude.

Case 2: The input signal frequencies are set to $f_1 = 2.13$ GHz (inject to PA₁) and $f_2 = 2.08$ GHz (inject to PA₂) with 15-dBm amplitude.

Case 3: The input signal frequencies are set to $f_1 = 2.10$ GHz (inject to PA₁) and $f_2 = 2.13$ GHz (inject to PA₂) with 10-dBm amplitude.

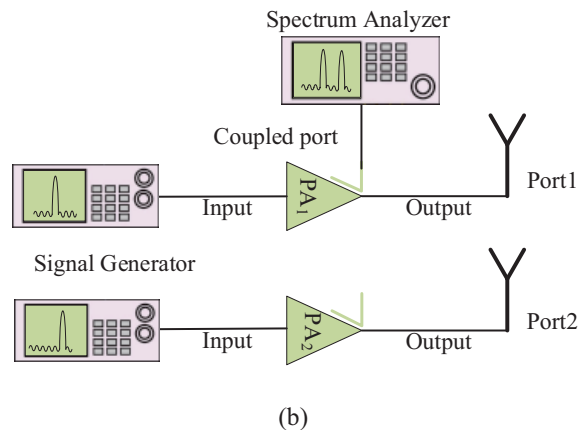
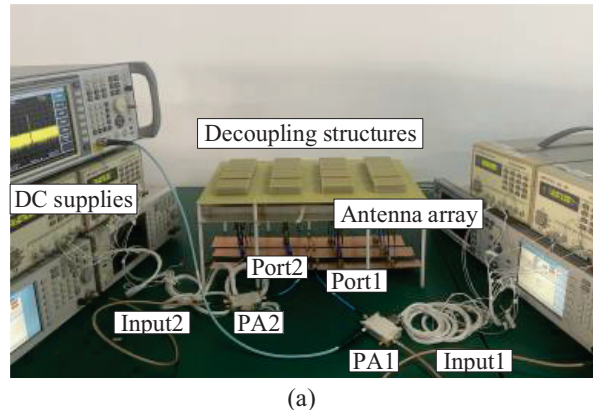


Fig. 7. (a) Photo and (b) schematic diagram of the measurement setup.

B. Measured Spectrum of PA

The PA₂ output spectra for case 1 with (wi. dec.) and without decoupling (w.o. dec.), are shown in Fig. 8 (a). If there were no mutual coupling or PA nonlinearity, the output spectrum from PA₂ should only contain the frequency of $f_2 = 2.09$ GHz. In the presence of mutual coupling and PA nonlinearity, however, the output spectrum from PA₂ contains multiple frequencies, as shown in Fig. 8 (a). The interference signal at $f_1 = 2.05$ GHz with an amplitude of -21.8 dbm is mainly due to the array mutual coupling. In addition, two spurious signals at 2.13 GHz and 2.17 GHz are observed due to the PA nonlinearity in the presence of mutual coupling. After the decoupling structure [cf. Fig. 3] is applied to the BS array, the mutual coupling is reduced by 15 db (i.e., from

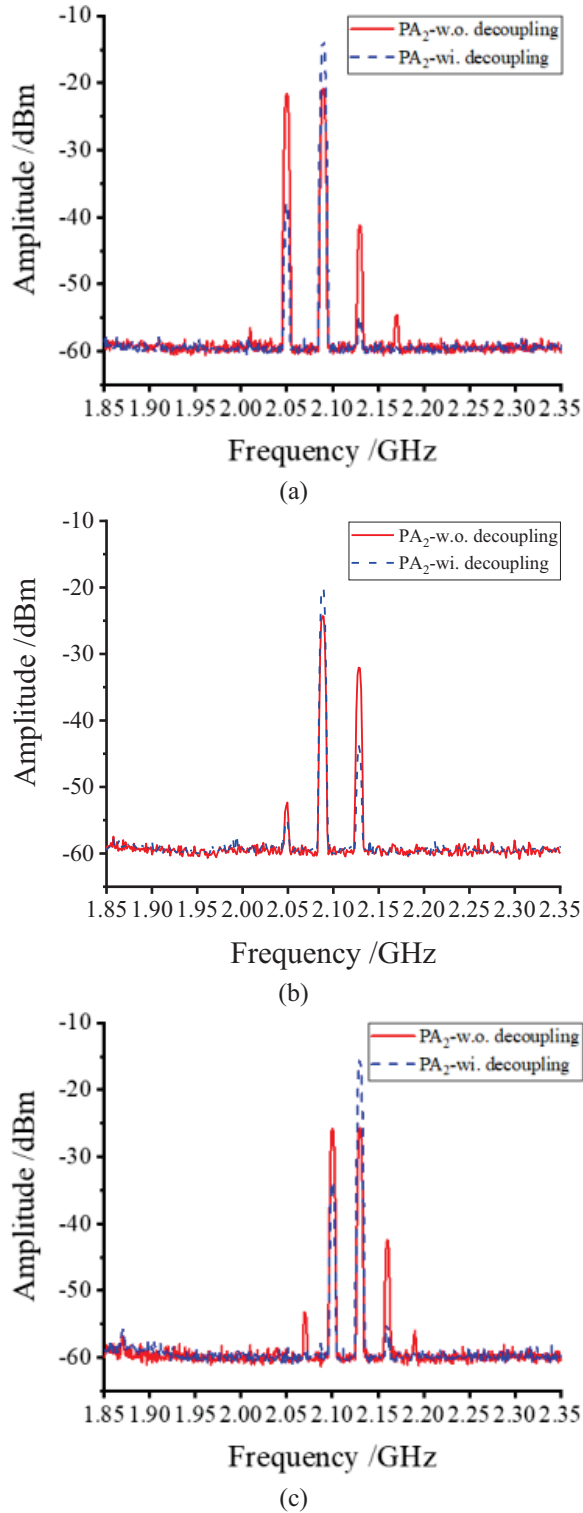


Fig. 8. Measured spectrum at the coupled port of PA₂ for (a) case 1, (b) case 2 and (c) case 3.

–15 to –30 db). As a result, the interference signal at $f_1 = 2.05$ GHz is suppressed by 16.1 db (i.e., from –21.8

to –37.9 dbm), the two spurious signals at 2.13 GHz and 2.17 GHz are almost eliminated, and the useful signal at $f_2 = 2.09$ GHz (i.e., the input frequency) is increased from –21.0 to –14.2 dbm.

The PA₂ output spectrum for case 2 with and without decoupling are depicted in Fig. 8 (b). The results are consistent with that of case 1. The interference signal occurring at $f_1 = 2.13$ GHz is mainly due to the mutual coupling, while the spurious signal at 2.05 GHz is attributed to the combination of PA nonlinearity and mutual coupling. With effective decoupling, the interference signal at $f_1 = 2.13$ GHz is reduced from –32.1 dbm to –43.7 dbm, while the amplitude of the useful signal at $f_2 = 2.08$ GHz is improved from –24.2 to –20.1 dbm.

Figure 8 (c) depicts the PA₂ output spectrum of case 3 with and without decoupling, and the results of case 3 are consistent with that of case 1 and case 2. When the mutual coupling in array is significantly reduced, the interference and spurious caused by nonlinearity are suppressed, such as the interference signal at 2.10 GHz is reduced from –26.1 dbm to –33.8 dbm, the spurious signal at 2.16 GHz is almost completely eliminated, while the amplitude of the desired signal at $f_2 = 2.13$ GHz increases from –25.9 dbm to –15.6 dbm.

Table 1 summarizes the comparison of PA₂ output spectrum in the array with and without decoupling in three cases, all of which increase the desired signal amplitude and suppress interference and spurious signals.

Table 1: Comparison of PA₂ output after decoupling

	Case 1	Case 2	Case 3
Improvement of desired signal/dB	6.8	4.1	10.3
Suppression of interference /dB	16.1	11.6	7.7

Table 2: Suppression of PA₁ output at different amplitudes

	Case 1	Case 2	Case 3
Magnitude of CW signal /dBm	20	15	10
Suppression of interference /dB	7.7	9.6	7.6

The results in Table 1 are for PA₂. The output results of PA₁ are similar, as shown in Fig. 9. After the mutual coupling in the array is reduced, the output spectrum result of PA₁ is that the desired signal is enhanced and

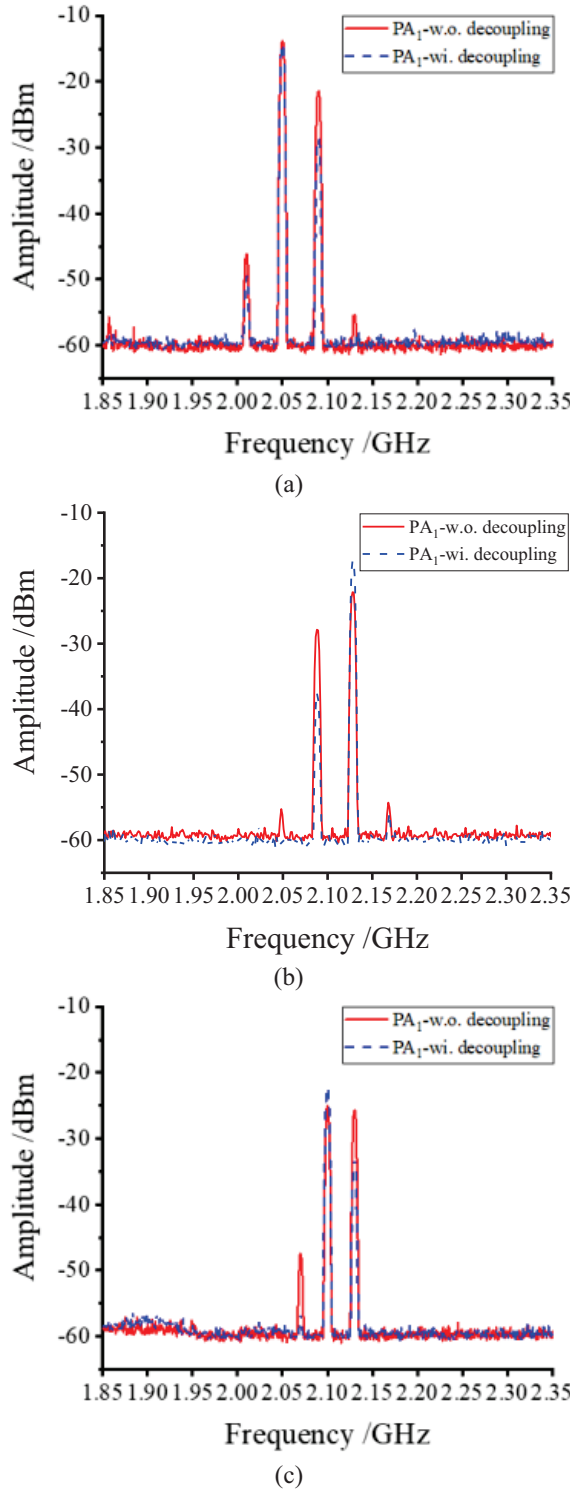


Fig. 9. Measured spectrum at the coupled port of PA₁ for (a) case 1, (b) case 2 and (c) case 3.

the interfering signal is suppressed. Table 2 shows the the suppression level of interference signal for different

amplitudes. When the amplitude of the input signal varies from 20 db to 10 db, the coupling reduction can bring obvious interference suppression effect.

V. CONCLUSION

A measurement-based characterization of the decoupling effect on the PA linearity in a transmitter array has been conducted in this paper. The experimental results show that the mutual coupling not only deteriorates the linearity, but also produces strong interference. For three cases with different frequencies and amplitudes, the desired signal could be improved by 4-10 db, and the spurious and interference signals could be suppressed by 7-16 db. It was demonstrated experimentally that decoupling could improve the PA linearity, reduce the interference, and enhance the desired signal in the transmitter array. *Sci. China Inf. Sci.*

ACKNOWLEDGEMENTS

This work was supported by the National Key R&D Program of China under Grant 2022YFB3902400.

REFERENCES

- [1] H. Pei, X. Chen, X. Huang, X. Liu, X. Zhang, and Y. Huang, "Key issues and algorithms of multiple-input-multiple-output over-the-air testing in the multi-probe anechoic chamber setup," *Sci. China Inf. Sci.*, vol. 65, no. 3, pp. 47-73, Mar. 2022.
- [2] R. He, B. Ai, G. Wang, M. Yang, C. Huang, and Z. Zhong, "Wireless channel sparsity: Measurement, analysis, and exploitation in estimation," *IEEE Wireless Commun.*, vol. 28, no. 4, pp. 113-119, Aug. 2021.
- [3] B. Gashi, S. Krause, R. Quay, C. Fager, and O. Ambacher, "Investigations of active antenna doherty power amplifier modules under beam-steering mismatch," *IEEE Microwave Compon. Lett.*, vol. 28, no. 10, pp. 930-932, Oct. 2018.
- [4] K. Hausmair, S. Gustafsson, C. Sánchez-Pérez, P. N. Landin, U. Gustavsson, T. Eriksson, and C. Fager, "Prediction of nonlinear distortion in wideband active antenna arrays," *IEEE Trans. Microwave Theory Tec.*, vol. 65, no. 11, pp. 4550-4563, Nov. 2017.
- [5] F. M. Barradas, T. R. Cunha, P. M. Cabral, and J. C. Pedro, "Modeling PA linearity and efficiency in MIMO transmitters," *IEEE MTT S. Int. Microwave Sym. Dig.*, Honolulu, HI, USA, pp. 1999-2002, Oct. 2017.
- [6] F. M. Barradas, P. M. Tomé, J. M. Gomes, T. R. Cunha, P. M. Cabral, and J. C. Pedro, "Power, linearity, and efficiency prediction for MIMO arrays with antenna coupling," *IEEE Trans. Microwave Theory Tech.*, vol. 65, no. 12, pp. 5284-5297, Nov. 2017.

- [7] J. C. Pedro and S. A. Maas, "A comparative overview of microwave and wireless power-amplifier behavioral modeling approaches," *IEEE Trans. Microwave Theory Tech.*, vol. 53, no. 41, pp. 1150-1163, Apr. 2005.
- [8] D. H. Wisell, B. Rudlund, and D. Ronnow, "Characterization of memory effects in power amplifiers using digital two-tone measurements," *IEEE Trans. Instrum. Mea.*, vol. 56, no. 6, pp. 2757-2766, Dec. 2007.
- [9] S. Amin, W. Van Moer, P. Händel, and D. Rönnow, "Characterization of concurrent dual-band power amplifiers using a dual two-tone excitation signal," *IEEE Trans. Instrum. Mea.*, vol. 64, no. 10, pp. 2781-2791, Oct. 2015.
- [10] C. Fager, K. Hausmair, K. Buisman, K. Andersson, E. Sienkiewicz, and D. Gustafsson, "Analysis of nonlinear distortion in phased array transmitters," *Proc. Int. Workshop Integr. Nonlinear Microw. Millimetre-Wave Circuits, INMMiC*, Graz, Austria, pp. 1-4, May 2017.
- [11] C. Fager, T. Eriksson, F. Barradas, K. Hausmair, T. Cunha, and J. C. Pedro, "Linearity and efficiency in 5G transmitters: new techniques for analyzing efficiency, linearity, and linearization in a 5G active antenna transmitter context," *IEEE Microwave Mag.*, vol. 20, no. 5, pp. 35-49, May 2019.
- [12] J. Jiang, Y. Li, L. Zhao, L. Zhao, and X. Liu, "Wideband MIMO directional antenna array with a simple meta-material decoupling structure for X-Band applications," *Applied Computational Electromagnetics Society (ACES) Journal*, vol. 35, no. 5, pp. 556-566, May 2020.
- [13] J. Jiang, Y. Xia, and Y. Li, "High isolated X-Band MIMO array using novel wheel-like metamaterial decoupling structure," *Applied Computational Electromagnetics Society (ACES) Journal*, vol. 34, no. 12, pp. 1829-1836, 2019.
- [14] X. Chen, M. Zhao, H. Huang, Y. Wang, S. Zhu, C. Zhang, J. Yi, and A. A. Kishk, "Simultaneous decoupling and decorrelation scheme of MIMO arrays," *IEEE Tran. Veh. Technol.*, vol. 71, no. 2, pp. 2164-2169, Feb. 2022.
- [15] F. Faraz, X. Chen, Q. Li, J. Tang, J. Li, T. A. Khan, and X. Zhang, "Mutual coupling reduction of dual polarized low profile MIMO antenna using decoupling resonators," *Applied Computational Electromagnetics Society (ACES) Journal*, vol. 35, no. 1, pp. 38-43, 2020.
- [16] B. Qian, X. Chen, and A. A. Kishk, "Decoupling of microstrip antennas with defected ground structure using the common/differential mode theory," *IEEE Antennas Wirel. Propag. Lett.*, vol. 20, no. 5, pp. 828-832, May 2021.
- [17] Y. Da, Z. Zhang, X. Chen, and A. A. Kishk, "Mutual coupling reduction with dielectric superstrate for base station arrays," *IEEE Antennas Wirel. Propag. Lett.*, vol. 20, no. 5, pp. 843-847, May 2021.
- [18] F. Liu, J. Guo, L. Zhao, G. Huang, Y. Li and, Y. Yin, "Ceramic superstrate-based decoupling method for two closely packed antennas with cross-polarization suppression," *IEEE Trans. Antennas Propag.*, vol. 69, no. 3, pp. 1751-1756, 2021.
- [19] B. Liu, Y. Da, X. Chen, and A. A. Kishk, "Hybrid decoupling structure based on neutralization and partition schemes for compact large-scale base station arrays," *IEEE Antennas Wirel. Propag. Lett.*, vol. 21, no. 2, pp. 267-271, 2022.
- [20] CST Microwave Studio, CST Gmbh, 2020. <http://www.cst.com>
- [21] B. Liu, X. Chen, J. Tang, A. Zhang, and A. A. Kishk, "Co- and cross-polarization decoupling structure with polarization rotation property between linearly polarized dipole antennas with application to decoupling of circularly polarized antennas," *IEEE Trans. Antennas Propag.*, vol. 70, no. 1, pp. 702-707, Jan. 2022.
- [22] D. Kang, D. Yu, K. Min, J. Choi, D. Kim, B. Jin, M. Jun, and B. Kim, "A highly efficient and linear class-AB/F power amplifier for multimode operation," *IEEE Trans. Microwave Theory Tech.*, vol. 56, no. 1, pp. 77-87, Jan. 2008.



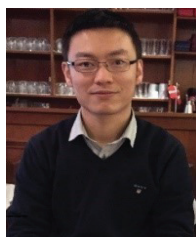
Fangyun Peng received her B.Sc. degree in Electrical Information Engineering from Southwest Jiaotong University, Chengdu, China, in 2018. She is currently pursuing a Ph.D. degree at the School of Electronic and Information Engineering from Xi'an Jiaotong University. Her research interests include over-the-air testing.



Fei Yang is with the China Academy of Space Technology.



Bo Liu received his B.Sc. degree in Electronic Information Engineering from Xidian University, Xi'an, China, in 2019. He received his M.Sc. degree from the School of Electronic and Information Engineering, Xi'an Jiaotong University, Xi'an, China, in 2022. His research interests include MIMO antennas and the decoupling of MIMO antennas.



Xiaoming Chen received his B.Sc. degree in Electrical Engineering from Northwestern Polytechnical University, Xi'an, China, in 2006, and M.Sc. and Ph.D. degrees in Electrical Engineering from Chalmers University of Technology, Gothenburg, Sweden, in 2007 and 2012, respectively. From 2013 to 2014, he was a post-doctoral researcher at that same university. From 2014 to 2017, he was with Qamcom Research & Technology AB, Gothenburg, Sweden. Since 2017, he has been a professor at Xi'an Jiaotong University, Xi'an, China. His research areas include MIMO antennas, over-the-air testing, reverberation chambers and has published more than 150 journal articles on these topics.

Prof. Chen currently serves as a Senior Associate Editor for IEEE Antennas and Wireless Propagation Letters. He was the general chair of the IEEE International Conference on Electronic Information and Communication Technology (ICEICT) in 2021. He won the first prize of the universities' scientific research results in Shaanxi province, China, 2022. He received the IEEE outstanding Associate Editor awards in 2018, 2019, 2020, 2021, and the URSI (International Union of Radio Science) Young Scientist Award 2017 and 2018.

A Hybrid EMC Testing Facility: Combining Transmission Line and Reverberation Chamber Measurement System

Kai Chen^{1,2}, Wenjun Qi¹, Peng Peng³, Hailong Wang¹, Xueqi Shen²,
Yongjiu Zhao¹, and Qian Xu^{1,*}

¹College of Electronic and Information Engineering
Nanjing University of Aeronautics and Astronautics, Nanjing, 211106, China
chenkay@nuaa.edu.cn, qiwenjun@nuaa.edu.cn, emhai@foxmail.com, yjzhao@nuaa.edu.cn,
*emxu@foxmail.com

²Nanjing Rongce Testing Technology Ltd
Nanjing, 211112, China
george@emcdir.com

³EMC technical expert with Ford Motor Research & Engineering Center (Nanjing)
Nanjing, 211100, China
pp02003125@126.com

Abstract – By combining a transmission line system (TLS) and a reverberation chamber (RC), a hybrid electromagnetic compatibility (EMC) testing facility is designed and constructed. Generally, the lowest usable frequency (LUF) of an RC is limited by its dimension, which limits the application of RCs for EMC testing at low frequencies. Therefore, to improve the field uniformity (FU) of an RC at frequencies lower than the LUF, a TLS is integrated into the RC. After optimizing the load resistance, length, and width of the TLS, the resonant frequency and electric field spikes of the hybrid system are eliminated. The FU of the E-field in the system is greatly improved in the frequency range of 0-30 MHz. Moreover, using an oscillating wall stirrer in the RC, the FU satisfies the standard (IEC 61000-4-21) above 80 MHz. Results show that combining the TLS and the RC testing system could be widely used for EMC testing in the frequency range of 0-30 MHz and 80 MHz-6 GHz.

Index Terms – electromagnetic compatibility, field uniformity, reverberation chamber, transmission line system.

I. INTRODUCTION

Nowadays, nearly all electronic products should comply with electromagnetic compatibility (EMC) standards [1–2]. Ideally, products should be tested in a uniform and well-described facility in the frequency range of interest. If the field is not uniform enough in the testing area, the E-field fluctuation could be large and the

accuracy of testing results may not be guaranteed. Thus, a variety of well-developed techniques have been introduced into the EMC testing industry, such as anechoic chambers, reverberation chambers (RC) [3], and transmission line systems [4–6].

An RC is an electrically large shielded cavity, which tunes the boundary conditions to create a statistically uniform, isotropic, and randomly polarized field [7-10]. Utilizing different kinds of stirring methods, such as source stirring [11], mechanical stirring [12–13], and frequency stirring [14], RCs have been widely applied to EMC testing. The lowest usable frequency (LUF) of an RC is affected by its first resonance frequency limited by the dimension of an RC [8]. For an RC with dimensions of 12.7 m × 10.8 m × 6.3 m, the LUF is about 80 MHz. How to extend the usable frequency range at the lower bound has attracted researchers' attention in recent years [15–18].

Another important method for EMC testing is the transmission line technique [19–21]. It can only generate a transverse electromagnetic (TEM) mode in the testing frequency range. When the frequency increases, higher modes exist and the FU is deteriorated. Since an RC has a LUF while a TLS has a highest usable frequency (HUF), by combining these two facilities, the working frequency range could be expanded in one facility.

In this paper, we integrate a TLS and an RC to realize a hybrid EMC testing system in the frequency range of 0 - 30 MHz and 80 MHz - 6 GHz. The designed TLS generates testing fields below 30 MHz, and the RC using a sliding wall generates testing fields at frequen-

cies above 80 MHz. The paper is organized as follows: section II presents the design and verification of the proposed TLS. Measurement results of the FU in the RC are shown in section III. Finally, section IV concludes the paper.

II. DESIGN AND VERIFICATION OF THE TLS

A stripline is realized by placing a transmission line above and parallel to the ground plane. When one end of the stripline is excited, the other end is connected with broadband resistances, it transmits TEM waves at working frequencies. The E-field generated by a stripline is uniform at low frequencies. The designed stripline and the geometry of the structure are demonstrated in Figs. 1 (a) and (b). By optimizing the load resistance and the cutoff frequency comprehensively, the structure dimensions are obtained as follows: $L_1 = 3\text{ m}$, $L_2 = 5.5\text{ m}$, $L_3 = 2.6\text{ m}$ and $W_1 = 3\text{ m}$. Furthermore, the characteristics of the stripline in the open area test site (OATS) are verified and good performance is obtained. In the operating frequency band, the voltage standing wave ratio (VSWR) is less than 4, and the cutoff frequency is up to 30 MHz, which satisfies the designed requirements. Then the simulation model of the RC and the oscillating wall is built as shown in Fig. 2 (a), the oscillating wall is composed of four irregular horizontal plates, used as the mechanical stirrer inside the RC.

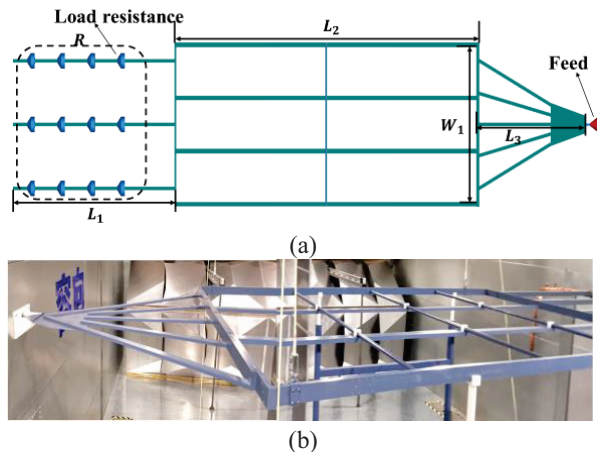


Fig. 1. The designed strip line. (a) Geometry structure. (b) Fabricated sample.

According to the displacement of the oscillating wall, the scenarios are marked as 0%, 50% and 100%, respectively. 0% means that the movement of the stirrer is the smallest. We measure the FU at a 1 m height plane [1] using

$$FU = 20 \log_{10} \left(\frac{E_{max}}{E_{min}} \right), \quad (1)$$

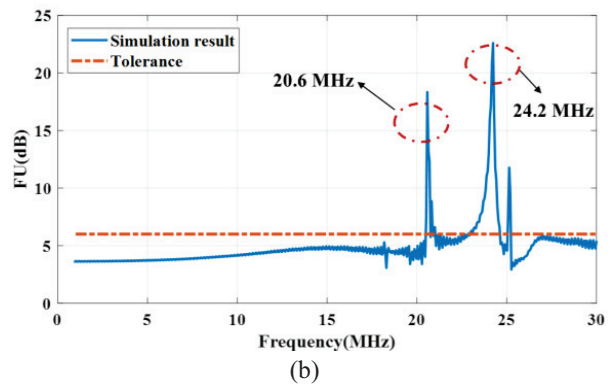
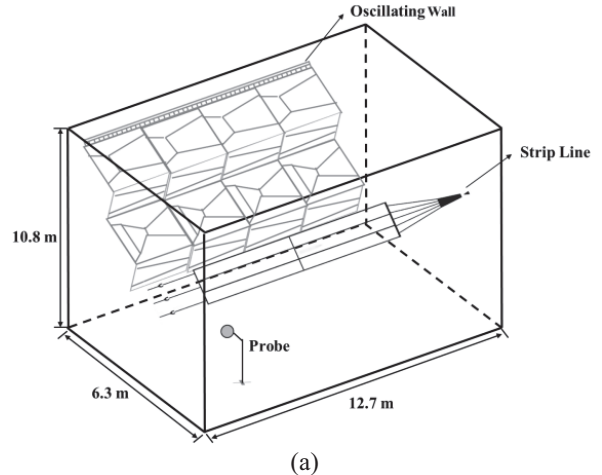


Fig. 2. (a) The initial hybrid system. (b) The simulation results of FU in an RC.

where E_{max} is the maximum value of E-field and E_{min} is the minimum value of E-field in the testing area. The simulation result is demonstrated in Fig. 2 (b), some FU spikes over the frequency range of 20-30 MHz exist.

Generally, we can perturb the system to shift the resonance frequency of an RC and obtain a uniform field in the usable frequency band. Two methods are given: (a) change the position of the oscillating wall. The resonance frequency varies with the inner structures of the RC; (b) reduce the Q-factor of the E-field at resonance frequency until it can be ignored. During the simulation process, the latter method is selected and the oscillating wall is fixed at 100% state.

For the optimization of the designed stripline, the load impedance is first discussed. Considering that high field strength is applied during the EMC testing process, distributed resistances are adopted, to avoid exceeding the power tolerance of the resistances. We use a distributed loading network which is formed by many resistances in series and in parallel. Ceramic resistors are selected to ensure temperature and frequency stability. In Figs. 3 (a) and (b), the simulation results of E-field for

1 W input power and the FU using different values of the load resistances are analyzed. With the increase of the single load resistance, the FU first tends to be flat and then deteriorates along with the frequency varies. When the value is about 110Ω , the E-field and FU are the best.

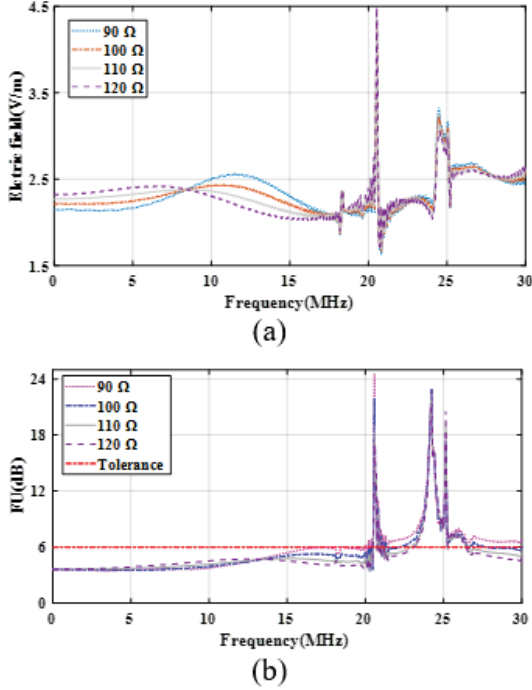


Fig. 3. From 0 to 30 MHz, the simulation results changing with the value of load in an RC, (a) E-field for 1 W input power and (b) FU.

Then, the E-field distribution of the hybrid system at frequencies where the field resonances appear is analyzed. In Figs. 4 (a) and (b), the resonant frequency of is about 20.6 MHz, resulting in a nonuniform E-field under the stripline. In addition, from Figs. 4 (c) and (d), at 24.2 MHz, the sharp edges enhance the E-field below the strip line, which affect the field uniformity significantly. Thus the resonances need to be shifted or reduced at some frequencies. To achieve this effect, we place three horizontal metal rods in front of the oscillating wall. By increasing the coupling between the metal rods and the oscillating wall (where the E-field are in the same direction), the resonance can be reduced or shifted. It can be observed from the simulation results in Fig. 5 (a) that the FU around 20 MHz is reduced to below 6 dB. However, the FU deteriorates from 25 MHz to 30 MHz, which needs to be further optimized.

To further reduce the resonance effect, some extra structures are added to the hybrid system in Fig. 6 (a). After analyzing the E-field again, we put 500Ω loads at both ends of the metal rods and added two vertical metal wires into the system. The two metal wires terminated

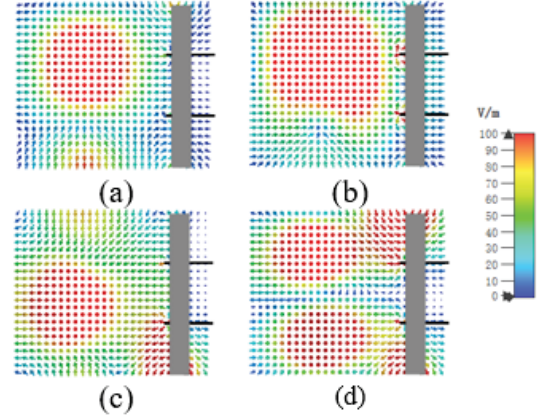


Fig. 4. The E-field distribution on the 1 m plane at 20.6 MHz (a) $t=0$; (b) $t=T/4$; at 24.2 MHz; (c) $t=0$; (d) $t=T/4$.

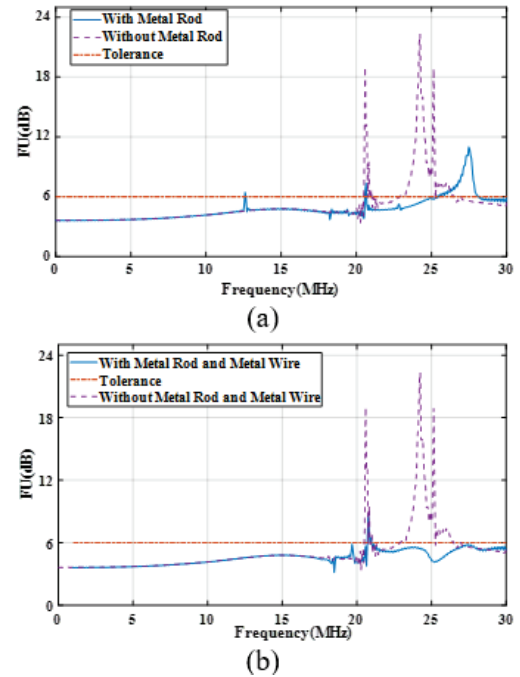


Fig. 5. The optimizing simulation results of FU in an RC compared with the tolerance requirements combining (a) metal rod, and (b) metal rod and metal wire.

with 500Ω resistors on both sides are placed in front of the oscillating wall. The resonance is reduced and the FU is improved. The simulation results from Fig. 5 (b) show that the FU spikes from 25 MHz to 30 MHz is reduced to below 6 dB. The spike of E-field at about 20 MHz could be ignored here, which would be eliminated by tuning the position of the oscillating wall in the testing process. Finally, the simulation results satisfied the testing requirements.

III. MEASUREMENTS OF THE HYBRID SYSTEM

We test the FU of the hybrid system in two scenarios: one utilizing the proposed TLS in an RC from 0 - 30 MHz, the other using the oscillating wall as a mechanical stirrer from 80 MHz to 6 GHz. The measurement results demonstrate that the usable frequency range of the hybrid system can be extended.

A. Measurement of FU from 0-30 MHz

As shown in Fig. 6 (b), the hybrid system is composed of an RC, a stripline, a field probe, an oscillating wall, a signal generator, and a power amplifier. In an ideal simulation process (the metal and the boundary are perfect electrical conductors), the input power is 2500 W and 100 V/m field strength is generated. During the actual measurement, due to the loss of RF cables and the cavity, a higher input power is used to meet the requirements.

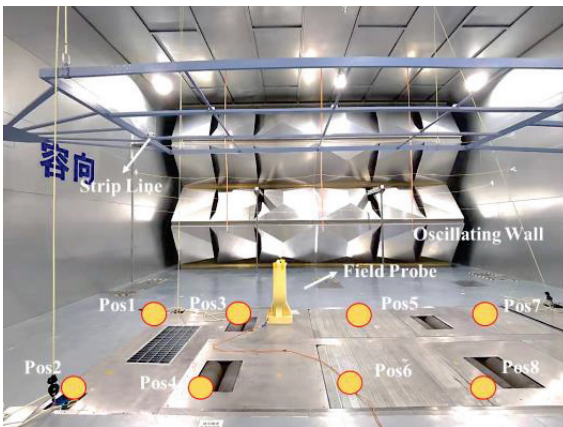
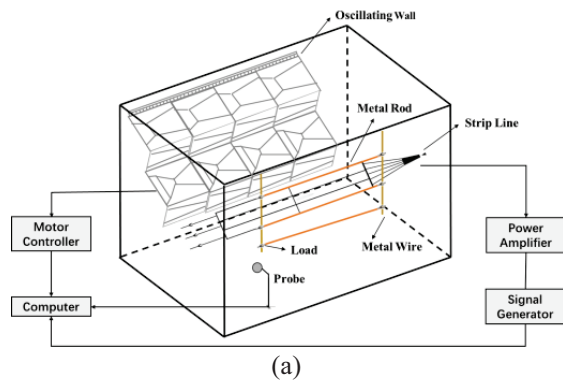
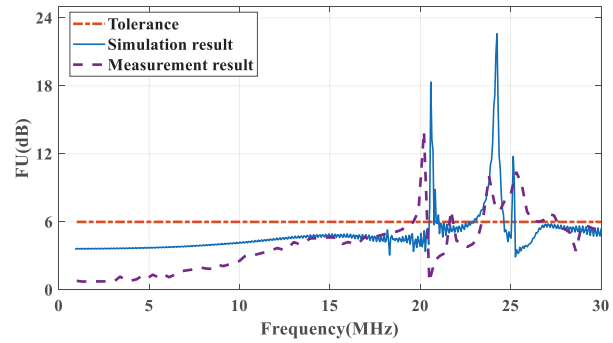
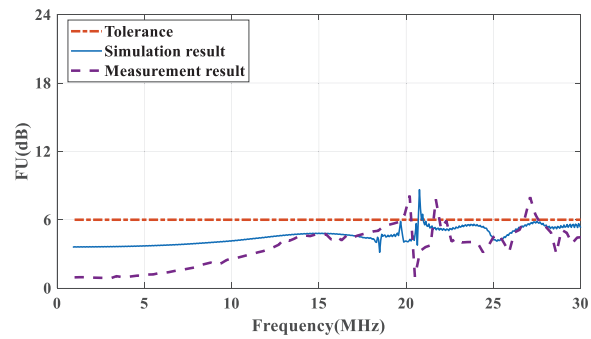


Fig. 6. Typical FU measurement setup with the TLS: (a) schematic plot, and (b) measurement scenario in an RC.

In this measurement, the designed TLS is placed beside the metal wall in the RC. Moreover, the E-field probes are placed at 8 different positions at the corner



(a)



(b)

Fig. 7. From 0 MHz to 30 MHz, the simulation and measurement results of FU in the RC combining the TLS compared with the tolerance requirements, (a) initial results, and (b) optimized results.

of the working volume under the TLS. We measure the FU of the hybrid system as shown in Fig. 7 (a), the initial measurement results have slightly deviated from the simulation results. In the frequency range of 1 MHz - 18 MHz, the simulated FU is higher than the measured FU, due to the field probe positions of simulation being sampled at a higher density than used in the measurements. From 18 MHz to 30 MHz, some spikes of FU appeared. The maximum FU of the stripline is 14.0 dB, which does not satisfy the expected results.

The final measurement scenario in an RC with the TLS is shown in Fig. 6. Additional metal rods are added in the hybrid system. The optimized simulation and measurement results are shown in Fig. 7 (b). Compared with the initial results in Fig. 4, the FU is almost less than 6 dB over the whole frequency band. Considering the frequency dependency of the resistors, the measurement result is not as ideal as the simulation result. The reasons could be due to the difference between the simulation model and the reality. In the simulation, the structure of the stirrer inside the RC and is simplified as we do not have the detailed drawings from the manufacturer. The position of the stirrer in the simulation and reality may

not be exactly the same. Since the RC is a high Q cavity, the difference in the models could lead to very different results. As we do not expect the same results between simulation and measurement, as long as our approach works well in both simulation and measurement, it could be enough in practice and the measurement data is finally used in EMC testings.

It is noted that only a few samples of FU exceeded 6 dB in the frequency range of 18 MHz - 23 MHz and 26 MHz - 28 MHz. To avoid the resonance and achieve a lower FU, we need to tune the position of the oscillating wall (0%, 50%, and 100%) inside the RC to perform mechanical stirring in the frequency range of 20 MHz-30 MHz.

By shifting the resonant frequencies, the final results shown in Fig. 8 can achieve a lower FU, which satisfied the testing requirements in the entire working area. We show that different positions of the oscillating wall could avoid the spikes of FU and the hybrid system is proved to be feasible.

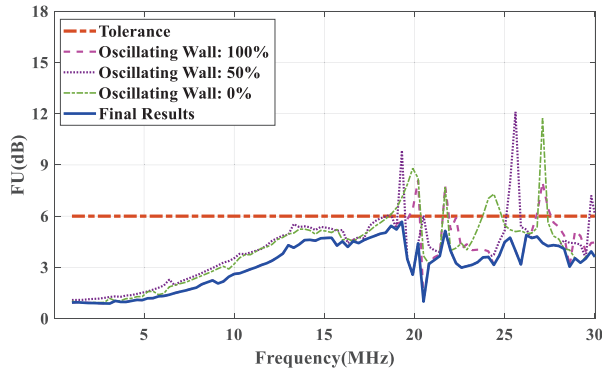


Fig. 8. The FU in the RC with different state of the oscillating wall compared with the tolerance requirements from 0 - 30 MHz.

B. Measurement of FU from 80 MHz-6 GHz

In an RC, the FU characterizes the statistical uniformity of the E-fields. The statistical FU is defined as the relative standard deviation of the maximum E-fields obtained at the eight positions in the testing volume [2]. The standard deviation σ (dB) (i.e. the FU) is defined as

$$FU(\text{dB}) = 10\log_{10} \frac{\sigma(\text{linear}) + \text{mean}}{\text{mean}}. \quad (2)$$

When the FU is lower than the tolerance given in [2], the field in an RC can be regarded as statistically uniform. Generally, the LUF occurs at three to six times the first chamber resonance f_{1st} . The f_{1st} of the RC is 18.23 MHz and the theoretical LUF is about 54.7 MHz-109.39 MHz. Furthermore, the LUF is about 80 MHz, corresponding with the theoretical value.

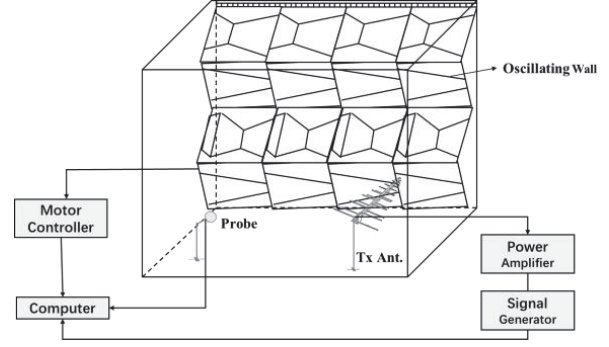


Fig. 9. Typical FU measurement setup using an oscillating wall.

A typical measurement setup is given in Fig. 9 from 80 MHz to 6 GHz. The measurement system consists of the RC, a Tx antenna, the oscillating wall, and the E-field probes. In the testing, the oscillating wall [12] moves back and forth to perturb inner structures of the RC during one measurement period. With the movement of the oscillating wall in the range of 3 m, the field of the RC achieves statistical uniformity. A power amplifier is used to compensate for the cable loss and the cavity loss.

In Fig. 10, the FUs obtained from field probes are lower than the FU tolerance from 80 MHz to 6 GHz. Furthermore, the FUs for different polarizations (E_x , E_y , and E_z) and the total FU are all less than 4 dB from 80 MHz to 100 MHz and less than 3 dB from 100 MHz to 6 GHz, which satisfies the limit in the IEC 61000-4-21 standard.

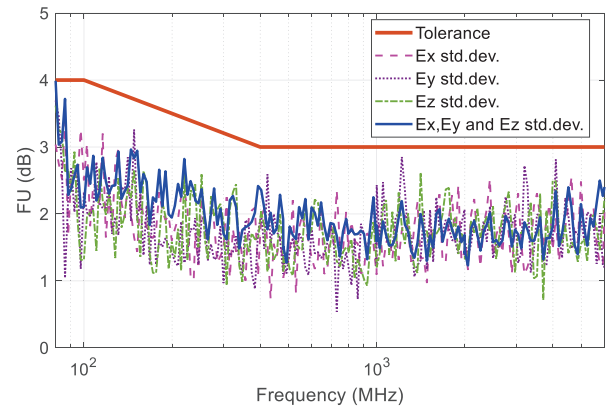


Fig. 10. The FU in the RC using oscillating wall compared with the tolerance requirements from 80 MHz - 6 GHz.

IV. CONCLUSION

For EMC testing, by combining the TLS and the RC, the usable frequency band of the hybrid system has been extended. The stripline is designed in the frequency of

0-30 MHz which can generate a uniform E-field. Moreover, through optimizations, the stripline is integrated into the RC. Additional structures are added to tune the resonant frequencies and improve the uniformity of the E-field. The results show that the FU is below 6 dB within 0-30 MHz, and the resonances in the frequency range of 20-30 MHz can be avoided by tuning the structures inside the RC.

ACKNOWLEDGMENT

This work was supported in part by Nanjing Rongce Testing Technology Ltd, the National Defense Basic Scientific Research Program of China under Grant JCKYS2021DC05, and The Fund of Prospective Layout of Scientific Research for NUAA.

REFERENCES

- [1] IEC 61000-4-21, *Electromagnetic Compatibility (EMC) – Part 4-21: Testing and Measurement Techniques – Reverberation Chamber Test Methods*, IEC Standard, Ed 2.0, 2011-01.
- [2] ISO 11452-2, *Road Vehicles — Component Test Methods for Electrical Disturbances From Narrowband Radiated Electromagnetic Energy — Part 2: Absorber-lined Shielded Enclosure*, ISO Standard, Ed 2.0, 2004-11.
- [3] M. Migliaccio, G. Gradoni, and L. R. Arnaut, “Electromagnetic reverberation: The legacy of Paolo Corona,” *IEEE Trans. Electromagn. Compat.*, vol. 58, no. 3, pp. 643-652, Jun. 2016.
- [4] M. L. Crawford, “Generation of standard EM fields using TEM transmission cells,” *IEEE Trans. Electromagn. Compat.*, vol. EMC-16, no. 4, pp. 189-195, Nov. 1974.
- [5] M. Valek, T. Korinek, and T. Bostik, “Design of stripline for EMC testing,” *Proc. 14th IEEE Conf. Microw. Tech.*, Prague, Czech Republic, pp. 1-4, 2008.
- [6] B. E. Roseberry and R. B. Schulz, “A parallel-stripline for testing of RF susceptibility,” *IEEE Trans. Electromagn. Compat.*, vol. 7, no. 2, pp. 142-150, Jun. 1965.
- [7] D. A. Hill, *Electromagnetic Fields in Cavities: Deterministic and Statistical Theories*, Wiley-IEEE Press, New Jersey, USA, 2009.
- [8] Q. Xu and Y. Huang, *Anechoic and Reverberation Chambers: Theory, Design and Measurements*, Wiley-IEEE, Chichester, UK, 2019.
- [9] X. Chen, J. Tang, T. Li, S. Zhu, Y. Ren, Z. Zhang, and A. Zhang, “Reverberation chambers for over-the-air tests: An overview of two decades of research,” *IEEE Access*, vol. 6, pp. 49129-49143, Aug. 2018.
- [10] A. Adardour, G. Andrieu, and A. Reineix, “On the low-frequency optimization of reverberation chambers,” *IEEE Trans. Electromagn. Compat.*, vol. 56, no. 2, pp. 266-275, Apr. 2014.
- [11] Q. Xu, L. Xing, Y. Zhao, T. Jia, and Y. Huang, “A source stirred reverberation chamber using a robotic arm,” *IEEE Trans. Electromagn. Compat.*, vol. 62, no. 2, pp. 631-634, Apr. 2020.
- [12] Z. Zhou, P. Hu, X. Zhou, J. Ji, M. Sheng, P. Li, and Q. Zhou, “Performance evaluation of oscillating wall stirrer in reverberation chamber using correlation matrix method and modes within Q -bandwidth,” *IEEE Trans. Electromagn. Compat.*, vol. 62, no. 6, pp. 2669-2678, Dec. 2020.
- [13] K. Madsen, P. Hallbjorner, and C. Orlenius, “Models for the number of independent samples in reverberation chamber measurements with mechanical, frequency, and combined stirring,” *IEEE Antennas Wireless Propag. Lett.*, vol. 3, pp. 48-51, 2004.
- [14] T. A. Loughry, “Frequency stirring: An alternate approach to mechanical mode-stirring for the conduct of electromagnetic susceptibility testing,” Phillips Laboratory, Kirtland Air Force Base, NM Technical Report 91-1036, 1991.
- [15] A. Coates and A. P. Duffy, “Maximum working volume and minimum working frequency tradeoff in a reverberation chamber,” *IEEE Trans. Electromagn. Compat.*, vol. 49, no. 3, pp. 719-722, Aug. 2007.
- [16] H. Sun, Z. Li, C. Gu, Q. Xu, X. Chen, Y. Sun, and F. Martin, “Metasurfaced reverberation chamber,” *Sci. Rep.* vol. 8, no. 1577, Jan. 2018.
- [17] J. Perini and L. S. Cohen, “Extending the operation of mode stirred chambers to low frequencies,” *IEEE International Symp. on Electromagn. Compat.*, Minneapolis, MN, USA, pp. 964-965, 2002.
- [18] M. L. Crawford, M. T. Mark, J. M. Ladbury, and B. F. Riddle, *Measurement and Evaluation of a TEM/Reverberating Chamber*, National Institute of Standards and Technology, Gaithersburg, 1990.
- [19] S. Hilavin and A. Kustepeli, “Design and implementation of a TEM stripline for EMC testing,” *IEEE Trans. Electromagn. Compat.*, vol. 56, no. 1, pp. 23-27, Feb. 2014.
- [20] P. Kay, “Considerations on a hybrid TEM-reverberation chamber,” *Electromagn. Compat. Symp.*, Adelaide, 2009.
- [21] W. Bittinger, “Properties of open strip lines for EMC measurements,” *Proc. IEEE Int. Symp. Electromagn. Compat.*, Dallas, TX, USA, pp. 120-125, Aug. 1993.



Kai Chen received his M.Eng. degree in Agricultural Mechanization from Yangtze University, Jingzhou, China, in 2014. He is currently pursuing a Ph.D. degree in Electromagnetic Field and Microwave Technology at the College of Electronic and Information Engineering, Nanjing University of Aeronautics and Astronautics. He was an EMC Engineer with H3C, Hangzhou, China, in 2010. He is an Application Engineer with Nanjing Rongce Testing Technology Ltd., Nanjing, China. His main research interests include reverberation chamber and electromagnetic compatibility (EMC).



Wenjun Qi received her B.Eng. degree and M.Eng. degree from Nanjing University of Aeronautics and Astronautics, Nanjing, China in 2018 and 2021, respectively, and she is currently pursuing a Ph.D. degree in Electromagnetic Field and Microwave Technology.

Her main research interests include reverberation chamber, computational electromagnetics and statistical electromagnetics, over-the-air (OTA) testing and electromagnetic compatibility (EMC).



Peng Peng received his M.Eng. Degree from the College of Mechanical Engineering, Southeast University, Nanjing, China in 2010. Prior to 2021, he was an EMC expert at Ford Motor China Engineering Center. He is interested in new EMC solutions for automotive EMC design and validation, and now works for a leading EV company.



Hailong Wang received his B.E. degree from Jinling Institute of Technology, Nanjing, China, in 2019, and his M.Eng. degree from the College of Electronic and Information Engineering from Nanjing University of Aeronautics and Astronautics, China, in 2022. He is currently working as an EMS Engineer. His research interests include liquid antennas, electromagnetic interference and EMC measurement methods.



Xueqi Shen received his M.Eng. degree from the Department of Radio, Southeast University, Nanjing, China, in 1989. He founded the Rongxiang Company in 2004 and Nanjing Rongce Testing Technology Ltd. in 2012, which is an EMC laboratory recognized by Ford and Yutong. Currently, Nanjing Rongce has the largest vehicle reverberation chamber in China. He is currently a Committee Member of Branches A, I, and D of the National Technical Committee on Radio Interference of Standardization Administration of China.



Yongjiu Zhao received his M.Eng. and Ph.D. degrees in Electronic Engineering from Xidian University, Xi'an, China, in 1990 and 1998, respectively. Since March 1990, he has been with the Department of Mechano-Electronic Engineering, Xidian University where he was made a professor in 2004. From December 1999 to August 2000, he was a Research Associate with the Department of Electronic Engineering at The Chinese University of Hong Kong. His research interests include antenna design, microwave filter design and electromagnetic theory.



Qian Xu (Member, IEEE) received his B.Eng. and M.Eng. degrees from the Department of Electronics and Information, Northwestern Polytechnical University, Xi'an, China, in 2007 and 2010, and received his Ph.D. degree in Electrical Engineering from the University of Liverpool, U.K, in 2016. He is currently an Associate Professor at the College of Electronic and Information Engineering, Nanjing University of Aeronautics and Astronautics, China.

He was an RF engineer in Nanjing, China in 2011 and an Application Engineer at CST Company, Shanghai, China in 2012. His work at the University of Liverpool was sponsored by Rainford EMC Systems Ltd. (now part of Microwave Vision Group) and the Centre for Global Eco-Innovation. He has designed many chambers for industry and is the author of the book, *Anechoic and Reverberation Chambers: Theory, Design, and Measurements* (Wiley-IEEE, 2019). His research interests include statistical electromagnetics, reverberation chamber, EMC and over-the-air testing.

Reducing the Measurement Time in a Reverberation Chamber to Less than 1 Second

Wenjun Xia, Wenjun Qi, Feng Fang, Chong Li, Lei Xing, and Qian Xu

College of Electronic and Information Engineering
Nanjing University of Aeronautics and Astronautics, Nanjing, 211106, China
xiawenjun@nuaa.edu.cn, emxu@foxmail.com

Abstract – To increase the speed of the measurement, a time-efficient multi-probe system in a reverberation chamber (RC) is validated. The system consists of 4 printed circuit board (PCB) switches integrating with 128 probe antennas. By using solid-state switches, all antennas can be switched over in sequence in less than 1 second. Typical characteristics of the RC and the total radiated power (TRP) of the device under test (DUT) are performed to verify the validity of this configuration. Compared with the RC using mechanical stirrers, this system shows its superiority in terms of testing efficiency.

Index Terms – measurement technique, multi-probe system, OTA, reverberation chamber.

I. INTRODUCTION

A reverberation chamber (RC) is an electrically large shielded room with mechanical stirrers used to change the field in the chamber [1–2]. With rotated stirrers, a statistically uniform and isotropic environment in the chamber can be created.

In past decades, the RC has been widely applied to both electromagnetic compatibility (EMC) measurements and over-the-air (OTA) testing. It can be used to evaluate the performance of some antennas and devices under test (DUTs), such as radiation efficiency [3–4], radiated emission and immunity tests [5], diversity gain [6], total radiated power (TRP) [7–10], total isotropic sensitivity (TIS) [10–11], and various different fields.

In order to achieve a well-stirred RC for accurate measurements, numerous independent samples are needed. For a typical RC with mechanical stirrers, the measurement is a time-consuming process because the stirrers are rotated with steps. Recently, optimized stirrers have been designed to improve the stirring performance [12]. Meanwhile, the source-stir technique has been applied to improve testing efficiency [13–21]. The multi-probe system, one of the stir techniques, is generally used in the RC [18–21]. By placing several receiving

antennas (source-stirring) on the wall instead of mechanical stirring, both the calibration and other measurements can be performed quickly. In this paper, we design a time-efficient multi-probe system with 128 antenna probes integrated on the 4 PCB switches, which can be used in the RC to perform measurements. The measurement setup is shown in Fig. 1. Instead of using software switching controlled by a computer, digital sequences with a hardware control unit is applied which accelerate the switching process significantly. Important parameters of the RC have been measured to validate its configuration.

This paper is organized as follows: The configuration and design of the multi-probe system are given in Section II. Measurement results such as field uniformity (FU), quality factor (Q factor), and TRP are detailed in Section III. Section IV gives the conclusion.

II. DESIGN AND ANALYSIS

As shown in Fig. 1, the multi-probe system is composed of 4 PCB switches considering the size of the RC. Every PCB switch has 8 single-pole four-throw (SP4T) solid-state switches and 1 single-pole eight-throw (SP8T) solid-state switch, which are used to switch 32 radio frequency (RF) paths. The multi-probe system controller consists of a digital signal generator used to send logic control signals to solid-state switches and a 1 SP4T switch intended for receiving RF signals from the 4 PCB switches. Antenna (Ant) 1 is connected to Port 1 of the vector network analyzer (VNA), the output port of the system controller is connected to Port 2. At each position, we measure S-parameters for 60,001 frequency points in the frequency range of 100 MHz - 6 GHz. The front of the multi-probe PCB switch is illustrated in Fig. 2 (a). The SMA connectors connected with receiving antennas are distributed in the four sides of the PCB. The back of the PCB switch is the control path, which is shown in Fig. 2 (b). Signals on each path need to pass through 1 SP8T solid-state switch, 1 SP4T solid-state switch, and some microstrip lines.

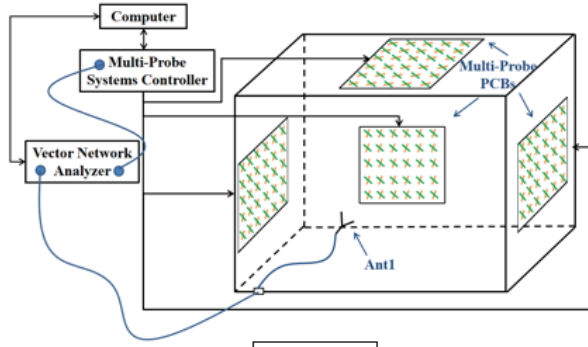


Fig. 1 (a)



Fig. 1 (b)

Fig. 1. Measurement setup: (a) schematic plot. (b) Measurement in multi-probe RC, the inner dimensions of the RC are $1.2 \text{ m} \times 0.8 \text{ m} \times 1.2 \text{ m}$.



Fig 2 (a)

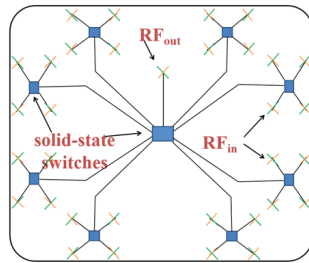


Fig 2 (b)

Fig. 2. The structure of the multi-probe PCB switch: (a) 32 probe antennas integrated on the PCB. (b) The RF paths of the PCB switch.

Generally, an SP4T solid-state switch needs 2 logic control input signals and an SP8T solid-state switch needs 3 logic control input signals. Considering the limited output terminals of the digital signal generator, we utilize an 8-bit output shift register to extend the number of the control signals. Figure 3 shows the system network diagram of the PCB switch. As is shown, the digital

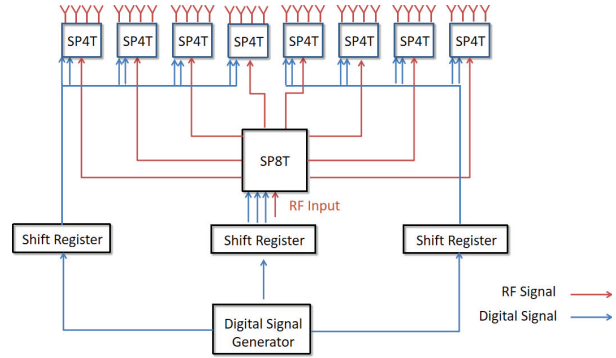


Fig. 3. The system network diagram of the PCB switch.

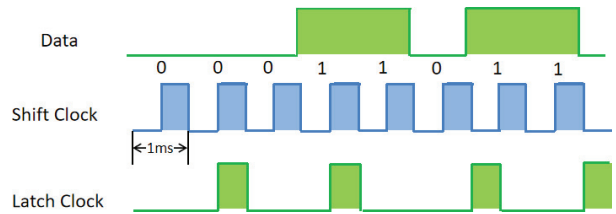


Fig. 4. The schematic diagram of the digital signals to control the SP4T solid-state switch.

signal generator sends data and clock signals to 3 shift registers which are used to control 8 SP4T switches and 1SP8T switch. By toggling the switch state, the RF input signal can arrive at any of the 32 paths. The schematic diagram of the digital signals to control the SP4T switch is shown in Fig. 4. Through setting the interval of the shift clock as 1ms, the data can be output every 2 ms. Thus, the SP4T solid-state switch can alter 4 times within 8 ms. The control of the SP8T solid-state switch is similar to this.

III. MEASUREMENT AND RESULTS

In this paper, we demonstrate the validity of the proposed configuration using a vector network analyzer (VNA). Two parameters of the RC: quality factor and field uniformity are investigated to characterize its performance. The TRP of a DUT has also been measured to show the test efficiency.

Q factor is an important parameter of the RC, which is defined as the ratio of the stored power U to the dissipated power P_l :

$$Q = \frac{\omega U}{P_l}. \quad (1)$$

It is well known that we can also use the time domain (TD) method to calculate Q factor using the following equation (2):

$$Q = \omega \tau_{RC}, \quad (2)$$

where $\omega = 2\pi f$ is the angular frequency, and τ_{RC} is the chamber decay constant. Thus, although measurements

are performed in the frequency domain (FD) through the VNA, we can obtain TD results using the inverse Fourier transform (IFT) to the FD response. The τ_{RC} and Q factor are demonstrated in Fig. 5.

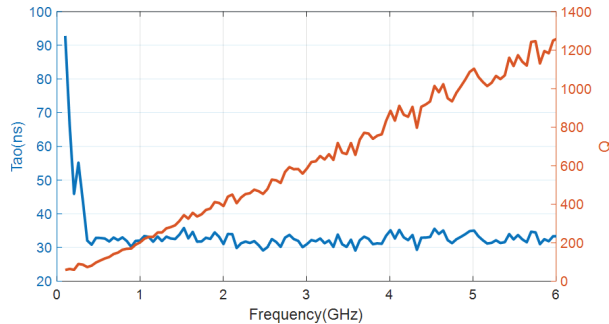


Fig. 5. Measured τ_{RC} and Q factor in the RC.

The FU can characterize the statistical uniformity of an RC, which is defined as the relative standard deviation of the average values obtained at the nine positions in RC [2]. We can judge whether the RC has statistical uniformity according to the tolerance requirements given in the IEC Standard [22]. Due to the limit of the frequency of the solid-state switch, we measure S -parameters for 6,001 frequency points in the frequency range of 100 MHz - 6 GHz. 9 test positions of the working volume are performed resulting in a total of 1152 measurement samples. The FU in the RC compared with the tolerance requirements is demonstrated in Fig. 6. As it shows, the FUs captured from the mean received power are lower than the tolerance requirements in the frequency range, which proves that the proposed system has a good stirring efficiency.

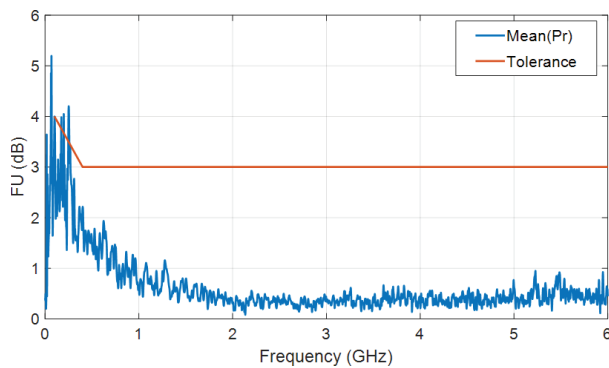


Fig. 6. The FU in the RC compared with the tolerance requirements.

Figure 7 shows the TRP measurement scenario in the RC. In order to explain the calculation process of the TRP clearly, the equations are represented below in decibel (dB) unit. The reference antenna acts as a reference source with known total radiated power (TRP_{Ref}). Once

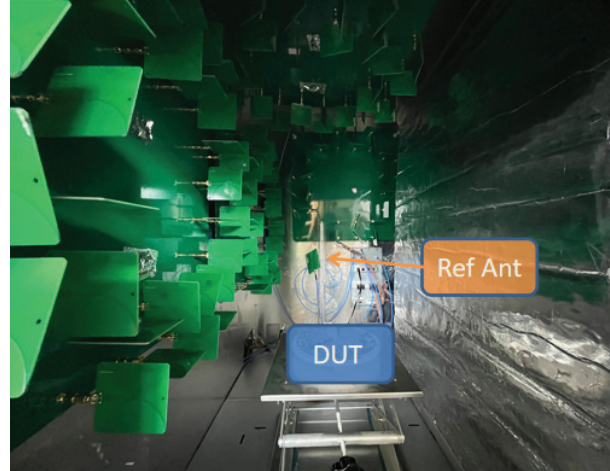


Fig. 7. The TRP measurement scenario in an RC.

averaging the received power from the 128 probe antennas ($\langle P_{RxRef} \rangle$), the chamber transfer function (T_{RC}) can be obtained in dB unit [23]:

$$T_{RC} = \langle P_{RxRef} \rangle - TRP_{Ref}, \quad (3)$$

when the DUT transmits the signals (TRP_{DUT}), a similar procedure has been performed. With the average

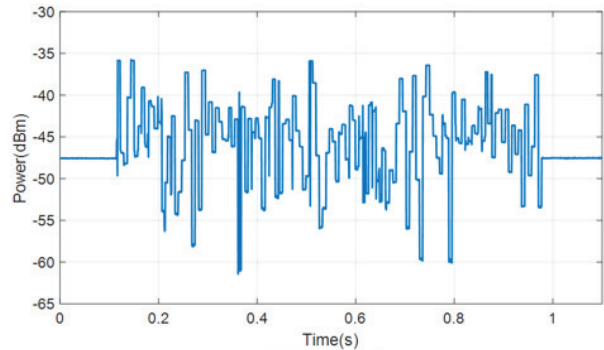


Fig 8 (a)

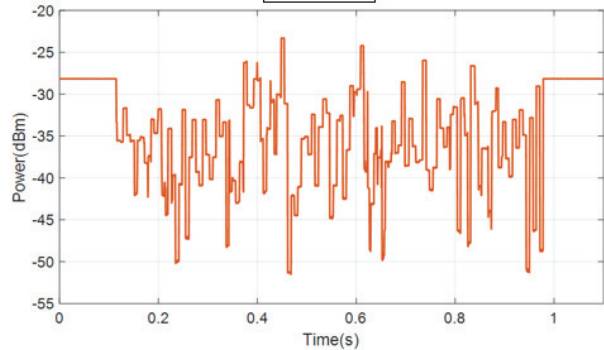


Fig 8 (b)

Fig. 8. The received power sequence from 128 probe antennas in the RC: (a) Ref source. (b) DUT.

received power of the DUT ($\langle P_{RxDUT} \rangle$), the T_{RC} can also be written in dB units:

$$T_{RC} = \langle P_{RxDUT} \rangle - TRP_{DUT}, \quad (4)$$

thus, the TRP of the DUT can be obtained from the equation (3) and (4) in dB units:

$$TRP_{DUT} = \langle P_{RxDUT} \rangle - \langle P_{RxDUT} \rangle + TRP_{Ref}. \quad (5)$$

We record 128 power samples at 2.4 GHz and calculate the TRP of the DUT to verify the high efficiency and accuracy of the proposed configuration. The received power samples in the switching sequence is illustrated in Fig. 8. As can be seen, the total measurement time is less than 1 second.

The cumulative density function (CDF) of the received power is shown in Fig. 9. The measured samples are normalized to the mean value. When the reference antenna is the signal transmitter, it can be considered as a single frequency source. Thus, the received power samples (P_{RxDUT}) is exponential distribution because of the wideband radiated spectrum [23–25]. The TRP of the DUT at 2.4 GHz is also calculated and shown in Fig. 10. With the increasing of the sample number, the average TRP converges to 4.56 dBm.

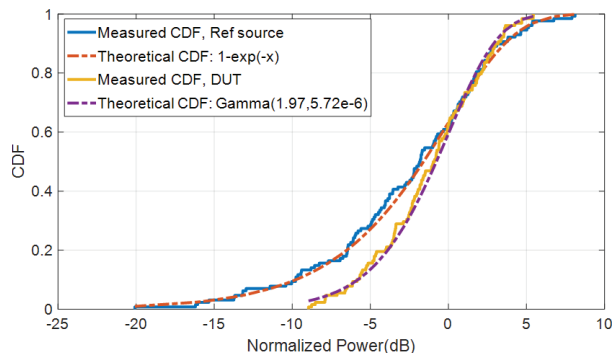


Fig. 9. CDFs of the measured normalized power samples at 2.4GHz.

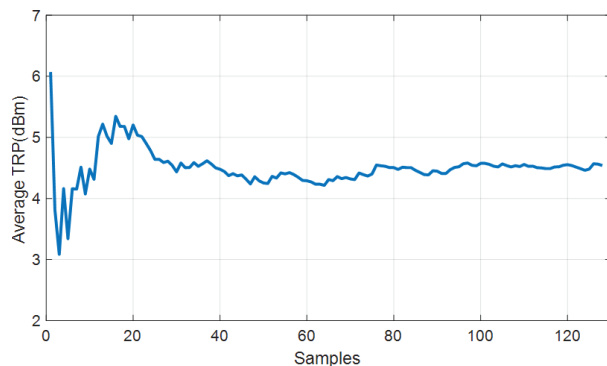


Fig. 10. The average TRP at 2.4GHz, 4.56 dBm.

IV. CONCLUSION

In this paper, we have proposed a multi-probe RC system based on a hardware-switching technique. Compared with conventional mechanical stirrers, the hardware cost is increased for small RCs, but the measurement efficiency is improved greatly. The total measurement time from 128 antennas can be shortened to less than 1 second. Two parameters of the RC and TRP of the DUT have demonstrated the validity of the proposed multi-probe system.

To maintain the measurement accuracy in each time slot, we set the interval of the shift clock to 1 ms. It should be noted that the test time can be further shortened if we decrease the interval of the hardware clock. However, the total time of 1 second is already short enough for most measurements and too short a measurement interval could lead to inaccuracy for some measurements (such as received power, throughput, bit error rate, and error vector magnitude) which require a short time average.

REFERENCES

- [1] D. A. Hill, *Electromagnetic Fields in Cavities: Deterministic and Statistical Theories*, Wiley-IEEE, New Jersey, USA, 2009.
- [2] Q. Xu and Y. Huang, *Anechoic and Reverberation Chambers: Theory, Design and Measurements*, Wiley-IEEE, Chichester, UK, 2019.
- [3] C. L. Holloway, H. A. Shah, R. J. Pirkl, W. F. Young, D. A. Hill, and J. Ladbury, "Reverberation chamber techniques for determining the radiation and total efficiency of antennas," *IEEE Trans. Antennas Propag.*, vol. 60, no. 4, pp. 1758-1770, Apr. 2012.
- [4] W. Xue, Y. Ren, X. Chen, Z. Wang, Y. Li, and Y. Huang, "Measurement uncertainty of antenna efficiency measured using the two-antenna method in a reverberation chamber," *Applied Computational Electromagnetics Society (ACES) Journal*, vol. 36, no. 9, pp. 1152-1158, Sep. 2021.
- [5] G. B. Tait, C. Hager, M. B. Slocum, and M. O. Hatfield, "On measuring shielding effectiveness of sparsely moded enclosures in a reverberation chamber," *IEEE Trans. Electromagn. Compat.*, vol. 55, no. 2, pp. 231-240, Apr. 2013.
- [6] X. Chen, P.-S. Kildal, J. Carlsson, and J. Yang, "MRC diversity and MIMO capacity evaluations of multi-port antennas using reverberation chamber and anechoic chamber," *IEEE Trans. Antennas Propag.*, vol. 61, no. 2, pp. 917-926, Feb. 2013.
- [7] H. G. Krauthauser, "On the measurement of total radiated power in uncalibrated reverberation chambers," *IEEE Trans. Electromagn. Compat.*, vol. 49, no. 2, pp. 270-279, May 2007.

- [8] L. Ma, A. Marvin, Y. Wen, E. Karadimou, and R. Armstrong, "An investigation of the total radiated power of pantograph arcing measured in a reverberation chamber," *International Conference on Electromagnetics in Advanced Applications (ICEAA)*, Palm Beach, Aruba, pp. 550-553, 2014.
- [9] F. Li, S. Huang, W. Xue, Y. Ren, and X. Chen, "Signal and coherence bandwidth effects on total radiated power measurements of LTE devices in reverberation chambers," *IEEE Transactions on Instrumentation and Measurement*, vol. 71, no. 5500503, pp. 1-3, Jan. 2022.
- [10] W. Xue, F. Li, X. Chen, S. Zhu, A. Zhang, and T. Svensson, "A unified approach for uncertainty analyses for total radiated power and total isotropic sensitivity measurements in reverberation chamber," *IEEE Transactions on Instrumentation and Measurement*, vol. 70, no. 1003112, pp. 1-12, Jan. 2021.
- [11] C. Orlenius, P.-S. Kildal, and G. Poilasne, "Measurements of total isotropic sensitivity and average fading sensitivity of CDMA phones in reverberation chamber," *IEEE Antennas and Propagation Society International Symposium*, Washington, DC, USA, pp. 409-412, 2005.
- [12] J. Tang, F. Li, J. Zheng, X. Chen, Y. Li, and J. Chen, "A new mode stirrer design for the reverberation chamber," *Applied Computational Electromagnetics Society (ACES) Journal*, vol. 36, no. 9, pp. 1182-1188, Sep. 2021.
- [13] Y. Huang and D. J. Edwards, "A novel reverberating chamber: the source-stirred chamber," *Eighth International Conference on Electromagnetic Compatibility*, Edinburgh, UK, pp. 120-124, 1992.
- [14] A. De Leo, G. Cerri, P. Russo, and V. M. Primiani, "Experimental comparison between source stirring and mechanical stirring in a reverberation chamber by analyzing the antenna transmission coefficient," *International Symposium on Electromagnetic Compatibility (EMC EUROPE)*, Amsterdam, Netherlands, pp. 677-682, 2018.
- [15] A. De Leo, V. M. Primiani, P. Russo, and G. Cerri, "Optimization techniques for source stirred reverberation chambers," *International Symposium on Electromagnetic Compatibility — EMC EUROPE*, Wroclaw, Poland, pp. 199-204, 2016.
- [16] W. Li, C. Yue, and W. Yu, "Study on array source stirring reverberation chamber," *Applied Computational Electromagnetics Society (ACES) Journal*, vol. 29, no. 12, pp. 1067-1076, Dec. 2014.
- [17] A. Cozza, "Source correlation in randomly excited complex media," *IEEE Antennas Wireless Propag. Lett.*, vol. 11, pp. 105-108, Jan. 2012.
- [18] W. Li, C. Yue, and W. Yu, "Study on array source stirring reverberation chamber," *Applied Computational Electromagnetics Society (ACES) Journal*, vol. 29, no. 12, pp. 1067-1076, Aug. 2021.
- [19] D. Mandaris, R. Vogt-Ardatjew, E. Suthau, and F. Leferink, "Simultaneous multi-probe measurements for rapid evaluation of reverberation chambers," *IEEE International Symposium on Electromagnetic Compatibility and IEEE Asia-Pacific Symposium on Electromagnetic Compatibility*, Suntec City, Singapore, pp. 590-594, 2018.
- [20] D. Mandaris, R. Vogt-Ardatjew, M. Z. Mahfouz, E. Suthau, and F. Leferink, "Time efficient reverberation chamber performance analysis using simultaneous multiprobe measurement technique," *International Symposium on Electromagnetic Compatibility*, Amsterdam, Netherlands, pp. 1-5, 2018.
- [21] W. Qi, F. Fang, W. Xia, Y. Zhao, L. Xing, and Q. Xu, "A compact multi-probe reverberation chamber for over-the-air testing," *Applied Computational Electromagnetics Society (ACES) Journal*, vol. 36, no. 9, pp. 1196-1201, Sep. 2021.
- [22] IEC 61000-4-21, *Electromagnetic Compatibility (EMC) — Part 4-21: Testing and Measurement Techniques — Reverberation Chamber Test Methods*, IEC Standard, Ed 2.0, Jan. 2011.
- [23] Q. Xu, W. Qi, C. Liu, L. Xing, D. Yan, Y. Zhao, T. Jia, and Y. Huang, "Measuring the total radiated power of wideband signals in a reverberation chamber," *IEEE Antennas Wireless Propag. Lett.*, vol. 19, no. 12, pp. 2260-2264, Oct. 2020.
- [24] W. Xue, F. Li, X. Chen, and T. Svensson, "Statistical analysis of measurement uncertainty in total radiated power of wireless devices in reverberation chamber," *IET Microwaves, Antennas & Propagation*, vol. 14, no. 11, pp. 1241-1245, Jun. 2020.
- [25] N. Wellander, M. Elfsberg, H. Sundberg, and T. Hurtig, "Destructive testing of electronic components based on absorption cross section RC measurements," *International Symposium on Electromagnetic Compatibility — EMC EUROPE*, Barcelona, Spain, pp. 778-783, 2019.



Wenjun Xia received his B.Eng. degree in Electronic Information Engineering from Suzhou University of Science and Technology, Suzhou, China in 2020. He is currently pursuing a M.Eng. degree in Electromagnetic Field and Microwave Technology at Nanjing University of Aeronautics and Astronautics, Nanjing, China. His main research interests include reverberation chambers, spatial

channel models, over-the-air testing, and electromagnetic compatibility.



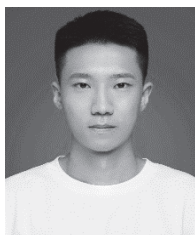
Wenjun Qi received her B.Eng. degree and M.Eng. degree from Nanjing University of Aeronautics and Astronautics, Nanjing, China in 2018 and 2021, respectively. She is currently pursuing a PhD in Electromagnetic Field and Microwave Technology. Her main research

interests include reverberation chambers, computational electromagnetics and statistical electromagnetics, over-the-air testing, and electromagnetic compatibility.



Feng Fang received his B.Eng. degree in Electromagnetic Field and Microwave Technology from Nanjing University of Aeronautics and Astronautics, Nanjing, China in 2020, where he has been currently working toward his M.Eng. His main research

interests include microwave measurement techniques, reverberation chambers, and wireless communication testing, especially over-the-air testing.



Chong Li received his B.Eng. degree in Communication Engineering from Nanchang Hangkong University, Nanchang, China in 2021. He is currently pursuing a M.Eng. degree in Electromagnetic Field and Microwave Technology, Nanjing University of Aeronautics and

Astronautics, Nanjing, China. His research interests include reverberation chambers, phased array systems, electromagnetic compatibility, and antenna design.



Lei Xing received her B.Eng. and M.Eng. degrees from the School of Electronics and Information, Northwestern Polytechnical University, Xi'an, China, in 2009 and 2012. She received her PhD in Electrical Engineering and Electronics at the University of Liverpool, U.K. in 2015.

She is currently an Associate Professor at the College of Electronic and Information Engineering, Nanjing University of Aeronautics and Astronautics, China.



Qian Xu received his B.Eng. and M.Eng. degrees from the Department of Electronics and Information, Northwestern Polytechnical University, Xi'an, China, in 2007 and 2010, and his PhD in Electrical Engineering from the University of Liverpool, U.K. in 2016. He is currently

an Associate Professor at the College of Electronic and Information Engineering, Nanjing University of Aeronautics and Astronautics, China. He was a radio frequency (RF) engineer in Nanjing, China in 2011, an Application Engineer at CST Company, Shanghai, China in 2012. His work at the University of Liverpool was sponsored by Rainford EMC Systems Ltd (now part of the Microwave Vision Group) and the Centre for Global Eco-Innovation. He has designed many chambers for industry and is the author of the book *Anechoic and Reverberation Chambers: Theory, Design, and Measurements* (Wiley-IEEE, 2019). His research interests include statistical electromagnetics, reverberation chambers, electromagnetic compatibility, and over-the-air testing.

Uncertainty Quantification Method of Crosstalk Involving Braided-Shielded Cable

Tianhong Tan¹, Tao Jiang¹, Haolin Jiang², Tianhao Wang², and Mingjuan Cai³

¹College of Information and Communication Engineering
Harbin Engineering University, Harbin, 150001, China
tthjob@163.com, jiangtao@hrbeu.edu.cn

²College of Instrumentation & Electrical Engineering
Jilin University, Changchun, 130000, China
jiang960208@yeah.net, wangtianhao@jlu.edu.cn

³Naval Research Academy, Shanghai, 201105, China
happy_caier@163.com

Abstract – In this paper, in view of the uncertainty of geometric parameters of braided-shielded cable and structural parameters of the shield in practical problems, polynomial chaos expansions (PCE) is used to explore the uncertainty quantification of a crosstalk calculation model of braided-shielded cable. First, the model based on multi-conductor transmission line theory is expanded by PCE. Second, the truncation degrees of polynomials and sample size of PCE are determined by the leave-one-out method, and the statistical characteristic parameters of crosstalk are obtained by combining coefficients of polynomials. Compared with the calculation results of the Monte Carlo method, the mean value, standard deviation and probability density function obtained by the two methods are basically consistent, but the PCE method has obvious advantages in calculation efficiency. Finally, the influence of input variable parameters in the crosstalk calculation model of braided-shielded cable are calculated by combining the PCE and the Sobol's global sensitivity analysis method, which provides theoretical guidance for the electromagnetic compatibility design of electrical and electronic equipment using braided-shielded cable.

Index Terms – braided-shield cable, crosstalk uncertainty quantification, polynomial chaos expansions, Sobol's global sensitivity analysis method.

I. INTRODUCTION

A transmission line is the carrier of electronic signals that play an important role in equipment connection. However, with the high integration of electrical and electronic equipment, the electromagnetic environment (EME) inside the equipment is becoming more and more complex, and the possibility of transmission

signal distortion or mis-operation of equipment caused by electromagnetic interference is also gradually increasing. Under certain conditions, the crosstalk of transmission lines can be calculated based on the transmission line theory (MTL) [1, 2]. However, due to objective reasons such as working environment, working state, and manufacturing process, the relevant parameters of transmission lines show uncertainty, so the uncertainty quantification of transmission lines has become a research hotspot in recent years [3, 4].

Braided-shielded cable is a transmission line wrapped by a metal mesh braid layer, which can shield electromagnetic interference caused by complex EME [5]. Due to its excellent electromagnetic compatibility (EMC) performance, braided-shielded cable is widely used in various fields [6]. As a key parameter affecting the shielding characteristics, transfer impedance has been studied by a large number of researchers. Schelkunoff proposed using surface transfer impedance of shielding cable to describe shielding effectiveness [7]. Subsequently, a complete calculation model of the transfer impedance was established by Vance [8], and the calculation model of the transfer impedance was improved by Sali, Tyni, and Kley [9–11]. Deterministic calculation of crosstalk in braided-shielded cable by combining MTL with transfer impedance calculation model [12]. However, in the actual situation, the geometric parameters of braided-shielded cable and the structural parameters of the shield will show uncertainty [13, 14], which will have an effect on the shielding effectiveness of the shield. Therefore, it is necessary to study the uncertainty quantification of crosstalk of braided-shielded cable. In [15], the influence of shielding material on shielding effectiveness is analyzed based on plane-wave theory. In [16] compared the analysis results

of the sensitivity analysis method based on the BEATRICES analytical model with the results based on MTL repeated analysis and calculation, and concluded that the magnitude of the average height between the carriers strongly determines the value of the transfer impedance at high frequencies. In [17] analyzed the multi-shield cable model and pointed out that the number of shielding layers, the thickness of shielding layer, and the structural parameters of insulating layer were the main parameters affecting the shielding effectiveness.

The existing research on braided-shielded cable is mostly about the qualitative analysis of the influence of shielding layer structure parameters on shielding effectiveness or crosstalk [18], which cannot quantify the uncertainty of the crosstalk of braided-shielded cable. In view of the above problems, this paper proposes to use PCE to quantify the uncertainty of the crosstalk calculation model of braided-shielded cable, and determine the sample size and truncation degree of PCE based on the leave-one-out (LOO) method. This is in view of the successful application of Sobol's global sensitivity analysis method based on variance decomposition in EMC field [19, 20]. In this paper, the Sobol's global sensitivity analysis method is combined with PCE to calculate the global sensitivity indices of input variable parameters and quantify their influence. The statistical characteristic parameters and global sensitivity index are calculated by the PCE method and are compared with results calculated by the Monte Carlo (MC) method to verify the accuracy and efficiency of the Sobol's global sensitivity analysis method based on PCE.

II. TRANSFER IMPEDANCE CALCULATION OF BRAIDED-SHIELDED CABLE

Due to its mechanical flexibility, the braided shielding layer will have holes. The external electric field can penetrate the shielding layer through the holes, resulting in crosstalk on the receptor line protected by the shielding layer [21, 22]. This shielding effectiveness is described by the transfer impedance of the shielding layer. The transfer impedance is determined by the five structural parameters of the shielding layer, which are: radius r_s of the shield, the number of carriers C in the braid, the pitch angle α of the weave, the diameter d of weaving wires, the number N of wires in each carrier. This is shown in Figs. 1 and 2:

The external electromagnetic field penetrates the shielding layer through three mechanisms to generate coupling on the receptor line:

1. Diffusion of the magnetic currents induced in the shield.
2. Penetration of the magnetic field through braid layer diamond-shaped holes.

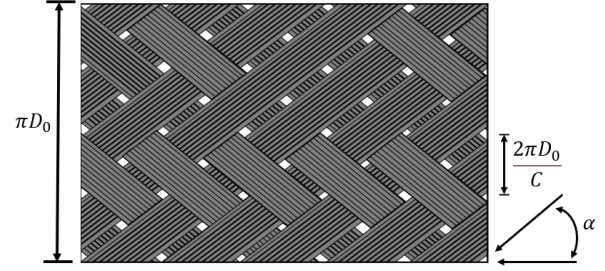


Fig. 1. Braid pattern developed on a plane.

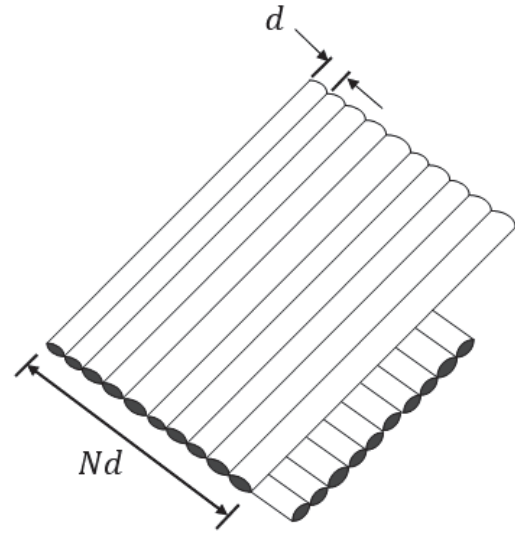


Fig. 2. One diamond of braid.

3. More complex inductance phenomenon caused by overlapping of weaving wires.

The above can be described by the following formula:

$$Z_T = Z_d + j\omega(M_h + M_b). \quad (1)$$

Z_T is the transfer impedance, Z_d represents the diffusion impedance calculation formula, which describes the low frequency characteristics of electromagnetic radiation to the shielding layer, M_h a formula for calculating the hole inductance, which describes the direct leakage of the magnetic field through the diamond-shaped holes in the braid, M_b represents the formula for calculating braided inductance, which is a description of inductance phenomenon. According to the theory of [23], the vortex current of braided carriers produces attenuation of transfer impedance, which is called the extra fluctuation effect M_e :

$$M_e = -\frac{1.16}{CNd} \arctan \frac{N}{3} \sin\left(\frac{\pi}{2} - 2\alpha\right) \sqrt{\frac{\mu}{\sigma}} \sqrt{\omega} e^{j\frac{\pi}{4}}. \quad (2)$$

The improved transfer impedance calculation formula is:

$$Z_T = Z_d + j\omega(M_h + M_h) + M_e. \quad (3)$$

According to the transfer impedance calculated by (3), the outer current of the shielding layer can be connected with the electric field of the inner layer, and the boundary conditions can be obtained. Combined with MTL to calculate crosstalk on receptor line.

III. ANALYSIS METHOD OF UNCERTAINTY QUANTIFICATION

A. Polynomial chaos expansions method

The PCE method has a solid mathematical foundation to describe the randomness of variables with different distributions [24]. The PCE method is equivalent to constructing a surrogate modeling of output variables. Any uncertain information of output variables can be obtained through the surrogate modeling, such as mean, standard deviation and probability density functions. In the construction of the surrogate modeling, PCE is usually truncated at degree p due to the consideration of calculation, and the corresponding p -degree PCE model can be expressed as:

$$Y \approx \sum_{i=0}^p \hat{c}_i \Phi_i(\xi), \quad (4)$$

where \hat{c}_i represents the corresponding coefficients of the multivariate polynomials orthonormal. The multivariate polynomials $\Phi_i(\xi)$ are then assembled as the tensor product of their univariate counterparts ξ_1, \dots, ξ_d , d represents the dimension of the model input.

$$\Phi_i(\xi) = \prod_{k=1}^d \phi_k^i(\xi_k). \quad (5)$$

The number of polynomial coefficients Q in p -degree PCE model can be calculated by the following formula.

$$Q = \frac{(d+p)!}{d!p!}. \quad (6)$$

Next, the samples of PCE need to be sampled in the standard random space. The sampling method used in this paper is Latin hypercube design (LHD) [25]. After obtaining the samples and the response value corresponding to the samples, the PCE coefficients are calculated by the ordinary linear square (OLS) method. As follows:

$$b = (AA^T)^{-1} A^T G. \quad (7)$$

A represents the sample matrix, \hat{b} represents the vector of the coefficients of the polynomial, and G represents the vector of the response value. After the polynomial coefficients of PCE is calculated according to (7), the uncertainty information of output variable can be calculated on the surrogate modeling. The mean and variance of the output variable can be expressed as:

$$E[Y] = c_0, \quad (8)$$

$$V = Var[Y] = \sum_{i \in p, i \neq 0} c_i^2. \quad (9)$$

In order to ensure accuracy and high efficiency, this paper uses the LOO method to determine the truncation degree and sample size of PCE. The process can be simply summarized as the following three steps:

1. Set the sample size to be verified and determine the truncation degree interval.
2. Use the LOO method to calculate the minimum error value of each sample size and the corresponding maximum truncation degree.
3. The error values of the minimum LOO method of each sample size are analyzed, and the optimal sample size is selected.

The error calculation formula of the LOO method is as follows:

$$'O_{LOO} = \frac{\sum_{i=1}^N (M(x^{(i)}) - M^{PC,i}(x^{(i)}))^2}{\sum_{i=1}^N (M(x^{(i)}) - \hat{\mu}_Y)^2}, \quad (10)$$

where $M(x^{(i)})$ represents the response value, $M^{PC,i}(x^{(i)})$ represents the response value calculated by the surrogate modeling constructed after removing sample points numbered i as the training set, $\hat{\mu}_Y$ is the expectation of the original model.

B. Global sensitivity analysis

The global sensitivity analysis can obtain the average sensitivity indexes in the entire distribution of the input variable parameters, and can also measure the effect of interaction between different input variable parameters on the uncertainty of output variables. This paper adopts Sobol's global sensitivity analysis method based on PCE, which is based on variance decomposition and is suitable for independent input variable parameters. Because the basis functions of PCE are mutually orthogonal, Sobol's global sensitivity decomposition can be used in (4) [26], So the first-order Sobol's global sensitivity index based on PCE method is:

$$S_j = \frac{\sum_{j \in d, j \neq 0} c_j^2}{V}, \quad (11)$$

where c_j represents the coefficients of polynomials involving the only j th-dimensional variable. V represents the variance of the output variable, according to (9).

The formula of total global sensitivity index is as follows:

$$S_j^T = \frac{\sum_{j \in d, j \neq 0} (c_j^T)^2}{V}, \quad (12)$$

where c_j^T represents the coefficients of all polynomials involving the j th-dimensional variable.

IV. EXAMPLE APPLICATION

In this section, combined with the PCE method and Sobol's global sensitivity analysis method based on PCE, the uncertainty quantification of the crosstalk model of braided-shielded cable is shown in Fig. 3.

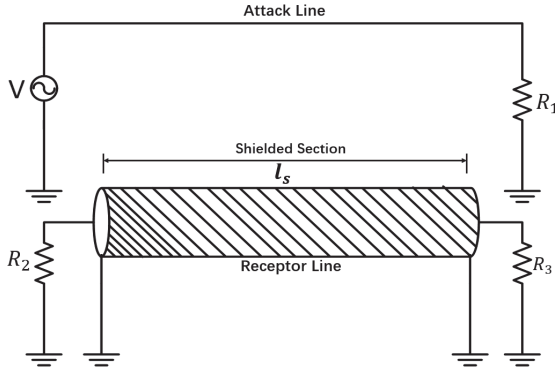


Fig. 3. Braided-shielded cable model.

There are six fixed parameters in the model shown in Fig. 3. The number of carries in the braided C is 16, the number of wires in the carry N is 4, the values of all impedances are 50Ω , and the excitation source amplitude on the attack line is set to 1V. According to the actual situation, the following eight uncertain independent parameters are set as input variable parameters of the model: l_s is the length of receptor line wrapped in braided layer, the distance between the attack line and the receptor line is S , the height of attack line and receptor line from the ground is h , the inner radius of the shielding layer is r_s , the line radius of receptor line and attack line are r_{w1} and r_w respectively. The distributions of input variables are as follows:

Table 1: The distribution of input variables

Random Input Variables	Distributed and Parameters	Unit
l_s	$U(3.45, 3.84)$	m
S	$U(1.42e^{-2}, 1.57e^{-2})$	m
h_g	$U(1.42e^{-2}, 1.57e^{-2})$	m
d	$N(1.27e^{-4}, (6.35e^{-6})^{-2})$	m
r_s	$U(8.44e^{-4}, 9.33e^{-4})$	m
r_{w1}	$N(3.2e^{-4}, (1.6e^{-5})^{-2})$	m
r_w	$N(3.2e^{-4}, (1.6e^{-5})^{-2})$	m
α	$U(\pi/18, \pi/4)$	rad

First, its PCE surrogate modeling is constructed according to the crosstalk calculation model of braided shield cable. When selecting the sample size of PCE, usually select the number of samples twice the number of

polynomials, that is, the sample size is $2Q$. However, this method has its limitations in the model with high dimension and strong nonlinearity. And according to equation (6), the number of coefficients is related to the truncation degree. Using inappropriate truncation degree will not only lead to low computational efficiency, but also cause insufficient calculation accuracy. So, it is important to select the appropriate sample size and truncation degree for the PCE model. Therefore, this paper adopts the LOO method to determine the truncation degree and sample size. Set at frequency point $f = 100kHz$, the sample sizes that need to be verified are 100, 200, 300, 400, and 500. The sample size of each group is analyzed by the LOO method 50 times, and the box plot is as follows:

As can be seen from Fig. 4, when the sample size is 100, 200, 300 using PCE calculation is prone to extreme outliers, and value of Inter-Quartile Range (IQR) of each sample size t is 8.5×10^{-4} , 3×10^{-4} , 7.7×10^{-6} respectively. When the sample size is 400 and 500, the IQR is 4.08×10^{-6} and 4.72×10^{-6} respectively, and there are no extreme outliers. At this time, the maximum truncation degree is 3. Considering the computational cost, the 3-degree truncation and the sample size of 400 should be adopted.

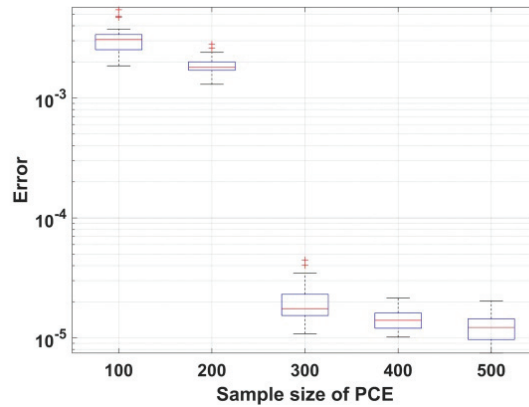


Fig. 4. The box plot of error analysis of the LOO method with different sample sizes.

Second, the calculation accuracy of PCE needs to be verified. The comparison frequency band is set as $[10^2, 10^8]$ Hz, the calculation times of the MC method is 10^3 , and the truncation degree and sample size of PCE are taken as the values verified by the LOO method. The comparison data are the near-end response voltage of the braided-shielded cable model.

As shown in Figs. 5 and 6, the standard deviation and mean value calculated by PCE are basically consistent with those calculated by MC. It can be seen that the application of the PCE method to calculate statistical moments in this model has accuracy. Then select two

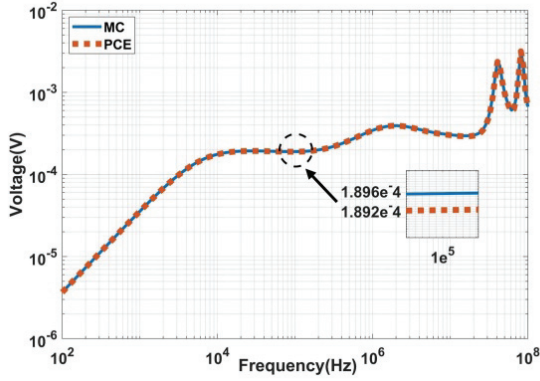


Fig. 5. Comparison between the mean value of near-end response voltage computed MC and PCE.

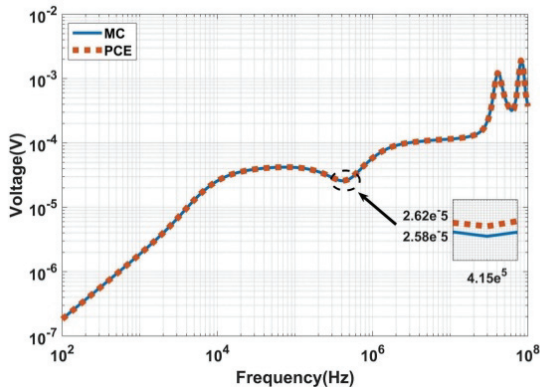


Fig. 6. Comparison between the standard deviation of near-end response voltage computed MC and PCE.

frequency points in $[10^2, 10^8]$ Hz, respectively, using the MC method and PCE method to calculate the probability density function at the frequency points.

It can be seen from Figs. 7 and 8 that the probability density functions of the near-end crosstalk voltage calculated by the PCE and MC methods is consistent. Through the comparison and verification of mean, standard deviation and probability density function, it can be seen that the statistical characteristic parameters calculated by the PCE method and MC method are basically the same, indicating that the accuracy of uncertainty quantification of the braided-shield cable crosstalk model by PCE meets the requirements.

Finally, the efficiency of the PCE method is verified. For calculation, the MC method requires 3398 seconds on an Intel Core i5 2.4GHz, 8-GB RAM computer, while the calculation time of the PCE method is 233 seconds, which is only 6.8 % of the time required by the MC method. This shows that the PCE method is much better than the MC in computational efficiency.

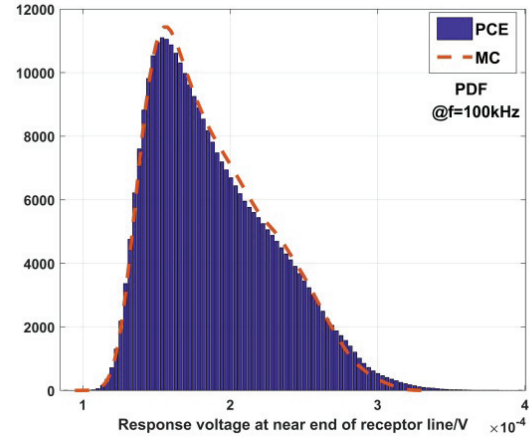


Fig. 7. Comparison between the probability density functions of near-end response voltage computed by MC and PCE at 100kHz.

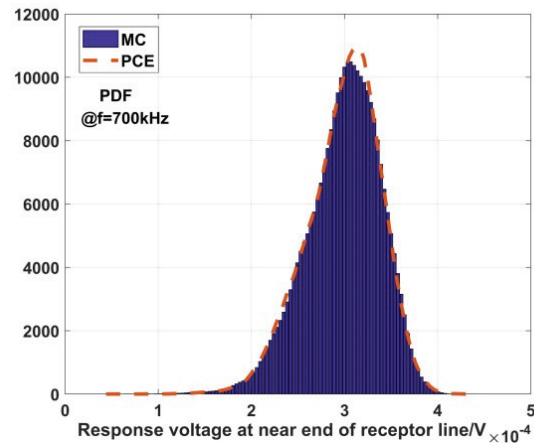


Fig. 8. Comparison between the probability density functions of near-end response voltage computed by MC and PCE at 700kHz.

Next, the Sobol's global sensitivity analysis method based on PCE is used to analyze the global sensitivity of the eight input variables mentioned above, quantifying the influence of input variables on the model. The near-end crosstalk voltage is also selected as the comparison data, and 100kHz is set as the calculation frequency point. The results of global sensitivity analysis based on the MC method are used as comparison data.

Figures 9 and 10 show that the Sobol's global sensitivity analysis method based on PCE at 100kHz is precise, compared with the MC result. It is proved that this method has accuracy in quantifying the uncertainty of the braided-shielded cable crosstalk model. In addition, it can be seen from the information given in the graphs

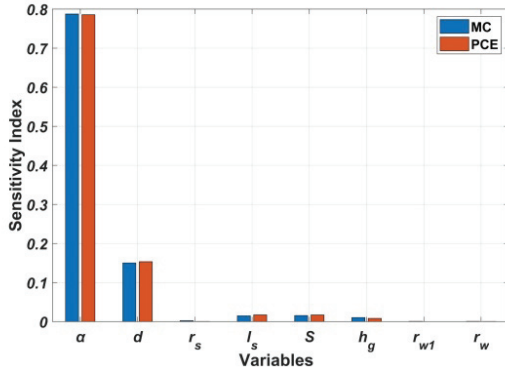


Fig. 9. The global first-order sensitivity index at 100kHz.

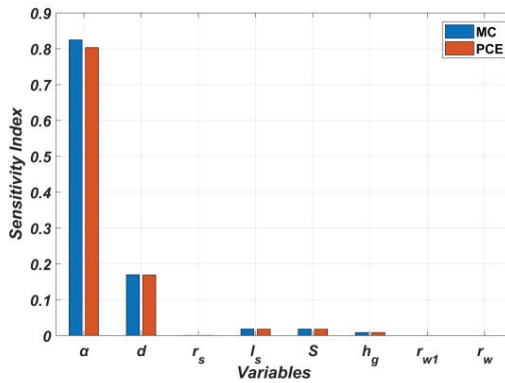


Fig. 10. The global total sensitivity index at 100kHz.

that the weaving angle α has the greatest influence at 100kHz, followed by the diameter of the braided wire d . At high frequency section, the transfer impedance consists of most of the hole inductance and braid inductance and a small part of the diffusion impedance.

In order to accurately show the influence of each input variable parameter on the model at different frequencies. Using Sobol's global sensitivity analysis method based on PCE for each input variable in frequency band $[10^2, 10^8]$ Hz.

As shown in Fig. 11, when the crosstalk calculation model of braided-shielded cable is in the frequency range $[10^2, 6.3e^3]$ Hz, l_s and S and h_g have great influence on the model. Because in the low frequency state, crosstalk is mainly composed of inductive coupling, l_s and S and h_g are the three important parameters determining inductive coupling. When the frequency is greater than 6.3kHz, α and d become important factors affecting the output variable, and the growth of α is particularly obvious. It shows that in the process of increasing frequency, most of the crosstalk is converted from inductive coupling to capacitive coupling. The shielding layer

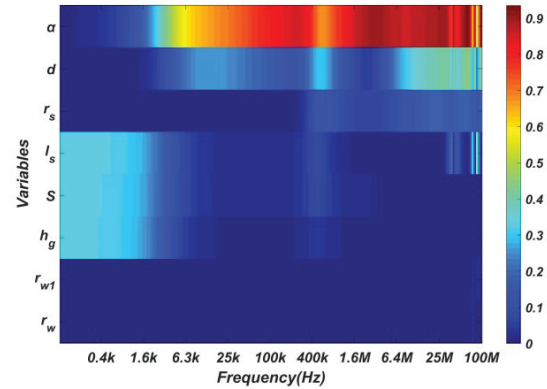


Fig. 11. Global total sensitivity index of input variables in $[10^2, 10^8]$ Hz.

of braided-shielded cable can greatly weaken capacitive coupling. The change of shielding layer structure parameter α , r_s and d affects the shielding effectiveness, and then affects the crosstalk received by the receptor line. The higher the frequency, the more obvious the effect. In addition, the effects of r_{w1} and r_w on the model are not significant.

V. CONCLUSION

In this paper, the uncertainty quantification problem of the crosstalk calculation model of braided-shielded cable is studied. The model with infinite ground as a reference conductor is adopted to make the input variable parameters obey different distributions. The uncertainty of the model is quantified by the PCE method, and the relevant statistical quantities such as the mean, standard deviation and probability density functions of the near-end crosstalk voltage of the receptor line, are obtained. The computed statistical quantities using PCE were validated by the classical MC method. This proves that the PCE method can greatly improve the calculation efficiency while ensuring the calculation accuracy by simplifying the model, and realize the uncertainty quantification of the crosstalk calculation model of braided-shielded cable. Finally, the global total sensitivity index and global first-order sensitivity index of the relevant input variable parameters in the crosstalk calculation model of braided-shielded cable are calculated by combining the PCE method and the Sobol's global sensitivity analysis method. Thus the influence degree of the relevant parameters on the braided-shielded cable crosstalk is obtained. Feasibility is also verified by the MC method. Therefore, the uncertainty quantification method and the global sensitivity analysis method proposed in this paper can provide an effective basis for the EMC design of electrical and electronic equipment with braided-shielded cables.

ACKNOWLEDGMENT

This paper is funded by the Harbin Engineering University high-level scientific research guidance special “urgent solution” research plan (3072022 QBZ0804) and the Key Laboratory of Advanced Marine Communication and Information Technology, Ministry of Industry and Information Technology, Harbin Engineering University, Harbin, China. This paper is also supported by the Shanghai Aerospace Science and Technology Innovation Fund under Grant SAST2019-002.

REFERENCES

- [1] C. R. Paul, “Solution of the transmission-line equations for three conductor lines in homogeneous media,” *IEEE Transactions on Electromagnetic Compatibility*, vol. EMC-20, no. 1, pp. 216-222, Feb. 1978.
- [2] Y. Zhao, Y. Li, and L. Zhao, “A G-shaped defected isolation wall for mutual coupling reduction between patch antenna and microstrip transmission line,” *IEEE 7th Asia-Pacific Conference on Antennas and Propagation*, Auckland, New Zealand, 2018.
- [3] L. Gao, Q. Yu, D. Wu, T. Wang, X. Yu, Y. Chi, and T. Zhang, “Probabilistic distribution modeling of crosstalk in multi-conductor transmission lines via maximum entropy method,” *IEEE Access*, vol. 7, pp. 103650-103661, Jul. 2019.
- [4] Q. Yu, W. Liu, K. Yang, X. Ma, and T. Wang, “Uncertainty quantification of the crosstalk in multiconductor transmission lines via degree adaptive stochastic response surface method,” *Applied Computational Electromagnetics Society (ACES) Journal*, vol. 36, no. 2, pp. 174-183, Feb. 2021.
- [5] Y. Zhao, Y. Li, W. Shi, and W. Yu, “Mutual coupling reduction between patch antenna and microstrip transmission line by using defected isolation wall,” *Applied Computational Electromagnetics Society (ACES) Journal*, vol. 34, no. 1, pp. 100-106, Jan. 2019.
- [6] M. Zhao, S. Xie, D. Su, and H. Sun, “Electromagnetic compatibility predesign for satellite secondary electrical power supply,” *Acta Aeronautica et Astronautica Sinica*, vol. 32, no. 5, pp. 849-856, May 2011.
- [7] S. A. Schelkunoff, “The electromagnetic theory of coaxial transmission lines and cylindrical shields,” *Bell System Technical Journal*, vol. 13, no. 4, pp. 532-579, Oct. 1934.
- [8] E. F. Vance, “Shielding effectiveness of braided-wire shields,” *IEEE Transactions on Electromagnetic Compatibility*, vol. EMC-17, no. 2, pp. 71-77, May 1975.
- [9] S. Sali, “An improved model for the transfer impedance calculations of braided coaxial cables,” *IEEE Transactions on Electromagnetic Compatibility*, vol. 33, no. 2, pp. 139-143, May 1991.
- [10] M. Tyni, “The transfer impedance of coaxial cables with braided outer conductor,” *Proc. 3rd Wrocław Symposium on Electromagnetic Compatibility*, Wrocław, Poland, pp. 410-418, 1976.
- [11] T. Kley, “Optimized single-braided cable shields,” *IEEE Transactions on Electromagnetic Compatibility*, vol. 35, no. 1, pp. 1-9, Feb. 1993.
- [12] C. R. Paul, “Transmission-line modeling of shielded wires for crosstalk prediction,” *IEEE Transactions on Electromagnetic Compatibility*, vol. EMC-23, no. 4, pp. 345-351, Nov. 1981.
- [13] Z. Fei, H. Yi, and J. Zhou, “Crosstalk variations caused by uncertainties in three-conductor transmission lines,” *Loughborough Antennas & Propagation Conference, LAPC. IEEE*, Loughborough, UK, pp. 1-5, Jan. 2016.
- [14] A. Tsaliovich, *Cable Shielding for Electromagnetic Compatibility*, Chapman and Hall, New York, 1995.
- [15] P. V. Y. Jayasree, B. P. Rao, and P. Lakshman, “Analysis of shielding effectiveness of single, double and laminated shields for oblique incidence of EM waves,” *Progress in Electromagnetics Research B*, vol. 22, no. 22, pp. 187-202, Jan. 2010.
- [16] J. L. Rotgerink, J. Verpoorte, and H. Schippers, “Uncertainties in coaxial cable transfer impedance,” *IEEE Electromagnetic Compatibility Magazine*, vol. 7, no. 3, pp. 83-93, Oct. 2018.
- [17] M. Xu, Y. Wang., X. Li, X. Dong, H. Zhang, H. Zhao, and X. Shi, “Analysis of the influence of the structural parameters of aircraft braided-shield cable on shielding effectiveness,” *IEEE Transactions on Electromagnetic Compatibility*, vol. 62, no. 4, pp. 1028-1036, Jul. 2019.
- [18] Y. Zhao, Y. Li, L. Zhao, V. Mordachev, and E. Sinkevich, “Equivalent circuit model for closely spaced patch antenna and microstrip line with loaded defected microstrip structure,” *Cross Strait Quad-Regional Radio Science and Wireless Technology Conference*, Xuzhou, China, Jul. 2018.
- [19] S. Lum, M. Nakhla, and Q.-J. Zhang, “Sensitivity analysis of lossy coupled transmission lines with nonlinear terminations,” *IEEE Transactions on Electromagnetic Compatibility*, vol. 42, no. 4, pp. 607-615, Apr. 2002.
- [20] A. Kouassi, J. Bourinet, S. Lalléchère, P. Bonnet, and M. Fogli, “Reliability and sensitivity analysis of transmission lines in a probabilistic EMC context,” *IEEE Transactions on Electromagnetic*

Compatibility, vol. 52, no. 2, pp. 561-572, Apr. 2016.

- [21] X. Liu, Y. Li, Y. Zhao, L. Zhao, V. Mordachev, and E. Sinkevich, "Equivalent circuit model of crosstalk reduction parallel transmission lines with defected microstrip structures," *Cross Strait Quad-Regional Radio Science and Wireless Technology Conference*, Xuzhou, China, pp. 21-24, Jul. 2018.
- [22] X. Liu, Y. Li, Y. Zhao, and L. Zhao, "Crosstalk reduction design and analysis of the planar meander transmission lines," *International Symposium on Antennas and Propagation*, Busan, South Korea, pp. 23-26, Oct. 2018.
- [23] F. M. Tesche, M. Lanoz, and T. Karlsson, *EMC Analysis Methods and Computational Models*, Wiley, New York, 1997.
- [24] D. Xiu and G. Karniadakis, "Modeling uncertainty in flow simulations via generalized polynomial chaos," *Journal of Computational Physics*, vol. 187, no. 1, pp. 137-167, 2003.
- [25] M. D. McKay, R. J. Beckman, and W. J. Conover, "A comparison of three methods for selecting values of input variables in the analysis of output from a computer code," *Technometrics*, vol. 21, no. 2, pp. 239-245, May 1979.
- [26] I. M. Sobol, "Sensitivity analysis for non-linear mathematical models," *Mathematical Modelling and Computational Experiment*, vol. 1, pp. 407-414, 1993.



Tianhong Tan received his B.S. degree in Electrical Engineering from Jilin University, Changchun, Jilin, China, in 2014. He is currently pursuing a Ph.D. degree in Information and Communication Engineering at Harbin Engineering University. His research interests include electromagnetic compatibility, electromagnetic simulation, and effectiveness evaluation.



Tao Jiang received his Ph.D. degree from Harbin Engineering University, Harbin, China, in 2002. Since 1994, he has been a Faculty Member of the College of Information and Communication, Harbin Engineering University, where he is currently a Professor. He was a Postdoctoral Researcher with the Research Institute of Telecommunication, Harbin Institute of Technology, Harbin,

China, from 2002 to 2003, and a Visiting Scholar with the Radar Signal Processing Laboratory, National University of Singapore, from 2003 to 2004. His current research interests include radio wave propagation, complex electromagnetic system evaluation, modeling, and simulation.



Haolin Jiang received his B.S. degree from the Department of Electrical Engineering, Southwest Jiaotong University, Chengdu, Sichuan, China, in 2018 and his M. S. degree from the College of Electrical and Computer Science, Jilin Jianzhu University, Changchun, China, in 2022. He is currently pursuing a Ph.D. degree in Electrical Engineering at Jilin University. His research interests include lightning electromagnetic fields evaluation and electromagnetic compatibility.



Tianhao Wang received his B.S. degree in Electrical Engineering and his Ph.D. degree in Vehicle Engineering from Jilin University, Changchun, Jilin, China, in 2010 and 2016, respectively. From 2016 to 2019, he was a Postdoctoral Researcher with the Department of Science and Technology of Instruments, Changchun, Jilin University. He is currently an associate professor with the College of Instrumentation and Electrical Engineering, Jilin University. His research interests include the uncertainty quantification of wireless power transfer of EVs and human electromagnetic exposure safety.



Mingjuan Cai received her Ph.D. degree from the National University of Defence Technology, Changsha, China, in 2006. She works with the Naval Research Academy as a Senior Engineer. Her current research interests include electromagnetic simulation, electromagnetic compatibility and evaluation.

Recent Developments of Shielding Effectiveness for Electronics and Information Devices

Ping Xu¹, Tao Jiang¹, Meiyu Wang¹, Yingsong Li^{2,*}, and Zhixiang Huang²

¹College of Information and Communication Engineering
Harbin Engineering University, Harbin, 150001, China

²Key Laboratory of Intelligent Computing and Signal Processing
Ministry of Education, Anhui University, Hefei 230601, China

*liyingsong@ieee.org

Abstract – With the increase wireless communications, many wireless devices and equipment have been invented for special applications, resulting in mutual interference that might destroy the systems or distort signal in-transmission. One of the effective methods to reduce or eliminate interference is to devise a shielding to block the unwanted interference in between the approaching systems, circuits, devices, etc. Thus, shielding and estimation of its effectiveness are very important in order to protect the information devices from potential interference and to improve the performance of information equipment. In this survey, we present the recent developments of the shielding and shielding effectiveness techniques and methods, and give a design for an electromagnetic shielding structure.

Index Terms – electromagnetic shielding, shielding effectiveness, shielding methods, shielding technique.

I. INTRODUCTION

With the increment of electronic devices and information equipment, uncertain interference might give a destroy or reduce the performance of electronic systems, chips, broads and devices, which can be classified into electromagnetic pulses, lighting, natural or artificial strong electromagnetic interference [1-10]. In recent years, much interference from wireless systems like 4G and 5G will also affect other electromagnetic devices. Fortunately, these systems don't give out strong interference, which is easy to filter out. With the development of high power microwave equipment, strong electromagnetic pulse or interference poses a huge threat to the general operation of electronic equipment [11]. Thus, electromagnetic protection and electromagnetic shielding are vital to reduce the loss caused by these threats.

To give protection from the potential interference, many shielding techniques and shielding methods have

been presented, including metal meshes [11], metal plates [12], frequency selective surface (FSS) [13], metal shells [14], and meta-materials [1, 15]. Motivated by these techniques, the shielding methods moves to low cost or high performance for protecting the information devices. Although these techniques or methods are useful for providing desired shielding to protect information devices from electromagnetic radiation that causes harm to hardware systems, components or printed circuit boards, some of them are not effective for practical engineering applications. Thus, the shielding effectiveness of these techniques and methods is required for engineers to select a suitable solution for practical engineering applications.

Recently, more attention has been paid to shielding effectiveness to discuss how to choose a metal mesh or different shielding structures for realization of engineering applications [16-18]. Many shielding effectiveness methods are presented, like the impedance calculation using average field theory [18]. However, the analysis models are not accurate enough for the different size of the meshes to analyze the shielding effectiveness [19-20]. The equivalent transmission line method [19-20] was used for giving an analysis of the double-layer metal meshes, but it failed to get a solution for a wide band of frequency in its engineering to be accurate. In addition, low simulation speed and large computation consumption made these methods difficult to get quick results for different structures and sizes of shielding [16]. Many effective computation methods were then investigated for complex structures with multi-layers and applications in wide frequency bands.

Additionally, many new structures for shielding applications were also presented, like the frequency selective surface (FSS) [13, 21], LC coil [22], diode grids [23], magnetic shielding techniques [24-25]. Also, the related analysis methods are given for various applications to discuss the shielding effectiveness. To get

the results, many analysis methods are also discussed by considering the structure parameters using the finite-difference time-domain method (FDTD) [26-27] and finite element method [28-29]. Additionally, the time-frequency domain shielding effectiveness analysis of the shielding structures and the magnetic shielding measurement with low frequency are also carried out to improve the performance of the shielding.

In this review, the recent developments of the shielding methods and shielding effectiveness analysis techniques will be presented and investigated to illustrate the performance of the shielding.

II. SHIELDING TECHNIQUES AND METHODS

A. Metal meshes

As we know, shielding is to prevent undesired interference from the environment, in order to protect the information devices. Thus, a great number of techniques and methods have been put forward to provide a safety measure to guarantee that the devices avoid microwave radiation attacks [21-25]. Furthermore, an electromagnetic wave has a different skin effect when it is transmitted from air to substrate. If it incidents into the metal, it will be blocked and it is difficult to penetrate the metals that will provide a good shielding. Thus, metal or metal shells [14] are used to construct a shielding structure. However, these structures are heavy and will waste metal materials, which also increases the cost for the design of a shielding structure. In order to reduce the cost and inherent performance of the metal shells in practical engineering, metal meshes are proposed with different analysis methods [10], shown in Fig. 1.

Using related techniques and methods, a variety of metal meshes with single or multi-layers have been presented and their shielding effectiveness have been investigated using different methods.

B. Frequency selective surfaces (FSSs)

Recently, another effective shielding has been proposed with a periodic array structure to provide a behavior of spatial filtering, which is known as frequency selective surface (FSS) [13, 21]. As we all know, FSS can be designed to have a band-stop characteristic to filter or block unwanted frequency bands with a stable angle characteristics. Thus, FSS has been used for shielding to protect the sensitive electronics components enabling them avoid electromagnetic interference (EMI) or radio frequency interference (RFI) in consumer or industrial electronic systems, as well as military and emergency systems.

One of the designs of the FSSs is presented in Fig. 2, where the cell of the FSS and the circuit extraction of the FSS cell is also given [29]. From the circuit analysis of the FSS, we can see the filter characteristics

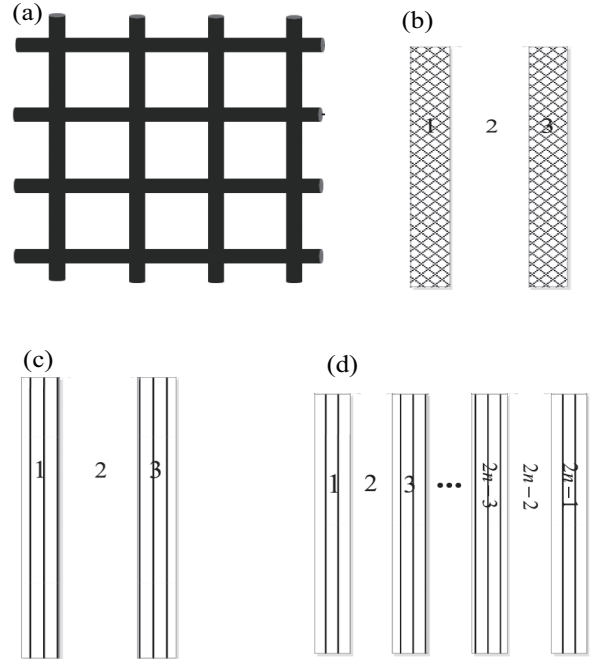


Fig. 1. Geometries of metal meshes [10]. (a) Planar square metal mesh with holes. (b) Double-layered metal plates. (c) Double-layered metal meshes. (d) Multi-layered metal meshes.

clearly. Additionally, we found that the FSS can provide an additional degree of freedom to precisely control the frequency response. It can easily select the desired frequency band and reject the unwanted band, which can filter the incident electromagnetic wave via designing the FSS geometry and arrangement of the FSS cells.

C. Braided shielding structures

As we know, cables are useful for information devices not only in low frequency but also in high frequency, and they can work in a wide frequency. Many braided structures have been proposed and investigated for cables [30-32]. Figure 3 shows a typical braided structure. By using these braided shielding structures, most of the low frequency interference can be filtered.

D. Coil shielding structures

The magnetic field can also be cancelled using shielding coils excited by an auxiliary source, and many coil shielding techniques are also presented and investigated via optimizing the phase and magnitude of the current in the coils to suppress the flux density. In addition, the coil couplings can be weakened using metal plates. Figure 4 shows an improved reactive hybrid shielding with an LC coil structure, where aluminum is designed as the ring shape and placed to surround the LC coil [22].

In this improved reactive hybrid shielding structure with an LC coil, an application with the equivalent

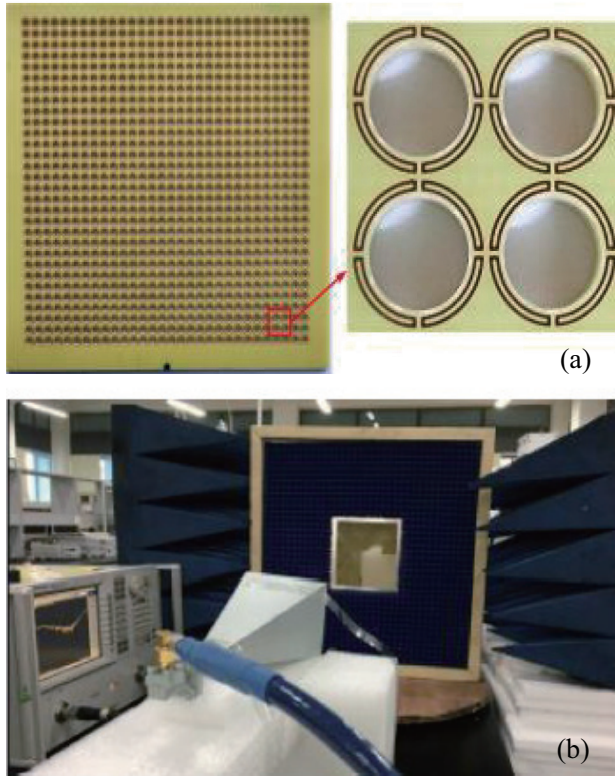


Fig. 2. FSS shielding structure [21]. (a) 3-D FSS cell. (b) Circuit model of the FSS cell. (c) Equivalent circuit of the FSS structure.

circuit for a WPT system with LC shielding coil is also given in Fig. 4. The conventional horizontal aluminum plate (HALP) is equivalent to a vehicle chassis to improve the performance using a vertical aluminum plate (VALP) [22]. In addition, there are also shielding methods using diode grids, metal plates with slots, shielding for orbital angular momentum waves, materials, and meta-materials.

III. SHIELDING EFFECTIVENESS ANALYSIS

With the developments of the shielding techniques and the methods used in the shielding and the electromagnetic computation methods, various shielding effectiveness analysis methods have been proposed and investigated for different applications, including the finite-difference time-domain method (FDTD) [26–27], the method of moments [28–29], time domain integral equation method [33], transmission-line model method [34], and time-frequency methods [35].

A. Model analysis method

To obtain the performance of shielding effectiveness, a lot of models have been presented and investigated in detail. Recently, a model was used to get a rea-

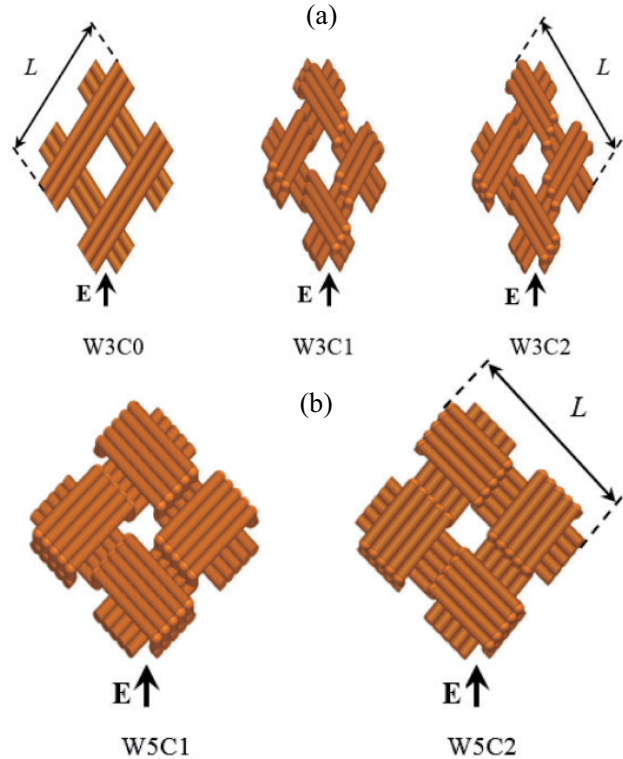


Fig. 3. Braided shielding structure [31]. (a) Geometry of planar braids with three wires per carrier, without (W3C0) and with curvatures (W3C1 and W3C2). (b) Geometry of dense braids with five wires per carrier and with curvatures (W5C1 and W5C2).

sonable approximation to evaluate the shielding effectiveness of a rectangular enclosure filled with conductive plates and the computation results were compared with the finite element method (FEM) [12, 28–29]. The model is given in Fig. 5. The computation results obtained from the model agree well with the FEM simulation, which also help to verify the effectiveness and correctness of the model [12].

B. Time-domain analysis of the shielding effectiveness

In this subsection, we introduce an improved half-space FDTD method to replace the half-space Green's function, where generalized transition matrix (GTM) method combined with Fourier transform is used to get the reflection coefficient [35]. In the computations, multi-direction and multi-polarization incident waves are considered for the total-field/scattered-field (TF/SF) given in Fig. 6 in the FDTD. Based on the modified FDTD method, it is applied to a typical half-space composite electromagnetic problem to get the time-domain shielding effectiveness of the shielding enclosure. The results show that the modified method without complex half-space Green's function has low complexity

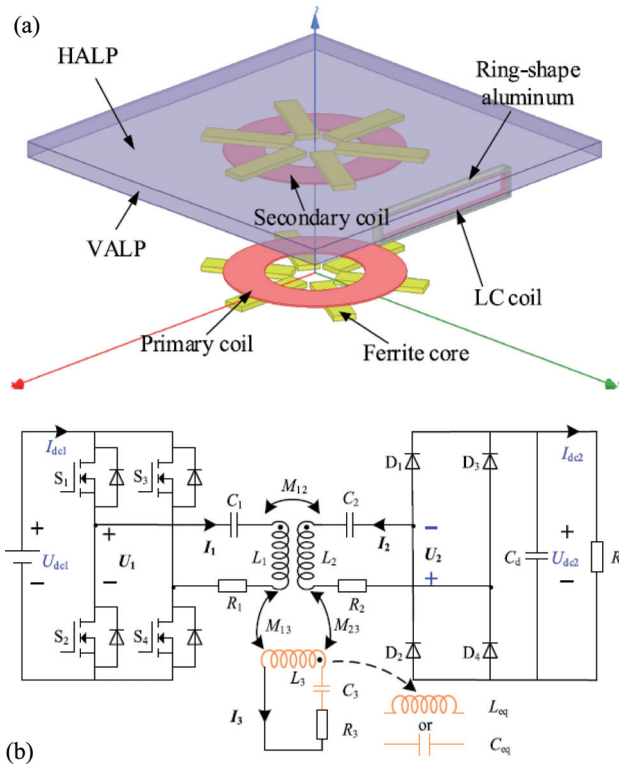


Fig. 4. Improved reactive hybrid shielding structure with an LC coil [22]. (a) Overall view of the improved reactive hybrid shielding with an LC coil structure. (b) Equivalent circuit of a reactive shielding system.

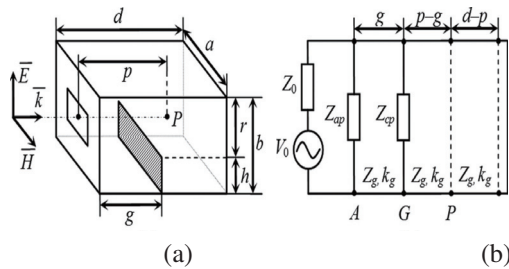


Fig. 5. Model for shielding effectiveness analysis of a rectangular enclosure filled with conductive plates [12]. (a) Metal rectangular enclosure with metal plates. (b) Equivalent circuit for getting the shielding effectiveness via computations.

compared to the traditional half-space algorithms. In addition, the proposed method can be used for different models, incident conditions, and complex environments.

C. Time-frequency analysis methods

Time-domain analysis always considers electromagnetic pulse (EMP) excitation, which has been used in waveform and spectra [36]. As for shielding against EMP, enclosures with small apertures are convention-

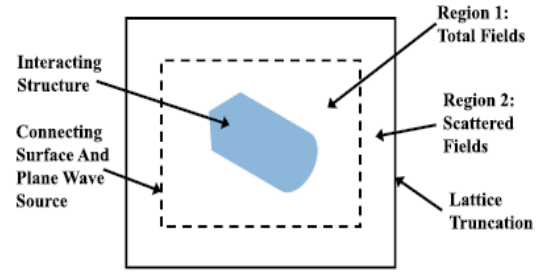


Fig. 6. Zoning of total-field and scattered-field regions [35].

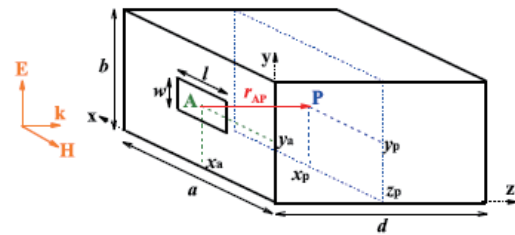


Fig. 7. Schematic of excitation of a rectangular enclosure with an aperture [36].

ally of applicable interest, and the image method limits the application for a large number of dipole images. Recently, for simply estimating time domain shielding effectiveness data of metallic enclosures under EMP excitation and further correlating these data to frequency domain, an analysis between the time and frequency domain for shielding effectiveness is presented and investigated for analyzing the metal enclosures with different apertures, where the analytical formulas for estimating time domain SE data against EMP excitation is also included and derived to analyze the metal enclosures.

The improved method in Fig. 9 is implemented based on the analysis of the transient process at the aperture and an equivalent magnetic current source [36]. Also, only direct emission from the aperture is considered and the equivalent circuit model for frequency domain shielding effectiveness data is used to get the correlation between the time and frequency domain. The simulations are presented to verify the analysis and the simulation agrees well with the analysis.

IV. TIME-DOMAIN SHIELDING EFFECTIVENESS MEASUREMENT

As we know, shielding effectiveness can be measured when a small shielding enclosure is made using frequency-domain techniques under the standard of IEEE 299.1. However, the high level of the shielding effectiveness under a high power microwave or a

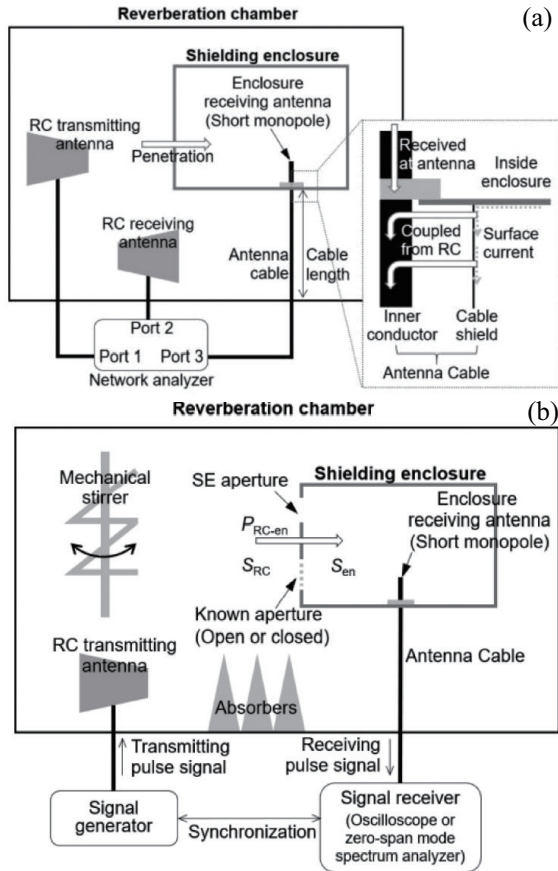


Fig. 8. Popular shielding effectiveness measurement method with frequency and time domain methods [37]. (a) IEEE 299.1 frequency-domain shielding effectiveness measurement method. (b) Time-domain shielding effectiveness measurement method.

directed-energy weapon will reduce the measurement dynamic range of the equipment for shielding effectiveness measurement, which is caused by the cable loss in the signal transmission during the shielding effectiveness measurement [37]. In this section, a time-domain shielding effectiveness measurement method is reviewed in order to achieve high accuracy for a high level shielding effectiveness measurement.

For the frequency-domain shielding effectiveness measurement method, the shielding effectiveness measurement should use a wide dynamic range to get an accurate measurement, where the wide dynamic range is obtained by comparing it to the receiving powers that are obtained before and after replacing a receiving antenna inside an enclosure with a load [37]. In this case, the dynamic range is always reduced by coupling from the cables. In the presence of the shielding effectiveness measurement, continue wave is used to measure the revived power, which will also be coupled into the

measurement resulting in dynamic range reduction.

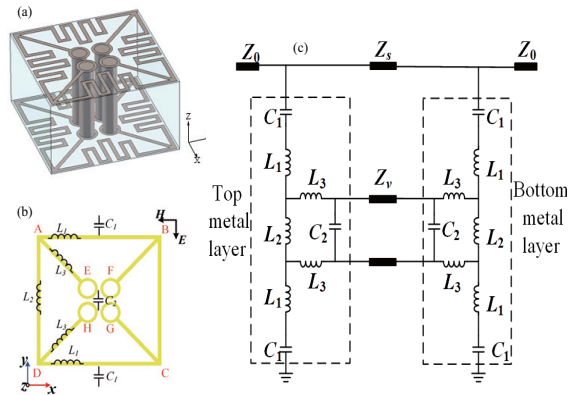


Fig. 9. FSS shielding structure [38]. (a) 3-D FSS cell. (b) Circuit model of the FSS cell. (c) Equivalent circuit of the FSS structure.

For the time-domain shielding effectiveness measurement method, a modulated pulse is used as a transmitting signal in a nested reverberation chamber rather than continue wave signal [37]. When the pulse signal is completely transmitted, the receiving signal is obtained inside the shielding enclosure in the time domain, which is defined as the enclosure response that is used to calculate the shielding effectiveness enclosure. Thus, the measured enclosure response is not affected by the transmitting signal, and hence, the dynamic range for the shielding effectiveness measurement will be unchanged.

V. AN EXAMPLE FOR DEVELOPING FSS SHIELDING STRUCTURE

Since FSS is also useful for shielding effectiveness and most of the FSS only provide a single frequency band with planar structure, we designed a 3-D FSS to mimic the size of the structure [38]. The presented structure is given in Fig. 9 with equivalent circuit of the FSS cell. The designed FSS is printed on a two-layered F4B substrate. To use the FSS cell developed in Fig. 9, a dual-band FSS is presented and given in Fig. 10 (a). The FSS is investigated, fabricated and measured in a chamber. The results shown in Fig. 10 (b) demonstrate that the FSS has good dual-band band-pass performance and the rejected band is wide enough to block the interference from 7GHz to 14GHz. In comparison with the simulations, the band-pass band has been broadened and the bandwidth for the first band-pass is narrowed. There is some difference between the measurement and the simulation, which might be caused by the fabrication and measurement errors. In addition, the FSS can still cover a wide -10dB bandwidth when the incident angle is 40° [38]. Also, in the future, the shielding could be applied in

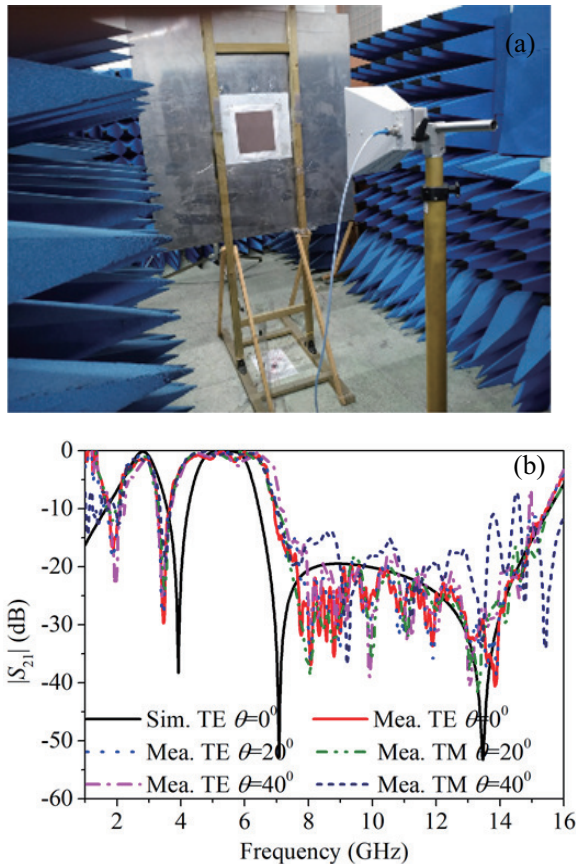


Fig. 10. Performance of the FSS. (a) 3-D FSS cell. (b) Circuit model of the FSS cell. (c) Equivalent circuit of the FSS structure.

high-power microwave (HPM), electronics warfare, and system isolation.

VI. CONCLUSION

In this investigation, recent developments of shielding and shielding effectiveness techniques and methods are reviewed, and analyzed. An example for FSS shielding structure is given, simulated, measured and discussed. From the developments of shielding structures, shielding effectiveness analysis methods, and shielding effectiveness measurements, we think the wide-band shielding structures and shielding effectiveness analysis and measurement with a high power pulse will be an interesting topic for EMP, EMI, and EMC studies. The proposed shielding structures and analysis method can also be used in MIMO engineering systems [39-46] to analyze shielding effectiveness.

ACKNOWLEDGMENT

This work was supported in part by the National Key Research and Development Program of China (2022YFE0123600).

REFERENCES

- [1] Y. Zhao, Y. Li, W. Shi, and W. Yu, "Mutual coupling reduction between patch antenna and microstrip transmission line by using defected isolation wall," *Applied Computational Electromagnetics Society (ACES) Journal*, vol. 34, no. 1, pp. 100-106, 2019.
- [2] V. I. Mordachev, E. V. Sinkevich, D. A. Tsyandenka, A. J. Krachko, Y. V. Yatskevich, A. V. Shuldov, A. A. Vodchits, Y. Li, T. Jiang, and W. Xue, "Multi-variant discrete analysis of EMC of on-board radio equipment with use of worst-case models," *International Symposium on Electromagnetic Compatibility*, Amsterdam, Netherlands, 2018.
- [3] X. Liu, Y. Li, Y. Zhao, and L. Zhao, "Crosstalk reduction design and analysis of the planar meander transmission lines," *International Symposium on Antennas and Propagation*, Busan, South Korea, 2018.
- [4] Y. Zhao, Y. Li, and X. Liu, "A low-profile wideband absorber using capacitive surface," *IEEE International Workshop on Electromagnetics: Applications and Student Innovation Competition (iWEM 2020)*, Penghu, Taiwan, 2020.
- [5] Y. Zhao and Y. Li, "A frequency selective rasorber with two absorption bands," *International Applied Computational Electromagnetics Society (ACES) Symposium*, California, USA, 2020.
- [6] Y. Zhao, Y. Xia, Y. Li, G. Yang, "A frequency selective rasorber with wide transmission band," *International Applied Computational Electromagnetics Society (ACES) Symposium*, Nanjing, China, 2019.
- [7] Y. Zhao, Y. Li, and X. Liu, "A novel dual polarized tunable frequency selective surface with varactors," *IEEE International Symposium on Antennas and Propagation*, Atlanta, Georgia, USA, 2019.
- [8] X. Liu, Y. Li, Y. Zhao, L. Zhao, V. Mordachev, and E. Sinkevich, "Equivalent circuit model of crosstalk reduction parallel transmission lines with defected microstrip structures," *Cross Strait Quad-Regional Radio Science and Wireless Technology Conference*, Xuzhou, China, 2018.
- [9] Y. Zhao, Y. Li, and L. Zhao, "A G-shaped defected isolation wall for mutual coupling reduction between patch antenna and microstrip transmission line," *IEEE 7th Asia-Pacific Conference on Antennas and Propagation*, Auckland, New Zealand, 2018.
- [10] X. Sun, B. Wei, Y. Li, and J. Yang, "A new model for analysis of the shielding effectiveness of multilayer infinite metal meshes in a wide frequency range," *IEEE Transactions on Electromagnetic Compatibility*, vol. 64, no. 1, pp. 102-110, 2022.

- [11] Z. Yan, F. Qin, and J. Cai, "Shielding effectiveness of materials under the excitation of high-power microwave," *IEEE Transactions on Electromagnetic Compatibility*, vol. 62, no. 5, pp. 2317-2320, 2020.
- [12] A. A. Ivnov, M. E. Komnatnov, and T. R. Gazizov, "Analytical model for evaluating shielding effectiveness of an enclosure populated with conducting plates," *IEEE Transactions on Electromagnetic Compatibility*, vol. 62, no. 5, pp. 2307-2010, 2020.
- [13] M. Wang, L. Zhao, J. Wang, X. Liang, S. Zhang, Y. Li, and W. Yu, "A low-profile miniaturized frequency selective surface with insensitive polarization," *Applied Computational Electromagnetics Society (ACES) Journal*, vol. 33, no. 9, pp. 1003-1008, 2018.
- [14] M. J. A. Helvoort and D. W. Harberts, "Low-frequency electromagnetic shielding and scattering of multiple cylindrical shells," *IEEE Transactions on Electromagnetic Compatibility*, vol. 63, no. 1, pp. 46-56, 2021.
- [15] K. Yu, Y. Li, and X. Liu, "Mutual coupling reduction of a MIMO antenna array using 3-D novel meta-material structures," *Applied Computational Electromagnetics Society (ACES) Journal*, vol. 33, no. 7, pp. 758-763, 2018.
- [16] S.-Y. Hyun, K.-W. Lee, and J.-G. Yook, "Modeling of shielding effectiveness of reinforced concrete walls for electromagnetic pulse," *42nd European Microwave Conference*, Amsterdam, The Netherlands, pp. 779-782, 2012.
- [17] A. Lopez, L. Vojtech, and M. Neruda, "Comparison among models to estimate the shielding effectiveness applied to conductive textiles," *Advances in Electrical and Electronic Engineering*, vol. 11, no. 5, pp. 387-391, 2013.
- [18] K. F. Casey, "Electromagnetic shielding behavior of wire-mesh screens," *IEEE Transactions on Electromagnetic Compatibility*, vol. 30, no. 3, pp. 298-306, 1988.
- [19] S. Cristina and A. Orlandi, "An equivalent transmission line model for electromagnetic penetration through reinforced concrete walls," *Transactions on Communications*, vol. E78-B, no. 2, pp. 218-229, 1995.
- [20] M. S. Sarto, "A new model for the FDTD analysis of the shielding performances of thin composite structures," *IEEE Transactions on Electromagnetic Compatibility*, vol. 41, no. 4, pp. 298-306, 1999.
- [21] L. Yan, L. Xu, R. X. K. Gao, J. Zhang, X. Yang, and X. Zhao, "Angularly independent frequency selective surface with good ventilation for millimeter wave EM shielding," *IEEE Transactions on Electromagnetic Compatibility*, vol. 64, no. 1, pp. 251-255, 2022.
- [22] Y. Li, K. Xie, Y. Ying, and Z. Li, "An improved hybrid shielding with LC coil for wireless power transfer system," *IEEE Transactions on Electromagnetic Compatibility*, vol. 64, no.3, pp. 720-731, 2022.
- [23] C. Yang, T. Wendt, M. Stefano, M. Kopf, C. M. Becker, S. Grivet-Talocia, C. Schuster "Analysis and optimization of nonlinear diode grids for shielding of enclosures with apertures," *IEEE Transactions on Electromagnetic Compatibility*, vol. 63, no. 6, pp. 1884-1895, 2021.
- [24] H. H. Park, "Analytic magnetic shielding effectiveness of multiple long slots on a metal plate using rectangular loops," *IEEE Transactions on Electromagnetic Compatibility*, vol. 62, no. 5, pp. 1971-1979, 2020.
- [25] W. Bai, F. Ning, X. Yang, C. Jiao, L. Chen, "Low frequency magnetic shielding effectiveness of a conducting plate with periodic apertures," *IEEE Transactions on Electromagnetic Compatibility*, vol. 63, no. 1, pp. 30-37, 2021.
- [26] Q. F. Liu, W. Y. Yin, J. F. Mao, and Z. Chen, "Accurate characterization of shielding effectiveness of metallic enclosures with thin wires and thin slots," *IEEE Transactions on Electromagnetic Compatibility*, vol. 51, no. 2, pp. 293-300, 2009.
- [27] H. Mai, J. Chen, and A. Zhang, "A hybrid algorithm based on FDTD and HIE-FDTD methods for simulating shielding enclosure," *IEEE Transactions on Electromagnetic Compatibility*, vol. 60, no. 5, pp. 1393-1399, 2018.
- [28] W. P. Carpes, L. Pinchon, and A. Razek, "Analysis of the coupling of an incident wave with a wire inside a cavity using an FEM in frequency and time domains," *IEEE Transactions on Electromagnetic Compatibility*, vol. 44, no. 3, pp. 470-475, 2002.
- [29] S. Benhassine, L. Pinchon, and W. Tabbara, "An efficient finite-element time-domain method for the analysis of the coupling between wave and shielded enclosure," *Transactions on Magnetics*, vol. 38, no. 2, pp. 709-712, 2002.
- [30] F. Haddad, B. Bayard, and B. Sauviac, "Low frequency relation between transfer impedance and shielding effectiveness of braided cables and grid shields," *IEEE Transactions on Electromagnetic Compatibility*, vol. 62, no. 6, pp. 2423-2430, 2020.
- [31] B. Bayard, F. Haddad, and B. Sauviac, "A wide frequency range relationship between transfer impedance of braided cables and shielding effectiveness of corresponding plate shields," *IEEE Transactions on Electromagnetic Compatibility*, vol. 66, no. 6, pp. 1837-1843, 2021.

- [32] E. F. Vance, "Shielding effectiveness of braided wire shields," *IEEE Transactions on Electromagnetic Compatibility*, vol. EMC-17, no. 2, pp. 71-77, 1975.
- [33] W. Luo, Y. Liao, Z. G. Zhao, J. Wang, J. H. HU, H. Xie, J. Y. Zhao, Q. F. Liu, L. Zhou, and W. Y. Yin, "Accurate simulation of shielding effectiveness of metallic cabins using an improved Calderon preconditioner-based time-domain integral equation method," *IEEE Transactions on Electromagnetic Compatibility*, vol. 60, no. 1, pp. 200-208, 2019.
- [34] B. L. Nie, P. A. Du, Y. T. Yu, and Z. Shi, "Study of the shielding properties of enclosures with apertures at higher frequencies using the transmission-line modeling method," *IEEE Transactions on Electromagnetic Compatibility*, vol. 53, no. 1, pp. 73-81, 2011.
- [35] L. Cao, Y. Z. Xie, and M. X. Gao, "Analysis of time-domain shielding effectiveness of enclosures above lossy half-space using an improved half-space FDTD method," *IEEE Transactions on Electromagnetic Compatibility*, vol. 62, no. 5, pp. 2076-2083, 2020.
- [36] G. Wu, P. Chen, L. Xie, and W. Wang, "Analytical correlation between time and frequency domain shielding effectiveness of metallic enclosures with apertures," *IEEE Transactions on Electromagnetic Compatibility*, vol. 62, no. 6, pp. 2773-2784, 2020.
- [37] J. H. Wang, H. H. Park, C. H. Hyoung, and J. H. Kwon, "Shielding effectiveness measurement with wide dynamic range for a small enclosure in a nested reverberation chamber," *IEEE Transactions on Electromagnetic Compatibility*, vol. 63, no. 5, pp. 1407-1416, 2021.
- [38] M. Wang, "Research and design of miniaturized multi-band frequency selective surface," Harbin Engineering University, Master's thesis, 2020.
- [39] W. Shi, X. Liu, and Y. Li, "ULA fitting for MIMO radar," *IEEE Communications Letters*, vol. 26, no. 9, pp. 2190-2194, 2022.
- [40] F. Liu, J. Guo, L. Zhao, G. L. Huang, Y. Li, and Y. Yin, "Ceramic superstrate-based decoupling method for two closely packed antennas with cross-polarization suppression," *IEEE Transactions on Antennas and Propagation*, vol. 69, no. 3, pp. 1751-1756, 2021.
- [41] L. Zhao, F. Liu, X. Shen, G. Jing, Y. Cai, and Y. Li, "A high-pass antenna interference cancellation chip for mutual coupling reduction of antennas in contiguous frequency bands," *IEEE Access*, vol. 6, pp. 38097-38105, 2018.
- [42] J. Li, X. Zhang, Z. Wang, X. Chen, J. Chen, Y. Li, and A. Zhang, "Dual-band eight-antenna array design for MIMO applications in 5G mobile terminals," *IEEE Access*, vol. 7, pp. 71636-71644, 2019.
- [43] K. L. Chung, A. Cui, M. Ma, B. Feng, and Y. Li, "Central-symmetry decoupling technique for circularly-polarized MIMO system of tightly packed Chinese-character-shaped patch antennas," *Applied Computational Electromagnetics Society (ACES) Journal*, vol. 36, no. 9, pp. 1125-1131, 2021.
- [44] T. Jiang, T. Jiao, Y. Li, and W. Yu, "A low mutual coupling MIMO antenna using periodic multi-layered electromagnetic band gap structures," *Applied Computational Electromagnetics Society (ACES) Journal*, vol. 33, no. 3, pp. 305-311, 2018.
- [45] S. Song, Y. Da, B. Qian, X. Huang, X. Chen, Y. Li, and A. A. Kishk, "Dielectric resonator magnetoelectric dipole arrays with low cross polarization, backward radiation, and mutual coupling for MIMO base station applications," *China Communications*, 2022.
- [46] B. Liu, Y. Da, X. Chen, and A. Kishk, "Hybrid decoupling structure based on neutralization and partition schemes for compact large-scale base station arrays," *IEEE Antennas and Wireless Propagation Letters*, vol. 21, no. 2, pp. 267-271, 2022.



Ping Xu obtained his Bachelor of Engineering degree in Telecommunication and Switching Engineering from the Air Force Engineering University in Xi'an, China, in 2003. Subsequently, he earned his Master's degree in Instrument Science and Technology from the National University of Defense Technology in Changsha, China, in 2005. His current research interests encompass a diverse array of topics, such as electromagnetic compatibility, assessment of intricate electromagnetic systems, and the advancement of cutting-edge modeling, simulation, and measurement methodologies.



Tao Jiang obtained his Ph.D. degree from Harbin Engineering University, Harbin, China, in 2002. He joined the College of Information and Communication at Harbin Engineering University as a faculty member in 1994, where he currently holds the position of Professor. Between 2002 and 2003, he served as a Postdoctoral Researcher at the Research Institute of Telecommunication,

Harbin Institute of Technology, Harbin, China. Additionally, he was a Visiting Scholar at the Radar Signal Processing Laboratory, National University of Singapore, from 2003 to 2004. His current research interests encompass radio wave propagation, complex electromagnetic system evaluation, as well as modeling and simulation.

Meiyu Wang obtained her Bachelor of Electrical and Information Engineering from the Harbin Engineering University, 2013. She got her master of Communication and Information System from the Harbin Engineering University, 2012. Her interest is the FSS design.



Yingsong Li received his B.S. degree in Electrical and Information Engineering, and M.S. degree in Electromagnetic Field and Microwave Technology from Harbin Engineering University, 2006 and 2011, respectively. He received his Ph.D degree from

both Kochi University of Technology (KUT), Japan and Harbin Engineering University (HEU), China in 2014. He is currently a Full Professor with the School of Electronic and Information Engineering of Anhui University from March 2022. He was a full Professor in Harbin Engineering University from 2014 to 2022 and a visiting scholar of University of California, Davis from March 2016 to March 2017, a visiting Professor of University of York, UK in 2018, a visiting Professor of Far Eastern Federal University (FEFU) and KUT. Now, he holds the visiting professor position of School of Information of KUT from 2018. He is a Postdoc of Key Laboratory of Microwave Remote Sensing, Chinese Academy of Sciences from 2016 to 2021. Now, He is a Fellow of Applied computational Electromagnetics Society (ACES Fellow), and he is also a senior member of Chinese Institute of Electronics (CIE) and IEEE. He has authored and coauthored about 300 journal and conference papers in various areas of electrical and information engineering. His current research interests include signal processing, adaptive filters, metasurface designs and microwave antennas.

Dr. Li serves as an Area Editor of *AEÜ-International Journal of Electronics and Communications* from 2017 to 2020, and he is an Associate Editor of *IEEE Access*, *Applied Computational Electromagnetics Society Journal (ACES Journal)* and *Alexandria Engineering Journal and Electromagnetic Science*. He is the TPC Co-Chair of the 2019 IEEE International Workshop on Electromagnetics (iWEM 2019-2020), 2019 IEEE 2nd International Conference on Electronic Information

and Communication Technology (ICEICT 2019), 2019 International Applied Computational Electromagnetics Society (ACES) Symposium-China, 2019 Cross Strait Quad-regional Radio Science and Wireless Technology Conference (2019 CSQRWC) and TPC Chair of ICEICT 2021-2022. He is also a General Co-Chair of ICEICT 2020 and a General Chair of IEEE 9th International Conference on Computer Science and Network Technology (ICCSNT 2021) and ICCSNT 2022. He is also a TCP member for many international and domestic conference. He also serves as a Session Chair or Organizer for many international and domestic conferences, including the WCNC, AP-S, ACES-China ect. He acts as a Reviewer of numerous IEEE, IET, Elsevier and other international journals and conferences.



Zhixiang Huang received his BS degree in Statistic and Probability and Ph.D. in Electromagnetic Field and Microwave Technology from Anhui University in 2002 and 2007, respectively. He is a Lecturer of Anhui University from 2007 to 2008 and is promoted to Professor in

2008, and is a visiting scholar in Ames Laboratory, Iowa State University, from 2010 to 2011. Currently, he is a full Professor and the dean of the School of Electronic Information Engineering of Anhui University, founder of Key Laboratory of Electromagnetic Environmental Sensing of Anhui Higher Education Institutes, director of the Young Scientists Club of Chinese Institute of Electronics (CIE), member of the Youth Working Committee of CIE. He is the recipient of the Outstanding Young Talent Project of National Natural Science Foundation of China (NSFC) in 2018 and the Chang Jiang Scholars Program of Ministry of Education of the People's Republic of China in 2022. He is a Senior Member of IEEE. He has more than 100 academic papers in peer-reviewed international/national journals. His current interests include theoretical and computational in electromagnetics and Microwave/RF circuit design, and multiphysics modeling.

Combined Application of Partition Clustering Classification and Gerchberg-Papoulis Optimization Algorithm for Spherical Near Field Antenna Measurements

Fangyun Peng¹, Yuchen Ma², Yuxin Ren², Bo Liu¹, Xiaobo Liu¹, Zhengpeng Wang³,
Lei Zhao⁴, Xiaoming Chen¹, and Zhiqin Wang²

¹School of Information and Communications Engineering
Xi'an Jiaotong University, Xi'an, 710049, China
pfy2014111731@stu.xjtu.edu.cn, liuboright@stu.xjtu.edu.cn, xiaoming.chen@mail.xjtu.edu.cn

²China Academy of Information and Communications Technology
Beijing, 100191, China
mayuchen@caict.ac.cn, renyuxin@caict.ac.cn, wangzhiqin@caict.ac.cn (author for correspondence)

³School of Electronic and Information Engineering
Beihang University, Beijing, 100191, China
wangzp@buaa.edu.cn

⁴School of Information and Control Engineering
China University of Mining and Technology, Xuzhou, 100083, China
leizhao@cumt.edu.cn

Abstract – An adaptive sampling and optimized extrapolation scheme for spherical near-field antenna testing is proposed. The method relies on the partition clustering classification algorithm and Voronoi classification to divide a small amount of initial data into subclasses and cells. The sampling density and rates of variation between adjacent sampling points are used as an overall metric function to evaluate the sampling dynamics at each location. Appropriate interpolation is performed in the highly dynamic region to increase the effective data in the near-field samples. The Gerchberg-Papoulis algorithm extrapolates the unnecessary interpolation region to improve the near-field sampling accuracy. This method uses a small amount of initial near-field sampled data for near-far field conversion to achieve the same precision as uniform oversampling. The feasibility and stability of the algorithm are proved from the actual measurement results.

Index Terms – adaptive sampling, cluster classification algorithm, extrapolation, spherical near-field testing.

I. INTRODUCTION

Compared with plane and cylindrical near-field testing, spherical near field testing (SNFT) scans the entire 3D near-field spherical information of the antenna under

test (AUT) with a uniform sampling interval through a single probe or multiple probes, and can obtain the complete information of the AUT in the entire 3D space. Spherical near-field to far-field (NF-FF) transformation techniques have been widely used to overcome the impossibility or impracticality of measuring antenna radiation patterns in the far field. The core of the SNFT is to use the characteristic that the spherical wave expansion coefficient remains unchanged in the near field (NF) and the far field (FF) to perform the spherical near-far field conversion [1–7]. Recently, the SNFT transformation technique has been applied to loaded/unloaded reverberation chambers for antenna pattern reconstruction [8, 9]. Nevertheless, calculation of spherical wave expansion coefficients for NF data with incomplete or large errors will cause large deviations.

There have been different solutions to the problem of truncation error and to demonstrate the reliability of the method in small truncation regions [10–16]. The authors in [10] proposed an iterative extrapolation-based machine learning algorithm to extend the calculation of the far field to a more accurate region, which employed an analysis of variance test to check the overall feasibility of the regression model. The authors in [11] used the Gerchberg-Papoulis (GP) iterative algorithm to extrapolate the part outside the truncation region. The NF sampling points were extended using a Slepian sequence

that is specially constructed to be orthogonal over a given truncated sweep circle, achieving more accurate results than the classical near-far-field transformation [12]. [13] adopted the truncation error in the measurement of the planar near-field aperture antenna by the alternate orthogonal projection method.

The large number of sampling points results in a long measurement time, which requires more flexibility in the sampling scheme. Measurements on the coarse grid were interpolated onto the finer grid using an optimal sampling interpolation (OSI) method to determine measurements for efficient recovery of non-uniform NF samples [17–18]. The compressed sensing (CS) method determines the minimum number of samples for near-field sparse recovery, which allows reducing the number of measurements for all antennas while maintaining accuracy [19–20]. However, the sparse level of NF sampled data and the prior information of the system had a great impact on the test results and are not suitable for all antenna tests. Based on measurements with helical scans, the authors in [21] investigated the application of non-uniform fast Fourier transforms in SNFT. A recently proposed method based on recursive partitioning in a multi-level subdomain hierarchy of radiating surfaces is applied to arbitrary surface measurements [22]. The authors in [23–25] described the adaptive method to reduce the measurement burden spherical near-field measurements. The fast irregular antenna field transformation algorithm (FIAFTA) was used to post-process the near field collected on an irregular grid [26] and the source reconstruction method was used to calculate the equivalent current on the surface of the ellipsoid containing the AUT [23]. These techniques require more time than fast Fourier near-far field transform methods.

In this paper, a spherical near-field sampling optimization method based on partition clustering classification and GP joint optimization is proposed. Starting from a small amount of sampled data, the clustering method is used to quantify the dynamic changes of the AUT NF electric field. There is a trade-off between sampling density and variation between adjacent sampling points according to different criteria. The new data is interpolated in the high dynamic change area of the field to improve the accuracy of the near-field sampling data and the GP iterative algorithm extrapolates the data to the unnecessary interpolation area to reduce the truncation error.

The structure of the paper is as follows. Section II introduces the theory of spherical wave expansion and the optimization scheme of spherical near-field sampling. Measurement results are presented in section III. The superiority of the optimized scheme in improving the test efficiency is proved. Section IV concludes the paper.

II. BACKGROUND THEORY

This section presents the theory of antenna pattern reconstruction based on a small number of initial sampling points. Firstly, the theory of spherical wave expansion is described. Then, the clustering method is introduced to divide the initial sampling points into several subclasses, and the calculation process of introducing new sampling data by using the GP optimization algorithm is given. Finally, the near-field data is reconstructed to obtain the antenna pattern. The detailed measurement process is as follows.

According to the uniqueness theorem and the equivalence principle, the radiation field in the outer space of the closed surface can be calculated and determined through the tangential component of the electromagnetic field on the closed surface including all the radiation sources. In the SNFT, an equivalent spherical surface is used to completely surround the AUT, and a passive region is established outside the spherical surface, as shown in Fig. 1.

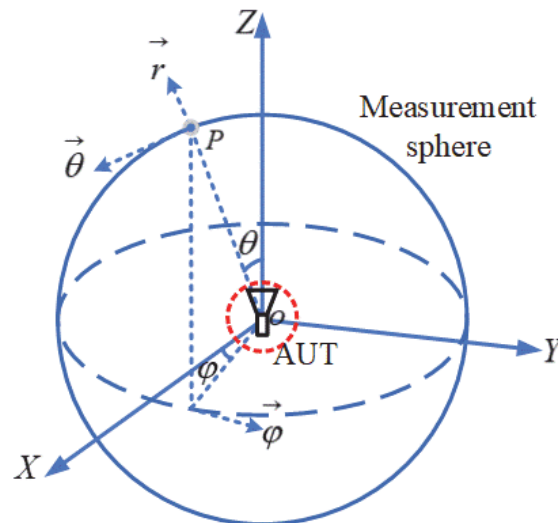


Fig. 1. Schematic of SNFT.

Outside the minimum sphere of the AUT, the electric field can expand as a weighted sum of spherical wave functions expressed as:

$$E(r, \theta, \varphi) = \sum_{s=1}^2 \sum_{n=1}^N \sum_{m=-n}^n Q_{smn} \vec{F}_{smn}^{(3)}(r, \theta, \varphi), \quad (1)$$

where (r, θ, φ) are the spherical coordinates, Q_{smn} are the SWCs of the AUT, $\vec{F}_{smn}^{(3)}$ are the spherical wave expansion functions, $s = 1$ and 2 represent transverse electric (TE) and transverse magnetic (TM) wave modes, respectively, and m, n are the number of modes of AUT. N is a truncation number for the spherical wave expansion empirically obtained from $N = [kr_0] + 10$,

where k is the wave number, r_0 is the radius of the minimum sphere surrounding the antenna and the square brackets indicate the largest integer smaller than or equal to kr_0 . In equation (1), the spherical wave expansion functions are known, the SWCs Q_{smn} can be solved and the field value at any distance can be obtained.

In order to obtain the dynamic change of the electric field data in the near field of the antenna, $M_{initial}$ sampling data are randomly selected from the uniform spherical near field sampling dataset S_2 as the initial samples set as S_1 . The K-means clustering method is used to cluster the $M_{initial}$ sampled data into k subclasses, and each subclass randomly selects a sample as the cluster center. Minkowski distance ($p = 2$ means Euclidean distance) is used to measure the deviation of each sample value from the cluster center and each sample is classified into the subclass where the cluster center with the closest distance is located. The cluster center of each subclass is updated to the average value of all points in the subclass, and the samples are reclassified until the cluster center of all subclasses no longer changes or the total clustering error in all subclasses is the smallest. The current total clustering error in all subclasses is:

$$d = \left(\sum_{j=1}^k \sum_{x_i \in C_j, c_j \in C_j} |x_i - c_j|^p \right)^{\frac{1}{p}}, \quad (2)$$

where x_i is the i -th sample and c_j is the cluster center belonging to the j -th subclass C_j .

After obtaining the cluster classification results, the initial near-field sampling data is sorted according to the sample sampling density and the rate of variation of adjacent samples, and the top ranking represents the area that needs to be interpolated. In order to calculate the sampling density, the initial sampling points are represented by a Voronoi diagram according to the nearest neighbor principle [27]. Each initial sampling point corresponds to a cell, and the sampling density is determined by the area of each cell. Each sampling point is associated with its nearest neighbor cell, and the sample variation rate is expressed as the gradient of the field between adjacent sampling points. So the overall evaluation parameter can be expressed as:

$$G(x_m) = \alpha \left(1 + \frac{S(x_m)}{\sum_{p=1}^{M_{initial}} S(x_p)} \right) + \beta \left(1 + \frac{V(x_m)}{\sum_{p=1}^{M_{initial}} V(x_p)} \right), \quad (3)$$

where $S(x_m)$ is the area of the m th cell, $V(x_m)$ is the sum of the absolute values of all gradients around the m th cell and α, β (satisfying $\alpha + \beta = 1$) are the weighting coefficients. α and β are adjusted accordingly according to the cluster classification results. If the sampling variation rate in a subclass is too large, in order to better judge the interpolation requirements of the sampling area, it is necessary to increase the proportion of sampling density

in the overall evaluation parameters, that is, increase the value of α .

According to the judgment criteria, part of the data to be interpolated comes from the dataset S_2 , and a small amount of data that is not located in the dataset S_2 with uniform sampling interval. A modified Akima piecewise cubic Hermite interpolation method is used in this part.

In order to reduce the truncation error caused by the near-far field conversion after zero-filling the non-essential interpolation area with smooth dynamic changes, the GP algorithm is introduced to extrapolate the sampled values. It is a band-limited extrapolation algorithm that extrapolates the data outside the interval from the known interval, and it is iteratively implemented by using Fourier transform and inverse Fourier transform. Plane wave spectra (PWS) of spherical near-field probe sampled data is obtained from truncated NF measurements using Fourier transforms:

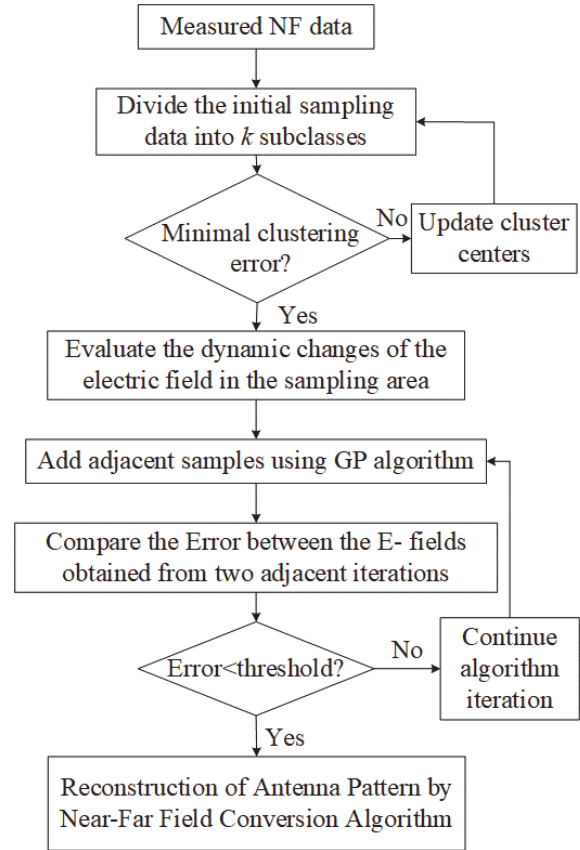


Fig. 2. Schematic diagram of the proposed method.

$$G_0(\theta_k, \varphi_k) = fft[g_0(\theta_k, \varphi_k)], \quad (4)$$

where $g_0(\theta_k, \varphi_k)$ is the cluster-interpolated accessible near field data. The filter functions in the spectral and space domain are:

$$H_R(\theta_k, \varphi_k) = \begin{cases} 1, & (\theta_k, \varphi_k) \in \Omega_0 \\ 0, & (\theta_k, \varphi_k) \notin \Omega_0 \end{cases}, \quad (5)$$

and

$$h(\theta_k, \varphi_k) = \begin{cases} 1, & (\theta_k, \varphi_k) \in \omega_0 \\ 0, & (\theta_k, \varphi_k) \notin \omega_0 \end{cases}, \quad (6)$$

where ω_0 and Ω_0 are reliable regions of the space and spectrum. The electric field on the sampling surface obtained by extrapolation is given by the following equation:

$$\begin{aligned} \xi_{n+1}(\theta_k, \varphi_k) &= \hat{\xi}_n(\theta_k, \varphi_k) + (g_0(\theta_k, \varphi_k) \\ &\quad - \hat{\xi}_n(\theta_k, \varphi_k))h(\theta_k, \varphi_k), \end{aligned} \quad (7)$$

where

$$\hat{\xi}_{n+1}(\theta_k, \varphi_k) = \text{ifft}[H_R(\theta_k, \varphi_k)G_n(\theta_k, \varphi_k)]. \quad (8)$$

The PWS of the reliable region is:

$$G_n(\theta_k, \varphi_k) = \text{fft}[g_n(\theta_k, \varphi_k)], \quad (9)$$

where fft and ifft means Fourier transform and inverse Fourier transform, n is the value of iteration times, (θ_k, φ_k) is the k th sampling point on the spherical grid and $g_n(\theta_k, \varphi_k)$ is the optimization extrapolation result for the n th iteration. The error of the near-field data obtained from two adjacent iterations is expressed as

$$\text{Error} = \sum_{k=1}^{M_{\text{total}}} |g_{n+1}(\theta_k, \varphi_k) - g_n(\theta_k, \varphi_k)|^2, \quad (10)$$

where M_{total} is the total effective NF data after extrapolation. After several iterations, the error reaches a stable convergence point and the iteration terminates.

A schematic diagram of the proposed method is shown in Fig. 2, where a small amount of sampling data is used to verify the effectiveness of the clustering technique and the GP extrapolation algorithm to estimate the electric field in the extended area.

III. MEASUREMENT RESULTS

A commercial antenna operating at 2.6 GHz, which is invisible internally, was tested in the spherical near-field multi-probe anechoic chamber of the China Academy of Information and Communications Technology (CAICT). The radius of the SNFT system is 1.6 m, and the minimum spherical radius surrounding the antenna is 0.156 m, as shown in Fig. 3. Figure 4 shows the antenna pattern obtained by using commercial software to calculate the NF data, which is set as the reference radiation pattern.

In order to obtain the initial small amount of sampling data, the NF sampling interval is set to 15 degrees and there is a truncation in the range from $\theta = 165^\circ$ to $\theta = 180^\circ$ degrees due to the influence of the south pole. To improve the test accuracy, triple uniform oversampling ($\Delta\theta = \Delta\varphi = 5^\circ$) is necessary. The uniformly sampled dataset and triple oversampled dataset are set as S_1 and S_0 respectively, and 150 sampling points are selected from S_1 as the initial data set S_2 .

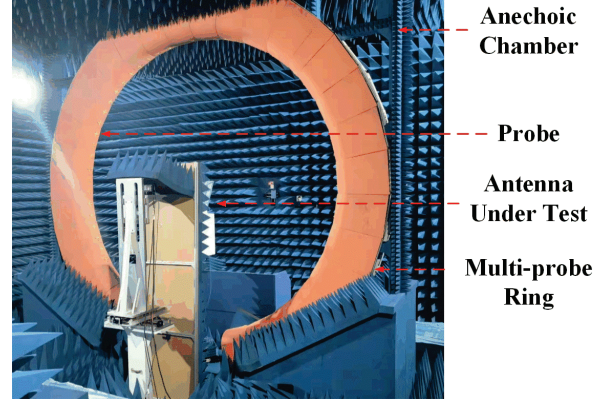


Fig. 3. The spherical NF measurement environment.

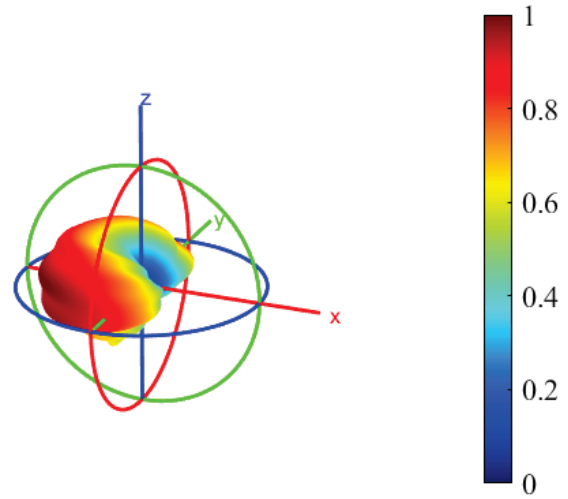


Fig. 4. Reference radiation pattern at 2.6 GHz.

The K-means clustering method divides the sampled values into k subclasses, and for each k value, the sum of the squared distances from every sample to the nearest cluster center is calculated as the total clustering error. As shown in Fig. 5 (a), the total cluster error converges to a stable value at $k = 6$ and Fig. 5 (b) shows the cluster classification results for $k = 6$. Figure 6 shows the Voronoi diagram cell classification results for the initial sampling of the NF. Using equation (3), the area of each cell and the variation rate of adjacent sampling points are calculated. The cell groups whose base sites are red represent highly dynamic areas requiring interpolation, and blue areas represent unnecessary interpolation region.

We use the interpolation method mentioned in the previous section to obtain the dataset S_3 with truncated regions. Dataset S_4 is extrapolated from dataset S_3 by GP algorithm. Figure 7 (a) shows the error of two adjacent iterations of the co-polarization (CP) and

cross-polarization (XP) of the antenna. When the GP algorithm iterates 80 times, the error converges. Figure 7 (b) shows the normalized iterative error of the oversampled electric field and the electric field obtained by the proposed method.

Figure 8 (a) shows the radiation pattern reconstructed from the dataset S_4 . Figure 8 (b) shows the rel-

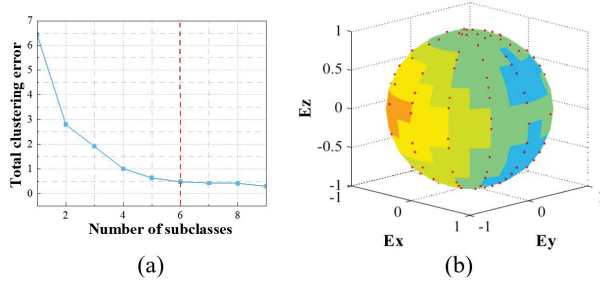


Fig. 5. K-means clustering method. (a) L-curve. (b) Clustering method, $k = 6$.

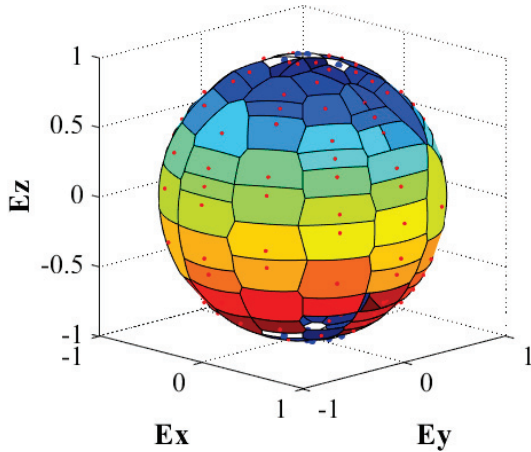


Fig. 6. Voronoi diagram classification for near-field sampling.

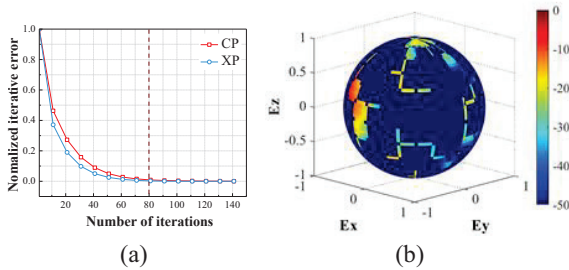


Fig. 7. (a) The normalized iterative error of CP and XP components obtained from two adjacent iterations. (b) Relative error of S_4 and S_0 in all angles.

ative error of reference and reconstructed radiation pattern. The relative error can be obtained using:

$$\text{Relative Error} = 20 \log \left| \frac{|E_1| - |E_2|}{|E_1| + |E_2|} \right|, \quad (11)$$

where E_1 and E_2 are the two electric fields to be compared, respectively. Comparisons of CP and XP components in XOY plane and XOZ plane between reference pattern, the pattern reconstructed by triple oversampling and optimal sampling by the proposed algorithm are given in Fig. 9. As can be seen, the main lobe of

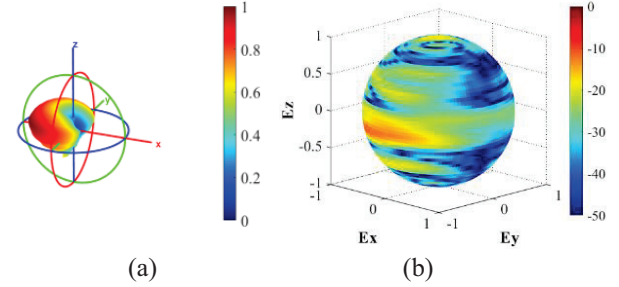


Fig. 8. (a) Reconstructed radiation pattern. (b) Relative error of reference and reconstructed radiation pattern in all angles.

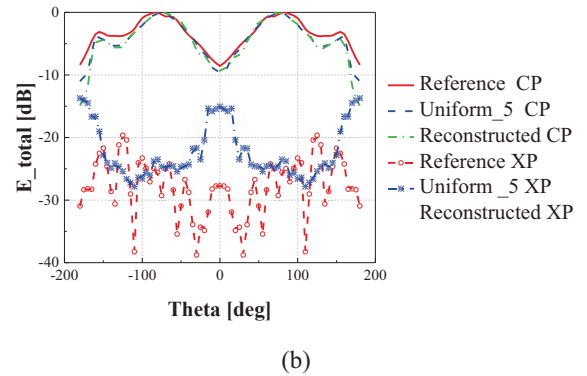
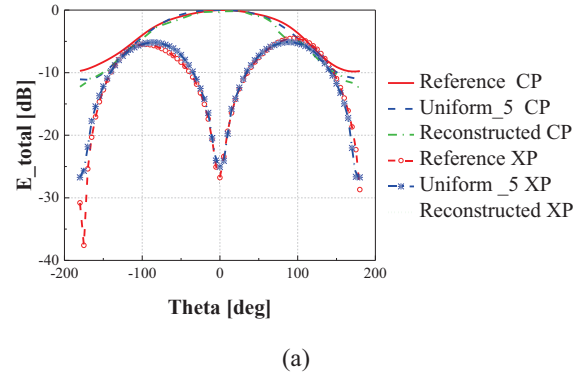
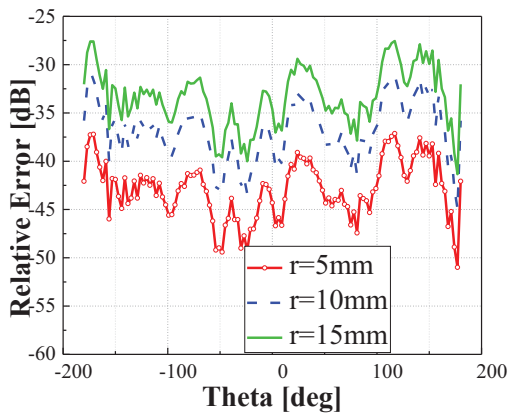


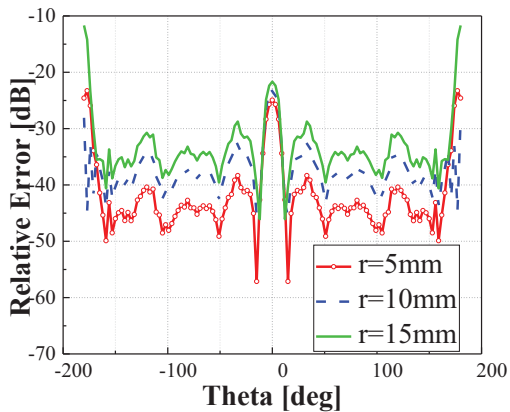
Fig. 9. Comparisons of CP and XP components in (a) XOY plane, and (b) XOZ plane between reference pattern, pattern reconstructed by triple oversampling and optimal sampling by the proposed algorithm.

the CP component of the pattern is in good agreement, but the reconstruction result of the XP has a large error compared with the reference pattern, especially in XOZ plane.

It is noted that the possible positioning error in the actual test affects the pattern recovery. Figures 10 and 11 show the interference errors in XOY plane and XOZ plane introduced when the radial errors are 5 mm, 10 mm and 15 mm, respectively, and the θ angle errors are 0.01 deg, 0.5 deg and 1 deg, respectively. The radial position error in spherical NF scanning mainly affects the phase error in the near field, which is proportional to the radial error. The θ angle error between the actual and the ideal alignment direction of the AUT makes the maximum gain direction of the probe antenna deviate from the center of the SNFT system, which changes the test distance and causes the change of the probe receiving strength to affect the recovery of the pattern.

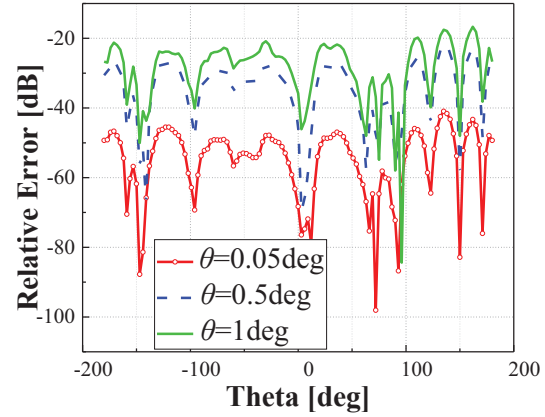


(a)

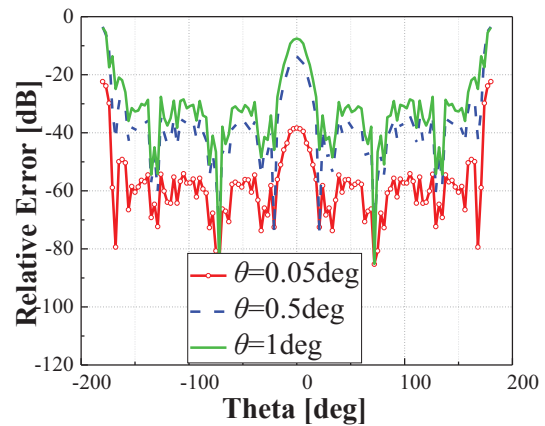


(b)

Fig. 10. The relative errors in (a) XOY plane, and (b) XOZ plane introduced when the radial errors are 5 mm, 10 mm, and 15 mm, respectively.



(a)



(b)

Fig. 11. The relative errors in (a) XOY plane, (b) XOZ plane introduced when the θ angle errors are 0.01 deg, 0.5 deg, and 1 deg, respectively.

IV. CONCLUSION

This paper proposes a method to improve the sampling efficiency of spherical near-field testing. Starting from a small number of near-field sampling points, the region with high dynamic variation of the electric field is located through the clustering classification theory for appropriate interpolation. The GP algorithm is used to extrapolate the unnecessary interpolation area to further improve the sampling accuracy and reduce the truncation error. The multi-probe spherical near-field anechoic chamber test was carried out on a commercial antenna working at 2.6 GHz. The feasibility of this scheme is demonstrated by comparing the reference radiation pattern with the radiation pattern reconstructed by three oversampling and optimized samplings. The influence of the test positioning error on the reconstructed pattern is further discussed.

REFERENCES

- [1] J. E. Hansen, *Spherical Near-Field Antenna Measurements*, Peter Peregrinus, London, UK, 1988.
- [2] T. M. Gemmer and D. Heberling, "Accurate and efficient computation of antenna measurements via spherical wave expansion," *IEEE Trans. Antennas Propag.*, vol. 68, no. 12, pp. 8266-8269, Dec. 2020.
- [3] T. B. Hansen, "Spherical near-field scanning with higher-order probes," *IEEE Trans. Antennas Propag.*, vol. 59, no. 11, pp. 4049-4059, Nov. 2011.
- [4] T. Laitinen, S. Pivnenko, J. M. Nielsen, and O. Breinbjerg, "Theory and practice of the FFT/matrix inversion technique for probe-corrected spherical near-field antenna measurements with high-order probes," *IEEE Trans. Antennas Propag.*, vol. 58, no. 8, pp. 2623-2631, Aug. 2010.
- [5] R. Cornelius and D. Heberling, "Spherical near-field scanning with pointwise probe correction," *IEEE Trans. Antennas Propag.*, vol. 65, no. 2, pp. 995-997, Feb. 2017.
- [6] L. Zhiping, Z. Wang, and W. Jianhua, "Computer reconstructed holographic technique for phase-less near-field measurement," *Applied Computational Electromagnetics Society (ACES) Journal*, vol. 28, no. 12, pp. 1199-1204, Sep. 2021.
- [7] F. S. de Adana, O. Gutiérrez, L. Lozano, and M. Cátedra, "A new iterative method to compute the higher order contributions to the scattered field by complex structures," *Applied Computational Electromagnetics Society (ACES) Journal*, vol. 21, no. 2, pp. 115-126, Jun. 2022.
- [8] J. Zheng, X. Chen, X. Liu, M. Zhang, B. Liu, and Y. Huang, "An improved method for reconstructing antenna radiation pattern in a loaded reverberation chamber," *IEEE Trans. Instrum. Meas.*, vol. 71, Art. no. 8001812, 2022.
- [9] Q. Xu, Y. Huang, L. Xing, C. Song, Z. Tian, S. S. Alja'afreh, and M. Stanley, "3-D antenna radiation pattern reconstruction in a reverberation chamber using spherical wave decomposition," *IEEE Trans. Antennas Propag.*, vol. 65, no. 4, pp. 1728-1739, Apr. 2017.
- [10] R. R. Alavi and R. Mirzavand, "Range extension in partial spherical near-field measurement using machine learning algorithm," *IEEE Antennas Wireless Propag. Lett.*, vol. 19, no. 11, pp. 2003-2007, Nov. 2020.
- [11] X. Li, T. Zhang, M. Wei, and L. Yang, "Reduction of truncation errors in planar near-field antenna measurements using improved Gerchberg-Papoulis algorithm," *IEEE Trans. Instrum. Meas.*, vol. 69, no. 9, pp. 5972-5974, Sept. 2020.
- [12] K. T. Kim, "Truncation-error reduction in spherical near-field scanning using Slepian sequences: Formulation for scalar waves," *IEEE Trans. Antennas Propag.*, vol. 59, no. 8, pp. 2813-2823, Aug. 2011.
- [13] F. J. Cano-Facila, S. Pivnenko, and M. Sierra-Castañer, "Reduction of truncation errors in planar, cylindrical, and partial spherical near-field antenna measurements," *Int. J. Antennas Propag.*, pp. 186-187, 2012.
- [14] O. M. Bucci and M. D. Migliore, "A new method for avoiding the truncation error on near-field antenna measurements," *IEEE Trans. Antenna Propag.*, vol. 54, no. 10, pp. 2940-2952, Oct. 2006.
- [15] E. Martini, O. Breinbjerg, and S. Maci, "Reduction of truncation errors in planar near-field aperture antenna measurements using the Gerchberg-Papoulis algorithm," *IEEE Trans. Antenna Propag.*, vol. 56, no. 11, pp. 3485-3493, Nov. 2008.
- [16] O. M. Bucci and M. D. Migliore, "A new method for avoiding the truncation error on near-field antenna measurements," *IEEE Trans. Antenna Propag.*, vol. 54, no. 10, pp. 2940-2952, Oct. 2006.
- [17] F. D'Agostino, F. Ferrara, C. Gennarelli, G. Gennarelli, R. Guerriero, and M. Migliozzi, "On the direct non-redundant near-field-to-far-field transformation in a cylindrical scanning geometry," *IEEE Antennas Propag. Mag.*, vol. 54, no. 1, pp. 130-138, Feb. 2012.
- [18] F. D'Agostino, F. Ferrara, C. Gennarelli, R. Guerriero, and M. Migliozzi, "Non-redundant spherical NF-FF transformations using ellipsoidal antenna modeling: Experimental assessments [measurements corner]," *IEEE Antennas Propag. Mag.*, vol. 55, no. 4, pp. 166-175, Aug. 2013.
- [19] B. Hofmann, O. Neitz, and T. F. Eibert, "On the minimum number of samples for sparse recovery in spherical antenna near-field measurements," *IEEE Trans. Antennas Propag.*, vol. 67, no. 12, pp. 7597-7610, Dec. 2019.
- [20] C. Culotta-López and D. Heberling, "Adaptive sampling for compressed spherical near-field measurements," *Antenna Measurement Techniques Association Symposium (AMTA)*, Newport, RI, pp. 1-6, 2020.
- [21] F. R. Varela, B. G. Iragüen, and M. Sierra-Castañer, "Application of nonuniform FFT to spherical near-field antenna measurements," *IEEE Trans. Antennas Propag.*, vol. 68, no. 11, pp. 7571-7579, Nov. 2020.
- [22] F. R. Varela, B. G. Iragüen, and M. Sierra-Castañer, "Near-field to far-field transformation on arbitrary surfaces via multi-level spherical wave expansion," *IEEE Trans. Antennas Propag.*, vol. 68, no. 1, pp. 500-508, Jan. 2020.
- [23] R. R. Alavi, R. Mirzavand, J. Doucette, and P. Mousavi, "An adaptive data acquisition and clus-

tering technique to enhance the speed of spherical near-field antenna measurements,” *IEEE Antennas Wireless Propag. Lett.*, vol. 18, no. 11, pp. 2325-2329, Nov. 2019.

- [24] Y. Wang, T. F. Eibert, and Z. Nie, “Adaptive cross approximation algorithm accelerated inverse equivalent current method for near-field antenna measurement,” *IEEE Trans. Antennas Propag.*, vol. 67, no. 3, pp. 1874-1883, Mar. 2019.
- [25] R. R. Alavi, R. Mirzavand, and P. Mousavi, “Fast and accurate near-field to far-field transformation using an adaptive sampling algorithm and machine learning,” *IEEE International Symposium on Antennas and Propagation and USNC-URSI Radio Science Meeting*, Atlanta, GA, pp. 225-226, 2019.
- [26] T. F. Eibert, E. Kılıç, C. Lopez, R. A. Mauermayer, O. Neitz, and G. Schnattinger, “Electromagnetic field transformations for measurements and simulations (invited paper),” *Prog. Electromagn. Res.*, vol. 151, pp. 127-150, May 2015.
- [27] J. Zheng, X. Chen, and Y. Huang, “An effective antenna pattern reconstruction method for planar near-field measurement system,” *IEEE Trans. Instrum. Meas.*, vol. 71, Art. no. 8005012, Jul. 2022.



Fangyun Peng received her B.Sc. degree in Electrical Information Engineering from Southwest Jiaotong University, Chengdu, China, in 2018. She is currently pursuing a Ph.D. degree at the School of Electronic and Information Engineering from Xi’an Jiaotong University. Her research interests include over-the-air testing.



Yuchen Ma was born in Beijing, China, in 1993. He received his B.E. degree and doctorate from the School of Electronic and Information Engineering, Beijing Jiaotong University, Beijing, China, in 2015 and 2021, respectively. He is currently at the China Academy of Information and Communications Technology, Beijing, China. His current research interests include near-field measurement and antenna design.



Yuxin Ren received his M.Sc. degree in Electronic Science and Technology from the Beijing University of Posts and Telecommunications, Beijing, in 2014. Since 2018, he has been an engineer at the China Academy of Information and Communications and Technology. His current research interests include the theory of reverberation chambers, plane wave synthesizers, and other OTA test systems.

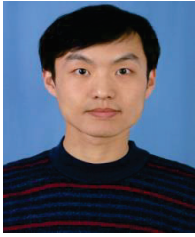


Bo Liu received his B.Sc. degree in Electronic Information Engineering from Xidian University, Xi’an, China, in 2019. He received his M.Sc. degree from the School of Electronic and Information Engineering, Xi’an Jiaotong University, Xi’an, China, in 2022. His research interests include MIMO antennas and the decoupling of MIMO antennas.



Xiaobo Liu (Member, IEEE) was born in Baoji, China, in 1992. He received his B.Eng. degree in Information Engineering and his Ph.D. degree in Electronic Science and Technology from Xi’an Jiaotong University, Xi’an, China, in 2014 and 2018, respectively. From 2018 to 2020, he was a Research Associate with Xi’an Jiaotong University. Since 2020, he has been a Post-Doctoral Fellow in Applied Mathematics and an Assistant Professor with Xi’an Jiaotong University. He has authored or coauthored more than 20 articles in international and domestic journals and conferences. His research interests include electromagnetic and microwave theory, computational electromagnetics, metasurface, antenna design, and microwave circuit.

Dr. Liu serves as a reviewer for the following IEEE journals: *IEEE Transactions on Microwave Theory and Techniques* (TMTT), the *IEEE Microwave and Wireless Components Letters* (MWCL), and the *IEEE Antennas and Wireless Propagation Letters* (AWPL).



Zhengpeng Wang (M'15) was born in Shandong, China, in 1981. He received his B.Sc. degree in Electronic Science and Technology from Shandong University, Jinan, China, in 2004, and his M.Sc. and Ph.D. degrees in Electromagnetic Field and Microwave Technology from Beihang University, Beijing, China, in 2007 and 2012, respectively.

He was a Visiting Researcher with the Antenna and Applied Electromagnetic Laboratory, University of Birmingham, Birmingham, U.K., in 2009 and 2010. From 2013 to 2015, he was a Research Fellow with the University of Kent, Canterbury, U.K., and the University of Science and Technology Beijing, Beijing, China. He is currently an Associate Professor at Beihang University. His current research interests include over-the-air (OTA) testing, reconfigurable antennas, compact antenna test range feed antenna and antenna measurement.



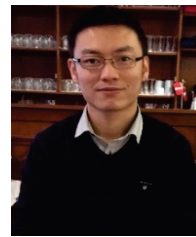
Lei Zhao (Senior Member, IEEE), received his B.S. degree in Mathematics from Jiangsu Normal University, China, in 1997. He received his M.S. degree in Computational Mathematics and Ph.D. degree in Electromagnetic Fields and Microwave Technology, both from Southeast

University, Nanjing, China, in 2004 and 2007, respectively.

He joined the China University of Mining and Technology, Xuzhou, China, in 2019, where he is currently a Full Professor. From September 2009 to December 2018, he worked at Jiangsu Normal University, Xuzhou, China. From August 2007 to August 2009, he worked at the Department of Electronic Engineering, The Chinese University of Hong Kong, as a Research Associate. From February 2011 to April 2011, he worked at the Department of Electrical and Computer Engineering, National University of Singapore, as a Research Fellow. From September 2016 to September 2017, he worked at the Department of Electrical and Computer Engineering, University of Illinois at Urbana-Champaign, Champaign, IL, USA, as a Visiting Scholar. He has authored or coauthored more than 90 refereed journal and conference papers. His current research interests include spoof surface plasmon polaritons theory and its applications, RF/microwave antenna and filter design, computational electromagnetics, and electromagnetic radiation on the human body.

Dr. Zhao serves as an Associate Editor for *IEEE Access*, an Associate Editor-in-Chief and reviewer for

the *Applied Computational Electromagnetics Society (ACES) Journal* and is a reviewer for multiple journals and conferences including *IEEE Trans. on Microwave Theory and Techniques*, *IEEE Trans. Antennas and Propagation*, *IEEE Antennas and Wireless Propagation Letters*, and other primary electromagnetics and microwave-related journals.



Xiaoming Chen received his B.Sc. degree in Electrical Engineering from Northwestern Polytechnical University, Xi'an, China, in 2006, and M.Sc. and Ph.D. degrees in Electrical Engineering from Chalmers University of Technology, Gothenburg, Sweden, in 2007 and

2012, respectively. From 2013 to 2014, he was a post-doctoral researcher at that same university. From 2014 to 2017, he was with Qamcom Research & Technology AB, Gothenburg, Sweden. Since 2017, he has been a professor at Xi'an Jiaotong University, Xi'an, China. His research areas include MIMO antennas, over-the-air testing and reverberation chambers, and has published more than 150 journal articles on these topics.

Prof. Chen currently serves as a Senior Associate Editor for *IEEE Antennas and Wireless Propagation Letters*. He was the general chair of the *IEEE International Conference on Electronic Information and Communication Technology (ICEICT)* in 2021. He won first prize for the universities' scientific research results in Shaanxi province, China, 2022. He received the IEEE outstanding Associate Editor awards in 2018, 2019, 2020, 2021, and the URSI (International Union of Radio Science) Young Scientist Award in 2017 and 2018.



Zhiqin Wang is the vice president of the China Academy of Information and Communications Technology. She is the chair of the CCSA Wireless Technical Committee. She is dedicated to pioneering research and practice in the field of mobile communications, and has specialized in mobile communications' technical research and standards. She is the chair of IMT-2020 (5G) Promotion Group in China and the vice chief engineer of the major project "New Generation Broadband Wireless Mobile Telecommunications".

A Compact Four-way Quadrature Power Splitter for 5G Low-band Applications

Song Gao¹, Hao Wang¹, Kwok L. Chung^{2,*}, Yingsong Li³, Kangtai Zheng², and Luqi Chen²

¹Civionics Research Laboratory, School of Civil Engineering
Qingdao University of Technology, Qingdao, 266000, China
gaosong@qut.edu.cn, hason1997@163.com

²School of Computer Science and Engineering
Huizhou University, Huizhou, 516007, China
*klchung@hzu.edu.cn, 2014080902233@stu.hzu.edu.cn, 2014080902429@stu.hzu.edu.cn

³Key Laboratory of Intelligent Computing and Signal Processing
Ministry of Education, Anhui University, China
liyingsong@ieee.org

Abstract – This article introduces an ultra-compact four-way quadrature power splitter (4W-QPS) based on a novel transmission-line compression technique called double-path zigzag microstrip line (DP-ZML). Detailed design techniques with modular approach are disclosed for the state-of-the-art 5G low-band applications. The theoretical predictions are verified with experimental results through a fabricated prototype that operates from 696.55 to 876.03 MHz with >15 dB return-losses and isolations, and $90^\circ \pm 4^\circ$ quadrature phase between adjacent outputs. The compact size of this 4W-QPS is achieved at $0.21\lambda_g \times 0.21\lambda_g$ at a center frequency of 786 MHz.

Index Terms – 5G low-band, miniaturization, quadrature power splitter (QPS), Z-shaped microstrip line.

I. INTRODUCTION

According to 3GPP TS38.101-1 V15.3.0 [1], New Radio Frequency Ranges (NR-FRs) are being rolled out into fifth generation (5G) mobile communications, where power dividers/splitters play a vital role in 5G low frequency bands. The 5G low-band spectrum is classified as any spectrum that operates below 1 GHz, e.g., 700~800 MHz, like n12, n14, n18, and n20 [1]. A four-way quadrature power splitter (4W-QPS) with constant phase-shifts is in high demand by circularly-polarized antennas, multiple-beam antennas and power amplifiers due to its simplicity and low power loss. On one hand, conventional power dividers are known to occupy a large physical size due to restriction of multiple quarter-wavelength ($\lambda/4$) transmission lines. On the other hand, a large foot-print is required for the QPSs operating

in the 5G low-band NR at frequencies of 800 MHz or so.

Over the years, many miniaturization techniques of power splitter circuits and or feeding networks using various types of transmission lines have been reported in the literature [2–5]. In [4–5], broadband QPSs using metamaterial lines were proposed for circularly-polarized antenna array, wherein the quadrature (90°) phase difference between output ports was realized by space-saving metamaterial lines. Based on half-wavelength slot-lines coupling, a compact four-way out-of-phase power splitter was proposed in [6]. However, the isolations between output ports are identified to be insufficient (<15 dB), which may not be suitable for certain applications that require high isolations. To address this issue, a new radial power divider was reported in [7], wherein an isolation network composed of RLC and LC topologies was used. Very good isolation levels (>20 dB) and its associated bandwidth were obtained; however, the air bridges used will increase fabrication cost as its footprint is big ($80 \times 80 \text{ mm}^2$) at 1 GHz. In [8], a four-way microstrip power splitter using lumped elements was proposed for dual-band (1 and 2 GHz) application. However, its electrical size ($0.54\lambda_g \times 0.45\lambda_g$) is found to be large. Recently, an interesting chained slotted power divider using half-mode substrate-integrated waveguide at X-band was presented [9], where compact size can be achieved at the cost of low isolation levels of about 12 dB. More recently, a very compact ($0.17\lambda_g \times 0.22\lambda_g$) quasi-planar four-way power splitter was reported [10], wherein high isolation (20 dB) bandwidth of 58% was achieved but with equal phases at its output ports. Similarly, a wideband (60%) equal-phase power

splitter (EPS) using multi-stage connection lines was reported in [11]. However, both the extra loss and broad size are found to be large.

In this paper, a highly compact four-way power splitter with quadrature phases using double-path Z-shaped microstrip line (DP-ZML) in the form of a double layer is presented. The goal of this compact design is to enable 5G low-band operation at a low cost. The predicted results are validated by a fabricated prototype presenting an operating bandwidth from 696.55 to 876.03 MHz, where its return losses and isolation are of >15 dB with phase-difference of $90^\circ \pm 4^\circ$ between adjacent output ports. The ultra-compact size is achieved at $0.21\lambda_g \times 0.21\lambda_g$.

II. GEOMETRY OF POWER SPLITTER USING DOUBLE-PATH ZIGZAG MICROSTRIP LINES

The initial geometry of the proposed double-path zigzag microstrip line in the form of four sections of ZML is shown in Fig. 1, which mimics a phase delay of 90° as in the single straight ML case (Fig. 1 (a)). The DP-ZML makes full use of PCB area and a common ground plane, wherein the ZMLs (zigzag traces) are positioned anti-symmetrically at the top- and bottom-side of the dual-layer FR4 substrate and electrically connected through three copper vias as shown in Figs. 1 (b) and 1 (c). In this way, the required length (phase delay) can be generated with an extremely small footprint on the circuit board. Meanwhile, owing to the short lines of

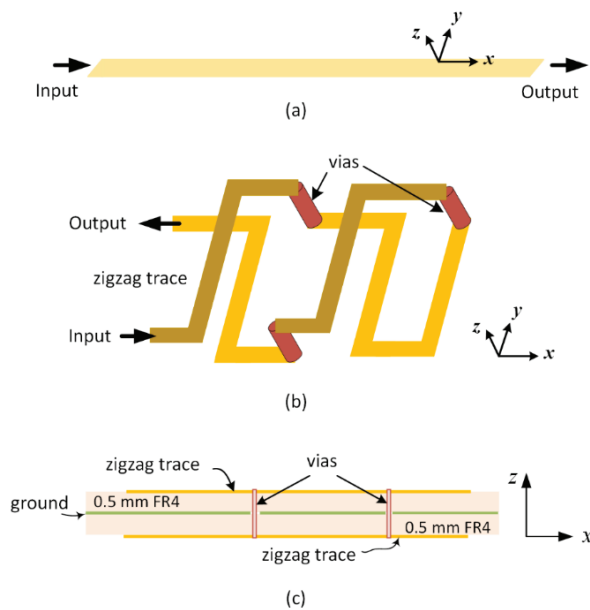


Fig. 1. Geometry of (a) conventional single straight ML, (b) proposed DP-ZML (substrates not shown), and (c) sideview of DP-ZMLs.

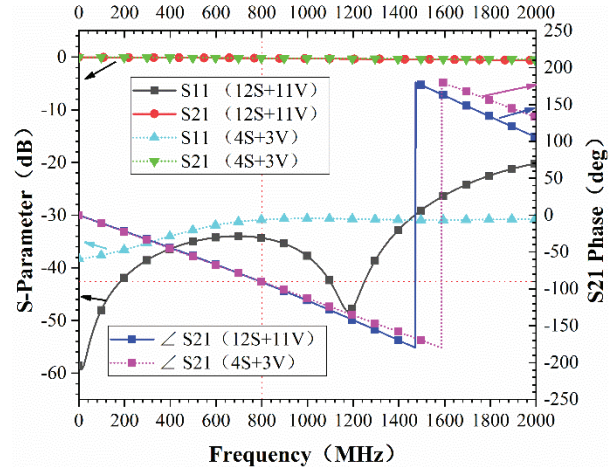


Fig. 2. Performance of zigzag MLs with 4 section and 12 section forms.

DP-ZML that owns a silent feature in reduction of coupling between microstrip lines printed on the same plane in comparison with parallel microstrip lines and or meander lines.

Figure 2 shows and compares the simulated performance of a four-section-plus-three-via (4S+3V) ZML design and a twelve-section-with-eleven-via (12S+11V) ZML design. The computed results are obtained by using a High Frequency Structure Simulator (HFSS) [12] in the frequency range of 0-2000 MHz. As seen, both the input and output reflection coefficients (S11 and S22) are tuned below -30 dB within the frequency range, whereas the neglectable insertion loss (S21) has been obtained, though a number of vias and zigzag sections have been used. These show that the internal impedance matching between the DP-ZML sections are well matched, whereas the tight schematic of the ZML shown perfect features low loss. More importantly, a quadrature phase delay at 800 MHz was obtained in both cases, and the phase delays varied linearly with frequency, viz., in the same manner with the single microstrip line.

III. QPS DESIGN METHODOLOGY AND LOGIC OPERATION

A stepwise design approach is employed to build the 4W-QPS as illustrated in Fig. 3, wherein four essential steps are described as follows:

- Step (a): design of $50\text{-}\Omega$ and $70.7\text{-}\Omega$ lines with different line widths.
- Step (b): design of 90° and 180° phase-delay ($50\text{-}\Omega$) lines with optimized number of metallic vias.
- Step (c): modular design of 2-way Wilkinson power splitter (2W-PS).
- Step (d): combination of PD lines with 2W-PSs by directly appending the PD lines to the outputs of PSs.

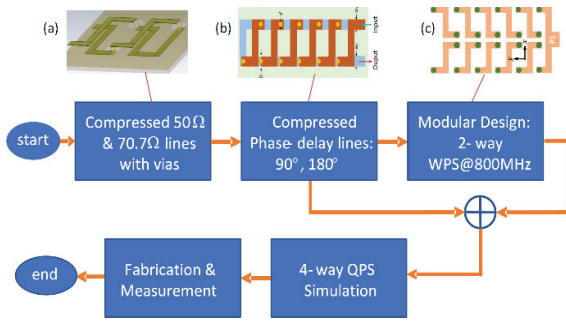


Fig. 3. Design logic-flow of 4-way QPS at 800 MHz.

After that, overall footprint optimization of 4W-QPS was undertaken using HFSS simulation, which composed of three building blocks of 2W-PS connected with three phase shifters, namely, two 90° - and one 180° -phase delays (PDs) in order to fulfill the requirement of 4W-QPS.

The geometry in the front- and back-view of the 2W-PS center at 800 MHz is shown in Fig. 4 (a), whereas its simulated performance is shown in Fig. 4 (b). As can

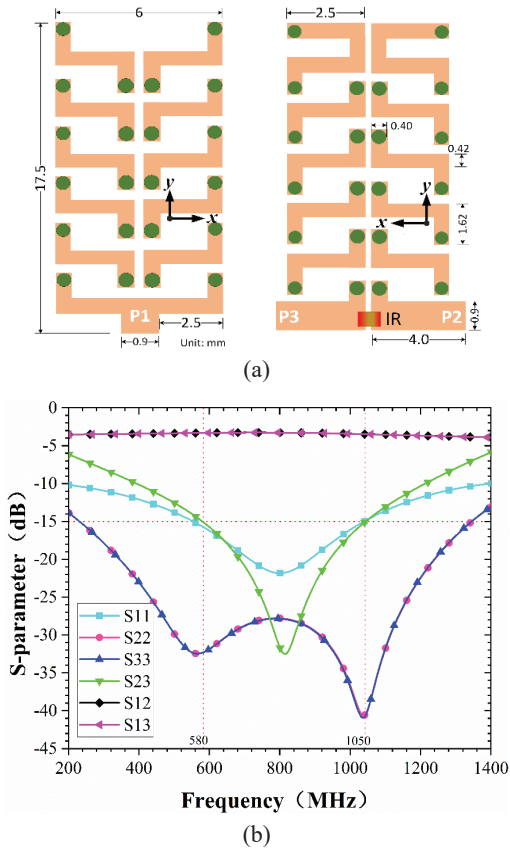


Fig. 4. Design of 2-way PS using DP-ZML at 800 MHz: (a) geometry, and (b) S-parameters performance.

be seen, the overlapped fractional bandwidth (FBW) was achieved from 580 to 1050 MHz (57.7%), wherein its return losses ($-S_{11}$ and $-S_{22}$) and isolation ($-S_{23}$) were obtained higher than 15 dB, whereas the in-band insertion losses ($-S_{21}$ and $-S_{31}$) were about 3.4 dB. Viz., an extra loss of 0.4 dB was produced when 23 ZML sections and 22 vias were used.

IV. EXPERIMENTAL VERIFICATION AND COMPARISON

In order to verify the performance of the previously discussed design approach, a prototype of 4W-QPS was fabricated by employing DP-ZMLs printed on a 0.5-mm-thick FR4 substrate ($\epsilon_r = 4.4$, $\tan\delta = 0.02$), as shown in Fig. 5. The photo illustrates the layout of the proposed QPS, including three blocks of 2W-PS, two 90° -PD and one 180° -PD. As shown, the footprint of the 4W-QPS prototype is compressed into a size of 45 mm \times 45 mm ($0.21\lambda_g \times 0.21\lambda_g$ at 786 MHz, measurement) including the SMA output connectors. Each PS is optimized to operate at a stable bandwidth while maintaining a 3-dB coupling level, whereas the PDs are used to achieve constant phase difference in specific frequency bands. Meanwhile, the isolation of the circuit configuration is enhanced by three isolation resistors (IR) of 100- Ω . Therefore, it can be clearly seen that this 4W-QPS has a very simple and compact scale to be accommodated in integrated systems that cannot accommodate the area required for long transmission lines.

The predicted results were obtained by using HFSS in the frequency range of 300-1200 MHz whereas the measurement was undertaken by a network analyzer Agilent E8363C. Both the simulated and measured results are displayed and compared in Fig. 6. In general, there is a good agreement between the simulation and the measurement. The corresponding scatter-parameter

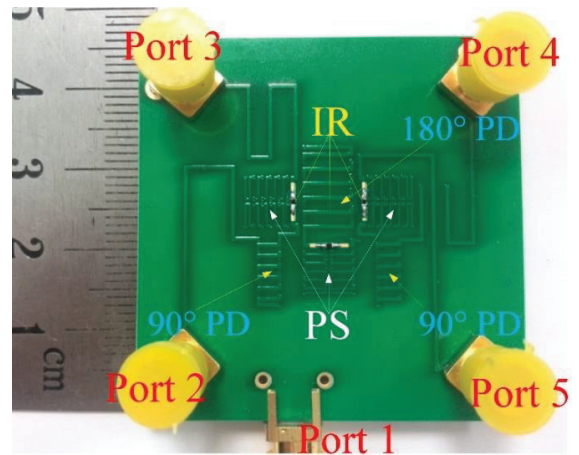


Fig. 5. Photograph of the fabricated 4-way QPS.

Table 1: Size and performance comparison of various four-way power splitters

Ref.	f_c (GHz)	4W-PSdesign	ϵ_r	Board size ($\lambda_g \times \lambda_g$)	Max EIL (dB)	15-dB FBW (%)	Iso ⁿ . at f_c (dB)
[4]	7.5	OPS	2.95	0.77×1.36	1.2	failed	17
[5]	1.0	EPS	4.5	0.52×0.52	2.0	24.4	25
[6]	1 & 2	EPS	3.66	0.54×0.45	0.2	42 & 14	24
[7]	9.3	EPS	3.5	2.21×0.27	1.5	failed	12
[8]	2.1	EPS	3.5	0.22×0.17	0.23	26.1	27
[9]	1.0	EPS	4.5	0.63×0.35	3.2	~60	32
This work	0.786	QPS	4.4	0.21×0.21	1.7	57.7	30

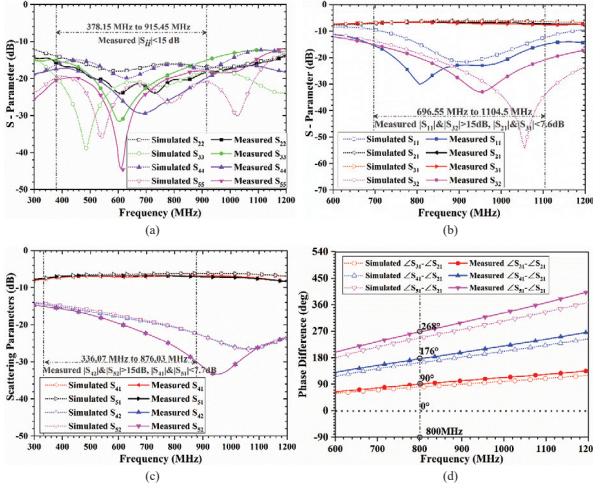


Fig. 6. Simulated and measured performance of the proposed 4W-QPS. (a) Output reflection coefficients (S₂₂, S₃₃, S₄₄ and S₅₅), (b) input reflection coefficient (S₁₁), insertion losses (S₂₁, S₃₁), and isolation ($|S_{32}|$), (c) insertion losses (S₄₁, S₅₁) and isolations (S₄₂, S₅₂), (d) output phase delays with respect to port-2.

magnitudes were recorded when exciting at the input (Port 1) with four outputs Port 2 to Port 5 (Fig. 5). An overlapped fractional bandwidth (FBW) is defined from 696.55 to 876.03 MHz, where the input and output return losses (viz., -S₁₁, -S₂₂, -S₃₃, -S₄₄, -S₅₅) and isolations between output ports (viz., -S₃₂, -S₄₂, -S₅₂) are all obtained better than 15 dB, as shown in Figs. 6 (a) to 6 (c). Moreover, the insertion losses among input and output less than 7.7 dB (maximum). Meanwhile, Fig. 6 (d) shows that the three output Ports (3, 4, and 5) of the 4W-QPS accomplish the phase difference of 0°, 90°, 176°, 268° at 800 MHz (corresponding ideal values are 0°, 90°, 180°, 270°) with respect to Port 2. These values imply a maximum phase error of 4° and a quadrature phase difference between adjacent outputs. Owing to the novel miniaturizing technique of DP-ZML, the footprint of the 4W-QPS circuit can realize a dramatic size reduc-

tion to 45 mm × 45 mm at a center frequency of 786 MHz from measurement.

Since 4-way quadrature power splitters/combiners are in high demand in RF/microwave circularly-polarized antenna arrays, but designs of 4W-QPS are hardly available from the literature, Table 1 shows the size and performance of 4-way power splitters with different output phases. Most of them are equal-phase power splitters (EPSs) and one is for a 180° out of phase power splitter (OPS). In our design, the phase delays were implemented outside the PSs using DP-ZMLs, nonetheless, with the smallest electrical size ($0.21\lambda_g \times 0.21\lambda_g$) in the Table. Meanwhile, two of the listed designs failed to commit the common 15-dB overlapping fractional bandwidth (FBW) with low levels of port isolation at center frequencies. Our design committed 57.7% FBW with an isolation of 30 dB. Moreover, the maximum extra insertion loss (Max EIL) was achieved at 1.7 dB within the measured FBW, which is an acceptable level in the comparison.

V. CONCLUSION

An ultra-compact four-way quadrature power splitter using novel DP-ZML technique is presented in this paper. Unlike broadband 4W-QPSs that typically have no specific application for 5G low-band in the literature, the design objective here is a small footprint for dedicated applications at 5G low-band NR frequencies. As considered, the devised power splitter strikes a balance between remarkable transmission characteristics, phase deviation and minimum losses. Thanks to novel compression techniques, the overall circuit size is greatly reduced ($45 \text{ mm} \times 45 \text{ mm}$) compared to conventional planar microstrip lines for an operating bandwidth of 697 to 876 MHz with a maximum quadrature phase error of 4°, which is sufficient to cover 5G low-band NR n12, n14 and n20. This experiment shows that this novel two-layer Z-shaped microstrip line structure can also be applied to other passive components for miniaturization at low cost.

ACKNOWLEDGMENT

This work is supported by the National Natural Science Foundation of China (No. 51978353) and is also supported by the Professorial and Doctoral Scientific Research Foundation of Huizhou University (No. 2021JB026).

REFERENCES

- [1] Technical Specification, 3GPP TS 38.101-1, V15.3.0. 2018-09. Accessed on 31 Aug. 2022. Available online at: https://panel.castle.cloud/view_spec/38101-1-f30/pdf/.
- [2] K. L. Chung and A. S. Mohan, "A circularly polarized stacked electromagnetically coupled patch antenna," *IEEE Trans. Antennas Propag.*, vol. 52, no. 5, pp. 1365-1370, 2004.
- [3] K. L. Chung and Y. Li, "Broadband artistic antenna array composed of circularly-polarized Wang-shaped patch elements," *AEU Intern. J. Electronics Comm.*, vol. 74, no. 4, pp. 116-122, 2017.
- [4] C.-H. Tseng and C.-L. Chang, "A broadband quadrature power splitter using metamaterial line," *IEEE Microw. Wirel. Compon. Lett.*, vol. 18, pp. 25-27, 2008.
- [5] K. L. Chung, "High-performance circularly polarized antenna array using metamaterial-line based feed network," *IEEE Trans. Antennas Propag.*, vol. 61, no. 12, pp. 6233-6237, 2013.
- [6] K. Song, Y. Mo, Q. Xue, and Y. Fan, "Wideband four-way out-of-phase slotline power dividers," *IEEE Trans. Ind. Electron.*, vol. 61, no. 7, pp. 3598-3606, 2014.
- [7] T. Yu, J.-H. Tsai, and Y. Chang, "A radial four-way power divider with the proposed isolation network," *IEEE Microw. Wirel. Compon. Lett.*, vol. 28, no. 3, pp. 194-196, 2018.
- [8] T. Zhang, W. Che, H. Chen, and W. Feng, "A compact four-way dual-band power divider using lumped elements," *IEEE Microw. Wirel. Compon. Lett.*, vol. 25, no. 2, pp. 94-96, 2015.
- [9] K. Song, S. Guo, and Y. Fan, "Four-way chained quasi-planar slotted-HMSIW power divider," *IEEE Microw. Wirel. Compon. Lett.*, vol. 28, no. 2, pp. 117-119, 2018.
- [10] B. Zhang, K. Song, X. Wang, Y. Yan, Y. Zhou, and Y. Fan, "Compact quasi-planar four-way power divider with wide isolation bandwidth," *IEEE Access*, vol. 7, pp. 77915-77922, 2019.
- [11] T. Yu and J.-H. Tsai, "Design of multiway power dividers including all connecting lines," *IET Microwaves, Antennas & Propag.*, vol. 12, no. 8, pp. 1367-1374, 2018.
- [12] Ansoft High Frequency Structure Simulation (HFSS), ver. 10, Ansoft Corporation, Pittsburgh, PA, 2005.



Song Gao received his M.E. degree from the University of Stellenbosch South Africa in 2005 and his Ph.D. degree from Qingdao University of Technology (QUT) in 2013. He is now a full professor at the School of Civil Engineering, QUT, where he is also the head of the engineering materials laboratory. His main research interests are civionics transducers, high performance fiber reinforced cementation composites and high-performance building materials using recycled building waste.



Hao Wang was born in December 1997, Weifang, China. He received his Bachelor's degree from Qingdao Agricultural University in 2020. He is currently pursuing a Master's degree at QUT. His research interests include concrete structures and antenna-based sensors for structural health monitoring. In 2021, he participated in the IEEE ICEICT conference and received the "Best Paper Award". In 2022, he won second place in QUT's comprehensive scholarship prize.



Kwok L. Chung (Senior Member, IEEE) was a Research Professor and a supervisor of Ph.D. students at Qingdao University of Technology (QUT) from Dec. 2005 to Jan. 2021. He was the Director of Civionics Research Laboratory at QUT, where he led a cross-disciplinary research team for structural health monitoring. In April 2021, he joined Huizhou University as a Distinguished Professor. He has authored and coauthored about 180 publications [science citation index (SCI) and engineering index (EI)] in various areas of electrical and civil engineering. His current research interests include passive wireless sensors, cement-based materials design and characterization, clothing antennas, and intelligent reconfigurable surfaces.

Prof. Chung has been classified as one of the world's top 2% scientists in the 2020 and 2021 lists released by Stanford University. He is the Founding Chair of the IEEE Qingdao AP/MTT/COM joint chapter (CN10879) Beijing Section. He has been an Associate Editor of *IEEE Access* and an Associate Editor of Elsevier's

Alexandria Engineering Journal since 2016 and 2020, respectively. He is an active reviewer for numerous international journals from IEEE, Elsevier, IOPscience, and many others.



Yingsong Li received his B.S. degree in Electrical and Information Engineering, and M.S. degree in Electromagnetic Field and Microwave Technology from Harbin Engineering University, 2006 and 2011, respectively. He received his Ph.D. degree from both Kochi University of Technology (KUT), Japan and Harbin Engineering University (HEU), China in 2014. He is currently a full professor at the School of Electronic and Information Engineering at Anhui University since March 2022. He was a full professor in HEU from 2014 to 2022 and a visiting scholar at the University of California, Davis, from March 2016 to March 2017, a visiting professor at the University of York, UK in 2018, a visiting professor at the Far Eastern Federal University (FEFU) and KUT. Since 2018 he has held a visiting professorship at the School of Information of KUT from 2018. He is a Fellow of the Applied Computational Electromagnetics Society, and is also a senior member of the Chinese Institute of Electronics (CIE) and IEEE. He has authored and coauthored about 300 journal and conference papers in various areas of electrical and information engineering. His current research interests include signal processing, adaptive filters, metasurface designs and microwave antennas.

Dr. Li served as an Area Editor of *AEÜ-International Journal of Electronics and Communications* from 2017 to 2020. He is an Associate Editor of *IEEE Access*, *Applied Computational Electromagnetics Society (ACES) Journal*, the *Alexandria Engineering Journal* and *Electromagnetic Science*.

He was the TPC Co-Chair of the 2019 IEEE International Workshop on Electromagnetics (iWEM 2019-2020), 2019 IEEE 2nd International Conference on Electronic Information and Communication Technology (ICEICT 2019), 2019 International Applied Computational Electromagnetics Society (ACES) Symposium-China, 2019 Cross Strait Quad-regional Radio Science and the Wireless Technology Conference (2019 CSQRWC). He acts as a reviewer of numerous IEEE, IET, Elsevier and other international journals and conferences.



Kangtai Zheng (Student Member, IEEE) was born in April 2001, Guangdong, China. He is currently studying for a Bachelor's degree at the School of Computer Science and Computer Engineering at Huizhou University. His research interests include microwave antennas and components, intelligent reconfigurable surfaces and deep learning. In 2022, he participated in the 13th IEEE iWEM conference and received the "Finalist Award".



Luqi Chen (Student Member, IEEE) was born in March 2001, Guangzhou, China. She is currently pursuing a Bachelor's degree in the international class of Huizhou University. Her research interests include active and passive reconfigurable intelligent surfaces, miniaturization of power dividers and artificial intelligence. She won the best paper award in the first author category at the 2022 IEEE 5th International Conference on Electronic Information and Communication Technology (ICEICT).

Removing the Froissart Doublets in a Rational Interpolation Based on Loewner Matrix

Haobo Yuan¹, Jungang Ren¹, Yujie Li², and Xiaoming Huang¹

¹National Key Laboratory of Antenna and Microwave Technology
Xidian University, Xi'an, 710071, China
hbyuan@mail.xidian.edu.cn, renjungang20@gmail.com, hxm.0314@126.com

²Hangzhou Institute of Technology
Xidian University, Hangzhou, 311200, China
liyujie3128@163.com

Abstract – In order to implement wide band frequency sweeping, the S-parameters can be fitted with an adaptive rational interpolation based on Loewner matrix. However, the errors in the sampling data may lead to Froissart doublets, which look like spikes in the curve. In this paper, a novel technique is proposed to remove these doublets. At first, the rational expression is converted into the sum of partial fractions by solving two generalized eigenvalue problems. After that, the partial fraction term with the smallest imaginary part of the pole and relatively large absolute value is considered to generate the doublets. Removing this term results in a smooth rational polynomial, which is validated by the example of a passive circuit simulated by finite element method (FEM).

Index Terms – finite element method, Froissart doublets, rational interpolation, S-parameter.

I. INTRODUCTION

Characterizing a passive electromagnetic structure can be challenging. A commonly used approach is obtaining the S-parameters through simulating the structure by frequency domain computational electromagnetic (CEM) methods at first. Then, a rational interpolation is utilized to fit the S-parameters over a wide frequency band, which afterwards is processed by fast Fourier transform to acquire the time domain response of the structure.

Interpolation is widely employed in the analyses of electromagnetic problems [1–7]. Of all the interpolation methods, many deal with rational interpolation, such as vector fitting [8], Padé approximant [9, 10], minimal rational interpolation [11], adaptive rational interpolation based on Loewner matrix (ARILM) [12], etc. However, rational interpolation often suffers from instability. Due to the roundoff error, it could

be difficult to compute rational polynomials in finite precision arithmetic, especially for higher degree numerators and denominators. On the other hand, the sampling data at discrete frequencies obtained by CEM often contains numerical errors, and the curve that goes through these points is not exactly a rational polynomial. Subsequently, the interpolated rational polynomial may have a spike-like spurious resonant point in the plot, which is termed as Froissart doublets. Theoretically speaking, Froissart doublets are a pair of points in a rational polynomial, one a pole and the other a zero, which are adjacent to each other and cannot be canceled [13]. This makes it difficult to obtain smooth functions with such rational polynomials.

Among all the rational interpolation techniques, ARILM is shown to be the most stable and efficient one. It is insensitive to roundoff error, for the underlying Loewner matrix is well-conditioned. However, ARILM also suffers from the Froissart doublets, since only approximated S-parameters rather than the precise ones can be yielded by CEM. As an outgrowth of ARILM, this paper focuses on how to determine and remove the doublets in the rational interpolation efficiently.

There are many strategies to handle these doublets. As a well-known rational interpolation technique, Padé approximants are very fragile to roundoff errors in the coefficients of the numerator and denominator polynomials. It can be stabilized by a lower order Padé approximant based on the SVD of the Toeplitz matrix [14, 15], which performs hopping across a square block of the Padé table to find the minimal degree denominator. However, this technique is inapplicable to ARILM. Some have proposed to remove the doublets in Padé approximants by reducing the roundoff errors with the extended precision arithmetic. Unfortunately, this technique is much more time-consuming than the commonly used double precision arithmetic [16–18]. Beckermann

introduced three different parameters to monitor the absence of Froissart doublets for a given general rational function [13]. He further planned to remove the undesirable doublets using the three parameters as penalties, but such a work has remained unreported as yet. Nakatsukasa proposed the AAA algorithm to construct the barycentric rational polynomial with the S-parameters at certain sampling points and select the points greedily to avoid exponential instabilities [19]. It identified spurious poles by their residues with a very small threshold. Then these doublets are removed by deleting the nearest sampling points from the set of frequencies. This method is truly applicable to ARILM, but it is obviously inefficient, since acquiring a single sampling point by CEM may be computationally expensive. Besides, removing the Froissart doublets is of great practical significance to filter the noise in the measured signals [15, 18–20–21]. But only the numerically simulated signals will be addressed in this paper.

This paper proposes a novel technique to remove the doublets arising in the ARILM. At first, the S-parameters of a passive circuit network are acquired by finite element method (FEM). Next, the ARILM is applied to capture the set of frequencies required to perform wide frequency band sweeping. After that, the obtained barycentric rational polynomial is converted into a partial fraction expression. Then, the partial fraction term with the smallest imaginary part of the pole and relatively large absolute value is considered to generate the doublets. Removing such a term leads to a smooth rational polynomial.

II. RATIONAL INTERPOLATION BASED ON LOEWNER MATRIX

Suppose there are $2p-1$ data points obtained by FEM:

$$f(s_i) = f_i, (i = 1, 2, 3, \dots, 2p-1), \quad (1)$$

where $0 = s_1 < s_2 < \dots < s_{2p-1} = 1$ are the normalized frequencies, and $f(s)$ is the unknown frequency response function. All the points are partitioned into two groups:

$$f(\lambda_i) = w_i (i = 1, 2, 3, \dots, p), \quad (2)$$

$$f(\mu_j) = v_j (j = 1, 2, 3, \dots, p-1). \quad (3)$$

With equation (2), $f(s)$ can be expressed by the following barycentric rational polynomial:

$$f_L(s) = \frac{\sum_{i=1}^p \alpha_i w_i}{s - \lambda_i} / \frac{\sum_{i=1}^p \alpha_i}{s - \lambda_i}, \quad (4)$$

where $\alpha_i (i = 1, \dots, p)$ are unknown coefficients to be determined by the following equation:

$$f_L(\mu_j) = \frac{\sum_{i=1}^p \alpha_i w_i}{\mu_j - \lambda_i} / \frac{\sum_{i=1}^p \alpha_i}{\mu_j - \lambda_i} = v_j. \quad (5)$$

Equation (5) leads to the condition:

$$\sum_{i=1}^p \frac{v_j - w_i}{\mu_j - \lambda_i} \alpha_i = 0, \quad (6)$$

which is written in compact matrix form as:

$$\begin{bmatrix} \frac{v_1 - w_1}{\mu_1 - \lambda_1} & \dots & \frac{v_1 - w_p}{\mu_1 - \lambda_p} \\ \vdots & \frac{v_j - w_i}{\mu_j - \lambda_i} & \vdots \\ \frac{v_{p-1} - w_1}{\mu_{p-1} - \lambda_1} & \dots & \frac{v_{p-1} - w_p}{\mu_{p-1} - \lambda_p} \end{bmatrix} \begin{bmatrix} \alpha_1 \\ \vdots \\ \alpha_p \end{bmatrix} = 0. \quad (7)$$

The system matrix on the left side is the so-called Loewner matrix, and the unknown coefficients can be readily evaluated by the SVD of the Loewner matrix. And then the rational polynomial (4), termed as the Loewner interpolation, goes through all the $2p-1$ points. Furthermore, an adaptive procedure is introduced in [12] to perform the interpolation efficiently.

III. REMOVING FROISSART DOUBLETS IN RATIONAL INTERPOLATION

A. Observe the Froissart doublets

If the S-parameters of a circuit are acquired by FEM and interpolated by ARILM, often a smooth rational polynomial can be obtained. However, sometimes, the interpolated rational polynomial has a spike in the curve, given the term Froissart doublets. Froissart doublets are mainly owing to the numerical errors of the S-parameters at the sampling frequencies. Let's explain the cause of the Froissart doublets with a simple partial fraction as:

$$f(s) = \frac{1.0 + j2.0}{s - (0.5 + j0.001)}, 0 \leq s \leq 1, \quad (8)$$

which has a pole and a residual. Actually, the real part of the pole represents the normalized resonant frequency, while the imaginary part indicates the power loss of the corresponding circuit. If the imaginary part of the pole is very small, the circuit is close to lossless, and there will be a resonance, which is characterized by a spike in the curve as in Fig. 1.

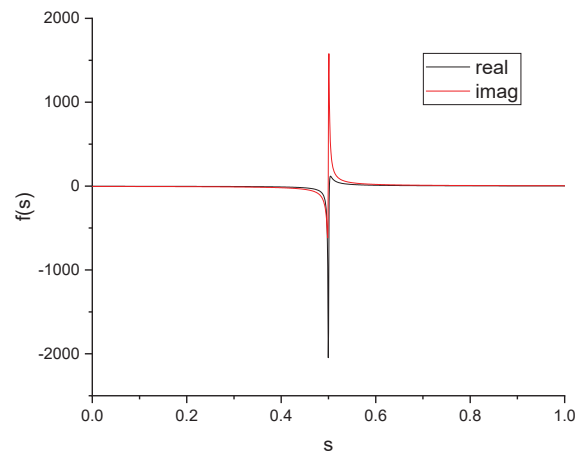


Fig. 1. A partial fraction with Froissart doublets.

This partial fraction expression has an advantage over the barycentric rational polynomial in that it indicates the location of the spike. Therefore, the latter will be converted into the sum of the former. Then, the residual and pole of every partial fraction term will be analyzed to find the connection among the spike, the poles, and the residuals.

B. Convert the Loewner interpolation into the partial fraction expression

Loewner interpolation can be rewritten as:

$$f_L(s) = \sum_{i=1}^p \frac{\alpha_i w_i}{s - \lambda_i} / \sum_{i=1}^p \frac{\alpha_i}{s - \lambda_i} \triangleq N/D. \quad (9)$$

The zeros of N are also the zeros of $f_L(s)$, while the zeros of D are the poles of $f_L(s)$. The zeros of D can be obtained by solving the following equation:

$$D = \sum_{i=1}^p \frac{\alpha_i}{s - \lambda_i} = 0. \quad (10)$$

This equation is equivalent to a generalized eigenvalue problem:

$$\begin{bmatrix} 0 & \alpha_1 & \alpha_2 & \cdots & \alpha_p \\ 1 & \lambda_1 & & & \\ 1 & & \lambda_2 & & \\ \vdots & & & \ddots & \\ 1 & & & & \lambda_p \end{bmatrix} \begin{bmatrix} x_0 \\ x_1 \\ x_2 \\ \vdots \\ x_{p+1} \end{bmatrix} = \lambda \begin{bmatrix} 0 & & & & \\ & 1 & & & \\ & & 1 & & \\ & & & \ddots & \\ & & & & 1 \end{bmatrix} \begin{bmatrix} x_0 \\ x_1 \\ x_2 \\ \vdots \\ x_{p+1} \end{bmatrix}, \quad (11)$$

which can be solved readily. Similarly, the zeros of N can be attained by solving another generalized eigenvalue problem:

$$\begin{bmatrix} 0 & \alpha_1 w_1 & \alpha_2 w_2 & \cdots & \alpha_p w_p \\ 1 & \lambda_1 & & & \\ 1 & & \lambda_2 & & \\ \vdots & & & \ddots & \\ 1 & & & & \lambda_p \end{bmatrix} \begin{bmatrix} x_0 \\ x_1 \\ x_2 \\ \vdots \\ x_{p+1} \end{bmatrix} = \lambda \begin{bmatrix} 0 & & & & \\ & 1 & & & \\ & & 1 & & \\ & & & \ddots & \\ & & & & 1 \end{bmatrix} \begin{bmatrix} x_0 \\ x_1 \\ x_2 \\ \vdots \\ x_{p+1} \end{bmatrix}. \quad (12)$$

Once all the poles and residuals are obtained, formula (9) can be converted into the pole-zero expression:

$$f_L(s) = N/D = d \prod_{i=1}^{p-1} (s - c_i) / \prod_{i=1}^{p-1} (s - b_i). \quad (13)$$

The constant d can be determined by any one of the sampling points, say (λ_1, w_1) , as:

$$d = w_1 \prod_{i=1}^{p-1} (\lambda_1 - b_i) / \prod_{i=1}^{p-1} (\lambda_1 - a_i). \quad (14)$$

Then, the pole-zero expression is rewritten as the sum of partial fractions:

$$d \prod_{i=1}^{p-1} (s - c_i) / \prod_{i=1}^{p-1} (s - b_i) = \sum_{i=1}^{p-1} \frac{a_i}{s - b_i} + a_0, \quad (15)$$

where both sides have the identical poles and only the residuals a_i remain unknown. Since the partial fraction expression goes through the sampling points in (2), we have:

$$\begin{bmatrix} 1 & \frac{1}{\lambda_1 - b_1} & \frac{1}{\lambda_1 - b_2} & \cdots & \frac{1}{\lambda_1 - b_{p-1}} \\ 1 & \frac{1}{\lambda_2 - b_1} & \frac{1}{\lambda_2 - b_2} & \cdots & \frac{1}{\lambda_2 - b_{p-1}} \\ \vdots & & & \ddots & \\ 1 & \frac{1}{\lambda_{p-1} - b_1} & \frac{1}{\lambda_{p-1} - b_2} & \cdots & \frac{1}{\lambda_{p-1} - b_{p-1}} \end{bmatrix} \begin{bmatrix} a_0 \\ a_1 \\ a_2 \\ \vdots \\ a_{p-1} \end{bmatrix} = \begin{bmatrix} w_1 \\ w_2 \\ w_3 \\ \vdots \\ w_p \end{bmatrix}. \quad (16)$$

Finally, the residuals a_i are attained, and the barycentric rational polynomial (4) is converted into the partial fraction expression:

$$f_L(s) = \sum_{i=1}^p \frac{\alpha_i w_i}{s - \lambda_i} / \sum_{i=1}^p \frac{\alpha_i}{s - \lambda_i} = \sum_{i=1}^{p-1} \frac{a_i}{s - b_i} + a_0. \quad (17)$$

C. Find and remove Froissart doublets

As discussed before, the Froissart doublets may be introduced by a partial fraction term, whose pole has a very small imaginary part. Therefore, we check every partial fraction term in (17) to determine which one may cause the doublets. As for the k^{th} term, we divide (17) into two parts:

$$f_L(s) = \left[\frac{a_k}{s - b_k} \right] + \left[\sum_{\substack{i=1 \\ i \neq k}}^{p-1} \frac{a_i}{s - b_i} + a_0 \right] \triangleq f_k(s) + f_R(s), \quad (18)$$

where the poles are denoted by $b_i = b_{ix} + j b_{iy}$, and ε is a threshold to judge the doublets. If $b_{ky} = \min_{i=1, \dots, p-1} (|b_{iy}|)$ and $|f_k(b_{kx})| > |f_R(b_{kx})| \times \varepsilon$, there are doublets located at b_{kx} .

In order to remove the doublets, we delete the k^{th} term in the partial fraction expression. In other words, $f_L(s)$ is approximated by $f_R(s)$. And then, the original sampling points are replaced with those computed by $f_R(s)$:

$$f_R(s_i) = f_i^*, \quad (i = 1, 2, 3, \dots, 2p - 1). \quad (19)$$

Finally, we construct another Loewner interpolation with these $(2p - 1)$ new sampling points:

$$f_L^*(s) = \sum_{i=1}^p \frac{\alpha_i^* w_i^*}{s - \lambda_i} / \sum_{i=1}^p \frac{\alpha_i^*}{s - \lambda_i}, \quad (20)$$

which will be smooth and have no Froissart doublets.

IV. NUMERICAL RESULTS

Figure 2 shows a passive circuit with 26 ports, which is simulated by FEM to obtain the S-parameters over a

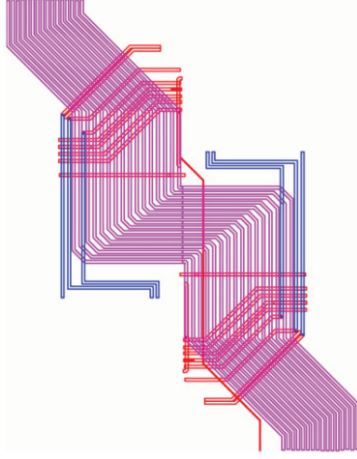


Fig. 2. The 26-port passive circuit being simulated.

very wide frequency band from 0.1 GHz to 250 GHz. We use ARILM to accomplish the wide band frequency sweeping, which starts with 3 sampling points and converges with 21 points. Note that all the S-parameters are interpolated with the same 21 frequencies. In order to determine the doublets, we set the threshold $\varepsilon = 1.0$.

The curve of $S_{26,1}$ is shown in Figs. 3 and 4. The interpolated rational polynomial has a spike at 157.6 GHz. Table 1 shows that the third partial fraction satisfies $b_{3y} = \min_{i=1, \dots, p-1}(|b_{iy}|)$ and $|f_3(b_{3x})| > |f_R(b_{3x})| \times \varepsilon$, where $b_{3x} = 0.6305$ corresponds to 157.6 GHz. Therefore, the third partial fraction causes the spike. Figures 3 and 4 show that the Froissart doublets are removed by the proposed method and the resulting curves are still a good approximation to the reference curves.

The curves of $S_{25,10}$ are shown in Figs. 5 and 6. The interpolated rational polynomial has a spike at

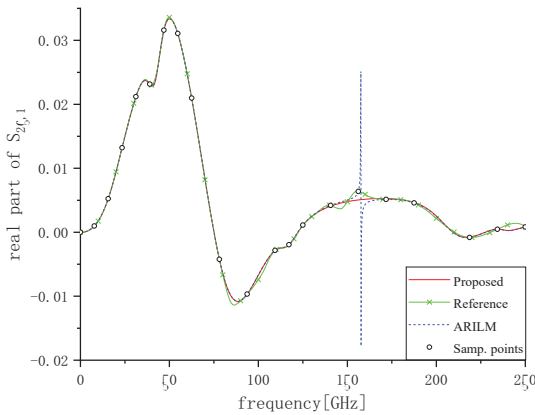


Fig. 3. Real parts of $S_{26,1}$.

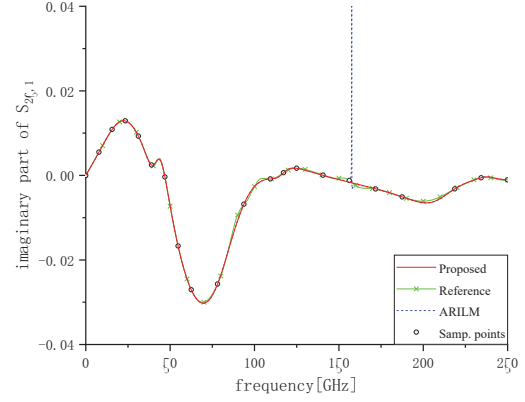


Fig. 4. Imaginary parts of $S_{26,1}$.

Table 1: Residuals, poles, and function values of $S_{26,1}$

No.	Residual a_i	Pole $b_{ix} + jb_{iy}$	$f_k(b_{kx})$	$f_R(b_{kx})$
1	-0.000028	0.952253	0.000952	0.000604
	-j0.000008	-j0.028919	+j0.000272	-j0.001296
2	-0.000315	0.836766	-0.004134	0.004356
	+j0.000332	+j0.076300	+j0.004345	-j0.001552
3	-0.000008	0.630471	0.073629	0.005099
	-j0.000002	-j0.000103	+j0.021013	-j0.001753
4	-0.000034	0.463729	0.001191	0.000447
	+j0.000076	+j0.028439	+j0.002662	+j0.001365
5	-0.000724	0.328455	-0.007271	0.027796
	+j0.003600	+j0.099524	+j0.036169	-j0.013676
6	0.000019	0.326027	-0.000260	-0.008067
	+j0.000014	-j0.072588	-j0.000192	-j0.021470
7	0.000529	-0.202759	0.009192	-0.006324
	-j0.003231	+j0.057593	-j0.056095	+j0.003122
8	0.003413	0.157954	0.032789	-0.011102
	-j0.003550	+j0.104093	-j0.034107	-j0.030392
9	0.000085	0.168986	0.003820	0.036364
	+j0.000278	+j0.022184	+j0.012519	-j0.000254
10	0.000197	0.087280	0.003678	0.008093
	-j0.000179	+j0.053472	-j0.003353	+j0.009259

33.32 GHz. As is shown in Table 2, this spike is generated by the ninth partial fraction, in which $b_{9x} = 0.1329$ corresponds to 33.32 GHz. Figures 5 and 6 show that after removing the spike, the curves obtained by the proposed method are in good agreement with the reference curves.

The curves of $S_{26,20}$ are given in Fig. 7, which has no spike. Table 3 shows that the fifth partial fraction has the minimum imaginary part, but $|f_5(b_{5x})| > |f_R(b_{5x})| \times \varepsilon$ is not satisfied. Therefore, the above three S-parameters validate the efficacy of the proposed method, which can exactly identify the partial fraction with Froissart doublets.

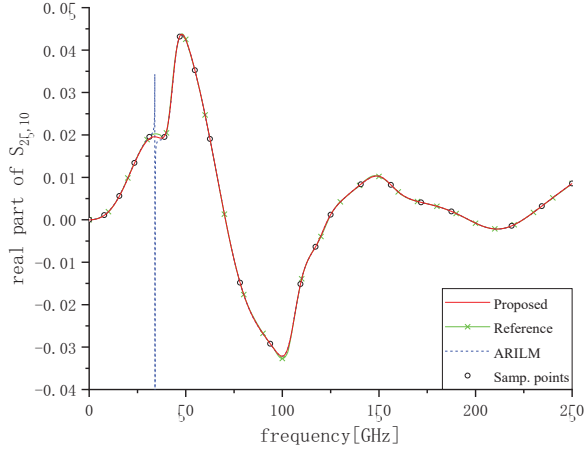


Fig. 5. Real parts of $S_{25,10}$.

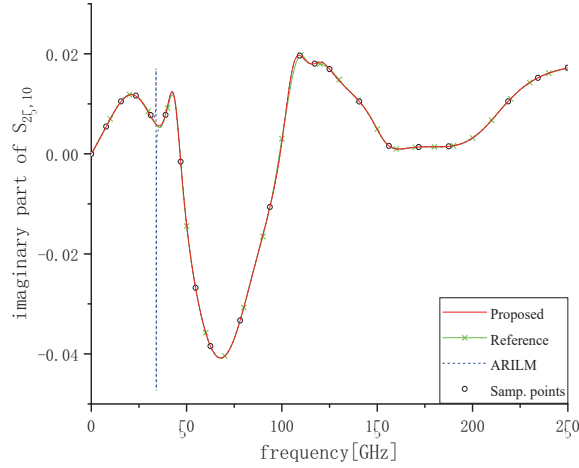


Fig. 6. Imaginary parts of $S_{25,10}$.

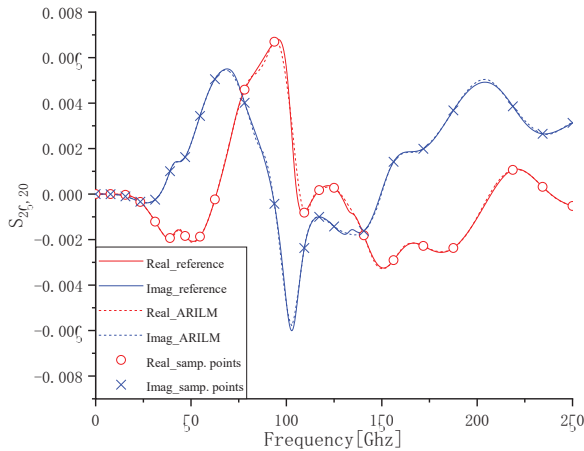


Fig. 7. Real parts and imaginary parts of $S_{26,20}$.

Table 2: Residuals, poles, and function values of $S_{25,10}$

No.	Residue	Pole	$f_k(b_{kx})$	$f_R(b_{kx})$
1	-0.002966	1.275554	0.218629	0.004306
	-j0.001250	-j0.013567	+j0.092157	+j0.009232
2	-0.000735	0.834878	-0.005848	0.010899
	+j0.001602	+j0.125776	+j0.012736	+j0.011212
3	-0.000254	0.609035	-0.005195	0.005349
	-j0.000258	+j0.048807	-j0.005294	+j0.008287
4	0.000137	0.476290	0.004186	0.000630
	+j0.000162	+j0.032733	+j0.004946	+j0.015302
5	0.000615	0.419796	0.018121	-0.013543
	+j0.000448	+j0.033937	+j0.013208	-j0.001148
6	-0.005674	0.285817	-0.050893	0.026137
	+j0.003293	+j0.111489	+j0.029541	+j0.010261
7	0.000603	0.172140	0.027729	0.034888
	+j0.000059	+j0.021737	+j0.002702	-j0.015548
8	0.003731	0.088112	0.036113	0.018777
	+j0.000644	+j0.103326	+j0.006236	-j0.024063
9	-0.000004	0.132949	-0.086857	0.020033
	-j0.000003	+j0.000041	-j0.076599	+j0.005948
10	0.000183	-0.051439	-0.003142	0.000234
	-j0.000006	-j0.058124	+j0.000098	-j0.003244

Table 3: Residuals, poles, and function values of $S_{26,20}$

No.	Residue	Pole	$f_k(b_{kx})$	$f_R(b_{kx})$
1	-0.004838	-1.362713	0.019640	0.004869
	-j0.008596	-j0.246348	+j0.034892	+j0.007194
2	-0.000198	0.887203	-0.001928	-0.002806
	-j0.000400	+j0.102572	-j0.003898	+j0.005414
3	-0.001274	0.672367	-0.009615	0.000149
	+j0.000307	+j0.132489	+j0.002316	+j0.011496
4	0.000217	0.605122	0.002880	0.004231
	+j0.000564	+j0.075424	+j0.007479	-j0.002434
5	0.000005	0.534310	0.000364	-0.000469
	+j0.000005	+j0.013026	+j0.000349	-j0.001958
6	-0.000191	0.412166	-0.007484	0.003694
	+j0.000034	+j0.025577	+j0.001314	+j0.001489
7	0.000023	0.295191	0.000788	0.002878
	-j0.000019	+j0.029625	-j0.000634	+j0.004267
8	0.000300	0.224718	0.003387	0.003941
	+j0.000497	+j0.088547	+j0.005611	+j0.000424
9	0.000023	0.166183	0.001129	-0.002189
	-j0.000010	+j0.020046	-j0.000508	+j0.000268
10	0.000003	0.091299	0.000045	-0.001142
	-j0.000053	+j0.063231	-j0.000837	-j0.000366

V. CONCLUSION

This paper proposes a new technique to remove the Froissart doublets in an adaptive rational interpolation based on the Loewner matrix. Numerical results indicate the efficacy of the proposed method. Although the proposed technique is tailored for ARILM, it is also applicable to other rational interpolations. In addition,

the threshold ε is manually set according to specific circuits, and it will be chosen automatically in future.

ACKNOWLEDGMENT

This work is supported partially by the Natural Science Basic Research Program of Shaanxi Province (Program No. 2021JM-129).

REFERENCES

- [1] A. Karwowski, A. Noga, and T. Topa, "Computationally efficient technique for wide-band analysis of grid-like spatial shields for protection against LEMP effects," *Applied Computational Electromagnetics Society (ACES) Journal*, vol. 32, no. 1, pp. 87-92, 2017.
- [2] Y. Zhang, D. Huang, and J. Chen, "Combination of asymptotic phase basis functions and matrix interpolation method for fast analysis of monostatic RCS," *Applied Computational Electromagnetics Society (ACES) Journal*, vol. 28, no. 1, pp. 49-56, 2013.
- [3] S. M. Seo, C. Wang, and J. Lee, "Analyzing PEC scattering structure using an IE-FFT algorithm," *Applied Computational Electromagnetics Society (ACES) Journal*, vol. 24, no. 2, pp. 116-128, 2009.
- [4] D. Schobert and T. Eibert, "Direct field and mixed potential integral equation solutions by fast Fourier transform accelerated multilevel Green's function interpolation for conducting and impedance boundary objects," *Applied Computational Electromagnetics Society (ACES) Journal*, vol. 26, no. 12, pp. 1016-1023, 2011.
- [5] F. S. de Adana, O. Gutiérrez, L. Lozano, and M. F. Cátedra, "A new iterative method to compute the higher order contributions to the scattered field by complex structures," *Applied Computational Electromagnetics Society (ACES) Journal*, vol. 21, no. 2, pp. 115-125, 2006.
- [6] Y. Zhang, Z. Wang, F. Zhang, X. Chen, J. Miao, and W. Fan, "Phased array calibration based on measured complex signals in a compact multiprobe setup," *IEEE Antennas and Wireless Propagation Letters*, vol. 21, no. 4, pp. 833-837, 2022.
- [7] Z. Liu, R. Chen, D. Ding, and L. He, "GTD model based cubic spline interpolation method for wide-band frequency- and angular- sweep," *Applied Computational Electromagnetics Society (ACES) Journal*, vol. 26, no. 8, pp. 696-704, 2011.
- [8] B. Gustavsen and A. Semlyen, "Rational approximation of frequency domain responses by vector fitting," *IEEE Transactions on Power Delivery*, vol. 14, no. 3, pp. 1052-1061, Jul. 1999.
- [9] G. A. Baker, J. L. Gammel, and J. G. Wills, "An investigation of the Padé approximant method," *Journal of Mathematical Analysis & Applications*, vol. 2, no. 1, pp. 405-418, 1961.
- [10] B. Essakhi and L. Pichon, "An efficient broadband analysis of an antenna via 3D FEM and Padé approximation in the frequency domain," *Applied Computational Electromagnetics Society (ACES) Journal*, vol. 2, no. 1, pp. 143-148, 2006.
- [11] A. C. Antoulas, J. A. Ball, J. Kang, and J. C. Willems, "On the solution of the minimal rational interpolation problem," *Linear Algebra and its Applications*, vol. 137-138, no. 4805, pp. 511-573, 1990.
- [12] H. Yuan, W. Bao, C. Lee, B. F. Zinser, S. Campione, and J. Lee, "A method of moments wide band adaptive rational interpolation method for high-quality factor resonant cavities," *IEEE Transactions on Antennas and Propagation*, vol. 70, no. 5, pp. 3595-3604, May, 2022.
- [13] B. Beckermann, G. Labahn, and A. C. Matos, "On rational functions without Froissart doublets," *Numerische Mathematik*, vol. 138, pp. 615-633, 2018.
- [14] P. Gonnet, S. Guttel, and L. N. Trefethen, "Robust Padé approximation via SVD," *SIAM Review*, vol. 55, pp. 101-117, Mar. 2013.
- [15] J. Gilewicz and Y. Kryakin, "Froissart doublets in Padé approximation in the case of polynomial noise," *Journal of Computational and Applied Mathematics*, no. 153, pp. 235-242.
- [16] R. P. Brent, F. G. Gustavson, and D. Y. Y. Yun, "Fast solution of Toeplitz systems of equations and computation of Padé approximants," *Journal of Algorithms*, vol. 1, pp. 259-295, 1980.
- [17] D. Belkić and K. Belkić, "Padé-Froissart exact signal-noise separation in nuclear magnetic resonance spectroscopy," *Journal of Physics B*, vol. 44, pp. 1-19, 2011.
- [18] D. Bessis, "Padé approximations in noise filtering," *Journal of Computational and Applied Mathematics*, vol. 66, pp. 85-88, 1996.
- [19] Y. Nakatsukasa, O. Sète, and L. N. Trefethen, "The AAA algorithm for rational approximation," *SIAM Journal on Scientific Computing*, vol. 40, no. 3, pp. A1494-A1522, 2018.
- [20] J. Gilewicz and M. Pindor, "Padé approximants and noise: A case of geometric series," *Journal of Computational and Applied Mathematics*, vol. 87, pp. 199-214, 1997.
- [21] J. Gilewicz and M. Pindor, "Padé approximants and noise: Rational functions," *Journal of Computational and Applied Mathematics*, vol. 105, no. 1, pp. 285-297, 1999.



Haobo Yuan was born in Tianmen, Hubei, China, in 1980. He received his B.S., M.S., and Ph.D. degrees in Electromagnetic Fields and Microwave Technology from Xidian University, Xi'an, China, in 2003, 2006, and 2009, respectively. Since 2006, he has been with the

School of Electronic Engineering, Xidian University, where he is an Associate Professor. He was a post doctoral researcher at Ohio State University in 2019. His current research interests include computational electromagnetics, antenna measurements, and electromagnetic compatibility.



Jungang Ren was born in Xi'an, Shaanxi, China, in 1998. He received his B.Eng. degree in Electronic Information Engineering from Xidian University, Xi'an, China, in 2020. He is currently working towards an M.S. degree with Xidian University. His research

interests are numerical techniques in computational electromagnetics.



Yujie Li received her B.Eng. degree in Electronic Information Engineering from the North University of China, Taiyuan, China in 2017. She is currently pursuing an M.Eng. degree with Xidian University. Her research interests are antenna measurement techniques and numerical methods in computational electromagnetics.



Xiaoming Huang received his B.Eng. degree in Electrical Engineering from Zhengzhou University, Henan, China, in 2021. He is currently pursuing an M.S. degree with Xidian University, Xi'an. His research interests are the numerical techniques in computational

electromagnetics.

Super-Broadband Rectifier with Wide-band Resistance Compression Network and Harmonic Cycling for RF-Harvesting

Xin Liu¹, Dawei Zhang¹, Yingsong Li^{2,3,*}, and Zhixiang Huang^{2,3}

¹College of Information and Communication Engineering
Harbin Engineering University, Harbin, 150001, China

²Key Laboratory of Intelligent Computing and Signal Processing
Ministry of Education, Anhui University, Hefei, 230601, China

*liyingsong@ieee.org

³Anhui Province Key Laboratory of Target Recognition and Feature Extraction
LuAn, 230088, China

Abstract – In this paper, a super-broadband (SBB) rectifier using a wideband resistance compression network (WRCN) and harmonic cycling is proposed, simulated, fabricated, measured and analyzed in detail for the harvesting of ambient radio frequency (RF) energy. Meanwhile, impedance compression and matching are achieved to implement the SBB using WRCN and impedance operation networks. Additionally, harmonic cycling structure and bending technology are employed to improve the power conversion efficiency (PCE) and reduce the size, respectively. For demonstration, a prototype of the proposed rectifier is fabricated and measured. The measured results are in good accordance with the simulated ones, indicating that the rectifier can provide high efficiency and ultra-broadband rectification characteristics. A PCE over 50% is realized at 3.5 GHz with an input power range of 6–24 dBm, and a PCE of 75% is obtained at an input power of 18 dBm. The PCE is greater than 50% at 17 dBm with an input frequency of 2.7–4.6 GHz. This work can find significant applications in the development of RF-harvesting.

Index Terms – bending technique, harmonic cycling, RF-harvest, super-Broadband rectifier, wide-band resistance compression technique.

I. INTRODUCTION

With the rapid development of communication technologies, human beings' living surroundings are full of electromagnetic waves. If these electromagnetic energies can be recycled and harvested on the spot, we can get rid of the limitation that their batteries determine the lifetime of electronic devices. Consequently, radio frequency (RF)-harvest is currently attracting much

attention in scientific and industrial fields. Various RF-harvest devices are currently used in the medical field, smart homes, electric vehicles, consumer electronics, and drone charging [1]. Many rectifiers can now achieve high power conversion efficiency (PCE) in narrow band ranges. However, with the rise of 5G and Internet of Things (IoT) technologies and MIMO radars [2], wider bands are being used for wireless communications where the electromagnetic energy is distributed across multiple bands. Therefore, it is becoming increasingly important to design broadband rectifiers to maximize the amount of power that can be harvested [3, 4].

A lot of rectifiers have been reported to address these mentioned problems. A rectifier consisting of a two-stage coupler is proposed and discussed in [5], which allows the reflected power caused by impedance mismatch to be re-rectified, improving the rectification efficiency, and a fractional bandwidth of 21.5% and a PCE over 70% have been achieved from 2.08 GHz to 2.58 GHz. The rectifier in [6] uses a non-uniform transmission line to achieve broadband rectification characteristics, resulting in a PCE higher than 50% over a bandwidth of 0.4–1 GHz. In [7], a two-stage impedance matching network was used to achieve a PCE greater than 50% with a fractional bandwidth over 37% (1.8–2.72 GHz). In [8], by using a taper impedance matching network, a broadband rectifier is achieved over 2–3.05 GHz with an input power of 10 dBm, and a peak PCE of 75.8% is obtained at an input power of 14 dBm. There are other methods to increase the operating bandwidth of rectifiers by using sub-rectifiers operating in a different band range [9, 10]. In addition, the PCE can be improved by increasing the matching quality using varactor diodes and

MOSFETs given in [10, 11]. However, it is still a great challenge to design rectifiers to cover multiple frequency bands.

This paper proposes an ultra-broadband rectifier with a wideband resistance compression network (WRCN) and harmonic cycling for RF-harvesting to address this issue. Two branches are connected using WRCN to achieve wideband impedance matching. The PCE of the rectifier is further improved with broadband, and a harmonic cycling technique is considered to achieve a broadband high-efficiency rectifier. The proposed rectifier is designed to get a PCE greater than 50% at an input power of 17 dBm from 2.7 to 4.6 GHz, which has a fractional bandwidth over 65% and provides a peak PCE up to 75% at 3.5 GHz with an input power of 18 dBm.

II. THEORETICAL ANALYSIS OF THE RECTIFIER

Figure 1 is the schematic diagram of the designed super-broadband (SBB) rectifier for RF energy harvesting applications using WRCN and harmonic cycling. The SBB rectifier circuit consists of two load resistors, a DC-pass filter (part A), two HSMS286C Schottky diodes, an impedance operating network (part B) and a wideband WRCN (part C).

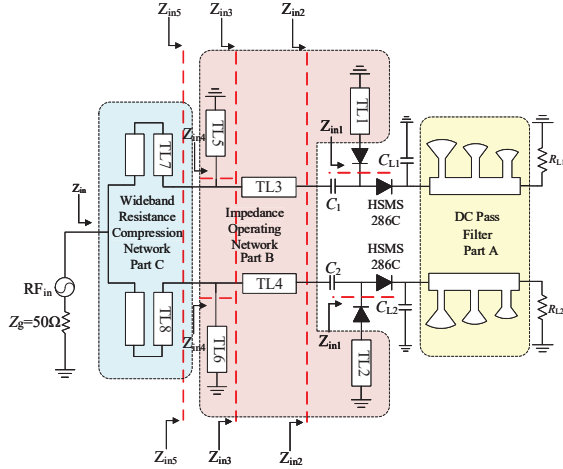


Fig. 1. Schematic of the proposed super-broadband rectifier.

A. Design of the DC-pass filter and harmonic cycling

Since the Schottky diode is a non-linear component, it would generate fundamental frequency and high harmonics in the process of converting the RF signal to DC signal, while the high harmonics are mainly dominated by the second harmonic, and the rest of the high harmonics carry too little energy that can be negligible. In order to make the output voltage more stable, DC-pass filters

combine lumped and distributed elements in this design, which is to smooth the output DC waveform and return the fundamental and higher harmonics to the Schottky diode for re-rectification.

The harmonic cycling structure in the proposed broadband rectifier consists of three linear microstrip stubs and three fan-shaped microstrip stubs. As depicted in Fig. 2, a fan-shaped stub has two characteristic parameters: the radius r_1 and the angle α . The input impedance of the fan-shaped stub can be calculated from equations (1), (2), (3) and (4) [12]:

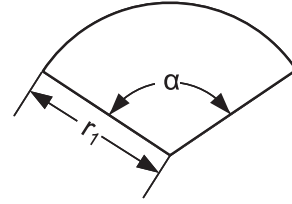


Fig. 2. Characteristic parameters of the fan-shaped stub.

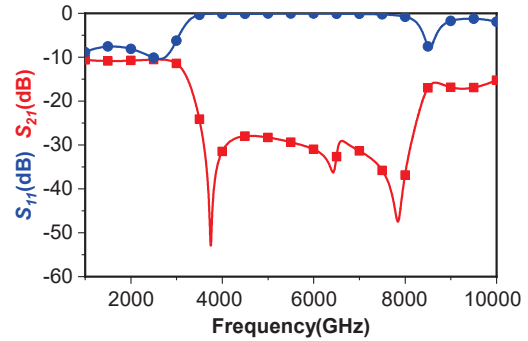


Fig. 3. The simulated S-parameters of harmonic cycling.

$$X_1 = \frac{h}{2\pi r_1} Z_0(r_1) \frac{360 \cos(\theta_1 - \varphi_2)}{a \sin(\varphi_1 - \varphi_2)}, \quad (1)$$

$$\tan \theta_1 = \frac{N_0(kr_1)}{J_0(kr_1)}, \tan \varphi_1 = \frac{J_1(kr_1)}{N_1(kr_1)}, (i = 1, 2), \quad (2)$$

$$Z_0(r_1) = \frac{120\pi [J_0^2(kr_1) + N_0^2(kr_1)]^{\frac{1}{2}}}{\sqrt{\epsilon_r} [J_1^2(kr_1) + N_1^2(kr_1)]^{\frac{1}{2}}}, \quad (3)$$

$$k = \frac{2\pi\sqrt{\epsilon_{re}}}{\lambda_0}, \quad (4)$$

where $J_0(x)$, $N_0(x)$, $J_1(x)$, $N_1(x)$ represent the first class of 0-order Bessel function, the second class of 0-order Bessel function, the first class of 1-order Bessel function and the second class of 1-order Bessel function, respectively. λ_0 denotes the wavelength in free space, ϵ_{re} is the

equivalent dielectric constant, and h is the thickness of the dielectric substrate. In addition, the resonance point of the input impedance of the fan-shaped stub is less affected by frequency variations than that of the linear stub. Thus, the smoother return loss S_{11} curve of the fan-shaped stub provides a broader bandwidth, which also exhibits a wider stop band in the DC-pass filter. Here, the DC-pass filter mainly consists of fan-shaped stubs and linear stubs, with the fan-shaped stubs to reduce the longitudinal size and the linear stubs to avoid the problem of the excessive transverse size of the fan-shaped stubs. The S-parameter is presented in Fig. 3, showing that the designed DC-pass filter can suppress the fundamental and higher harmonics of the RF signal and ensure a smooth DC output.

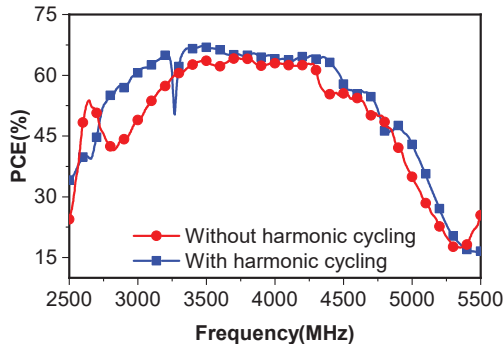


Fig. 4. Comparison of the PCE with and without the harmonic cycling structure.

A comparison of the PCE with and without harmonic loop structure at an input power of 15 dBm is shown in Fig. 4, where the DC-pass filter can recover fundamental and second harmonics over a wide frequency range and improve the PCE. Furthermore, since the filter will be integrated into the circuit, there will be inevitable interactions with the other structures. Therefore, the parameters of the DC-pass filter structure should be adjusted to be optimal for the entire rectifier circuit design.

B. Design of an impedance operation network (ION)

In this design, an ION is used to convert the complex impedance Z_{in1} into a wide resistance Z_{in3} . The upper and lower branches in the ION have the same structures, which both consists of two short-circuit stubs TL1 (TL2), TL5 (TL6) and a section of microstrip transmission line TL3 (or TL4). Thus, the upper branch is used as an example to discuss the operating principle and parameters in this section.

Firstly, the upper branch of the ION consists of two short-circuit stubs TL1, TL5 and a section of microstrip transmission line TL3, where TL1 is mainly to counteract the capacitive characteristics carried by parallel

branch diodes. Since the diode is mainly capacitive in its operating range, TL1 is used as a short-circuit inductor to compensate for the capacitive characteristics of the diode in the operating band by connecting the inductive and capacitive in series. The characteristic impedance and electrical length of TL1 are Z_1 and θ_1 , respectively. The input impedance of the diode in parallel is denoted as $Z_{d1}=R_{d1}+jX_{d1}$. Then, the input impedance of the branch after series connection with TL1 can be described as:

$$Z_{in1}(f) = R_d + jX_d + jZ_1 \tan \theta_1. \quad (5)$$

In order to better understand the design, we define the operating band as (f_1, f_2) , where $f_1 < f_2$ and $f_2/f_1=k$, which can be further denoted as $\theta(f_2)=k\theta(f_1)=\theta_1$. Under ideal circumstances, TL1 should compensate for the capacitive characteristic of caused by the diodes in parallel branch with frequency ranging from f_1 to f_2 , and hence, the characteristic impedance and electrical length of TL1 for a specific power can be calculated using:

$$\text{Im}(Z_{in1}(f_1)) = -\text{Im}(Z_{in1}(f_2)). \quad (6)$$

The TL1 can reduce the input impedance variation of the two diodes in the operating bandwidth and provide a basis for further impedance compression. The diode used in this design is the HSMS286C, and we integrate two diodes into one package. After optimization in Advanced Design Simulation (ADS) with Harmonic Balance Simulation (HB), the characteristic impedance and electrical lengths of TL1(TL2) is calculated at 3.5 GHz to be $Z_1=81 \Omega$, $\theta_1=41.2$ deg. At an input power of 17 dBm, the input impedance Z_{in1} is shown in Fig. 5 after using the series short-circuit stub TL1(TL2), which is equivalent to an inductor, to cancel the diode capacitance.

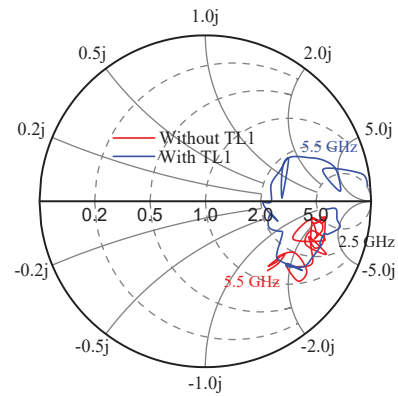


Fig. 5. Comparison of with and without TL1.

Secondly, the microstrip transmission line TL3 has the role of adjusting the imaginary part of the rectifier's input impedance Z_{in2} after TL1. To calculate the characteristic impedance Z_3 and electrical length θ_3 of

the series microstrip transmission line TL3, the rectifier initial input impedance at f_1 and f_2 is expressed as $Z_{in2}(f_1)=R_{d11}+jX_{d11}$ and $Z_{in2}(f_2)=R_{d22}+jX_{d22}$. Then, the rectifier input impedance at f_1 and f_2 after TL3 can be obtained and is given by equations (7) and (8):

$$Z_{in3}(f_1) = Z_3 \frac{Z_{in2}(f_1) + jZ_3 \tan \theta_3(f_1)}{Z_3 + j(Z_{in2}(f_1)) \tan \theta_3(f_1)}, \quad (7)$$

$$Z_{in3}(f_2) = Z_3 \frac{Z_{in2}(f_2) + jZ_3 \tan \theta_3(f_2)}{Z_3 + j(Z_{in2}(f_2)) \tan \theta_3(f_2)}. \quad (8)$$

The characteristic impedance and electrical length of TL3(TL4) were calculated to be $Z_4=77 \Omega$, $\theta_3=153$ deg at 3.5 GHz. $Z_{in2}(f_1)$ and $Z_{in2}(f_2)$ in the equations can be obtained using ADS simulation. Figure 6 shows the input impedance Z_{in3} of the rectifier in the 2.5–5.5 GHz band. It is observed that at an input power of 17 dBm, the real part of Z_{in3} in the frequency band of interest is approximately 39–50 Ω , and the imaginary part nearly oddly symmetrical about the 3.5 GHz frequency. In addition, a bending technique has been adopted in this design, which greatly reduces the space occupied by the TL3, saving space and reducing manufacturing costs.

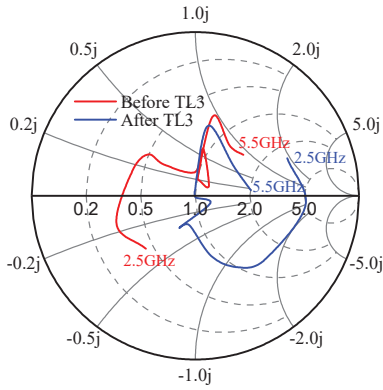


Fig. 6. Comparison of before and after TL3.

Thirdly, the input impedance of the rectifier is further compressed by TL5, which compresses the complex impedance into a wide resistance. Calculating the electrical length θ_5 and characteristic impedance Z_5 of TL5, the inductance of the rectifier input impedance Z_{in3} at f_1 and f_2 is expressed as $G_{in3}-jB_{in3}$, $G_{in3}+jB_{in3}$, respectively. Then, the inductance at f_1 and f_2 after TL5 is expressed as:

$$Y_{in4}(f_1) = \frac{1}{jZ_5 \tan \theta_5} = jB_{in3}, \quad (9)$$

$$Y_{in4}(f_2) = \frac{1}{jZ_5 \tan \theta_5} = -jB_{in3}. \quad (10)$$

The characteristic impedance and electrical length of TL5(TL6) were calculated to be $Z_4=77 \Omega$, $\theta_3=79.7$ deg at 3.5 GHz. Combining the two above equations gives the characteristic impedance and electrical

length of TL5. Further compression is applied to the input impedance to get oddly symmetric about the resistance axis. Compared to the graph before compression, the compressed input impedance only varies around the resistive axis of the Smith chart. It is worth noting that the proposed ION can also work over a wide range of input powers since the input impedance of a Schottky diode rectifier varies with the input power and has a similar trend in the bandwidth.

C. Design of a WRCN

In this section, a WRCN is used to achieve impedance matching of the rectifier over broadband. The precondition for using WRCN is that the rectifier should have two branches. The principle behind it lies in the use of two transmission lines with electrical lengths of $90^\circ+\Delta\theta$ and $90^\circ-\Delta\theta$, respectively, which can reduce the fluctuation of the input impedance due to load changes when it is connected in parallel. Compared to impedance compression networks, RCN requires additional ION, and impedance manipulation networks can transform complex impedances into wide resistances over a wide frequency range to a more stable achieve impedance matching over broadband.

The idea of designing the WRCN is presented as follows. Firstly, the WRCN should provide a resistor in the broadband, which is obtained from the previous ION analysis. For a conventional microstrip linear resistive compression network, it is difficult for the two branches to maintain complementary electrical lengths in the broadband, which can be well solved by using a double coupled line. Let the coupled line TL7 have an even-mode (odd-mode) characteristic impedance of Z_e (Z_o) and an electrical length of θ_{c1} at f_1 and θ_{c1} at f_2 . Regarding the coupled line as a section of the transmission line, the characteristic impedance of this transmission line is Z_{eq} , while the electrical lengths at f_1 and f_2 are θ_{eq1} and θ_{eq2} , respectively. To achieve complementarity of electrical lengths, θ_{eq1} and θ_{eq2} should satisfy:

$$\theta_{eq1} + \theta_{eq2} = 180^\circ. \quad (11)$$

Then, the ABCD transmission matrix of the coupled line at f_1 is modeled as equations (12), (13) and (14):

$$\frac{Z_e - Z_o \tan^2 \theta_{c1}}{Z_e + Z_o \tan^2 \theta_{c1}} = \cos \theta_{eq1}, \quad (12)$$

$$\frac{2Z_e Z_o j \tan \theta_{c1}}{Z_e + Z_o \tan^2 \theta_{c1}} = jZ_{eq} \sin \theta_{eq1}, \quad (13)$$

$$\frac{2j \tan \theta_{c1}}{Z_e + Z_o \tan^2 \theta_{c1}} = j \frac{\sin \theta_{eq1}}{Z_{eq}}. \quad (14)$$

Similarly, the equivalent ABCD transmission matrix of the coupling line at f_2 can be obtained. The characteristic impedance and electrical lengths for the coupled line can be calculated using the above four equations, where the electrical lengths operating at f_1 and f_2 have a

relationship of $\theta_{c2}=k\times\theta_{c1}$. The characteristic impedance and electrical length for TL6 can be obtained using the same analysis, except that the equivalent electrical length of TL6 at f_1 is θ_{eq2} that equals to $(180^\circ-\theta_{eq1})$, and the equivalent electrical length at f_2 is θ_{eq1} . In addition, the parallel impedance of the two branches is 50Ω , which matches the source impedance.

III. IMPLEMENTATION AND MEASUREMENT RESULTS

Based on the above principle analysis, the layout of the proposed rectifier is modelled in ADS and jointly optimized, which is shown in Fig. 7. The rectifier is printed on a F4B ($\epsilon_{re}=2.55$, $\tan\delta=0.002$) dielectric substrate with thickness of $h=0.762\text{ mm}$ and a total size of $94\times 60\text{ mm}^2$. Herein, two HSMS2862C are used as rectifier diodes, and the capacitors are all Murata's GRM18 series 100 pf capacitors, and the load resistance is 650Ω . To facilitate adjustment, two experimental resistor boxes are used in the test. Alternatively, if it was preferred to use only one load, the resistance value of the replacement load should be twice the resistance value of the initial load, and the PCE would remain almost unchanged.

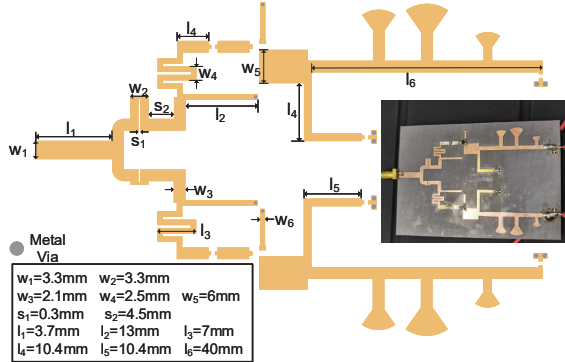


Fig. 7. Layout of the proposed rectifier.

In the experiment, an Agilent PNA-X vector network analyzer is used as a signal source, two adjustable resistor boxes are used as load resistors, and a multimeter is used to measure the output voltage. The proposed ultra-broadband rectifier is analyzed, fabricated and tested. Figure 8 gives a comparison of the simulated S_{11} of the proposed rectifier with the measured results at an input power of 17 dBm, showing that the rectifier has a good broadband characteristic. Herein, the PCE is calculated using equation (15) [13, 14]:

$$PCE(\%) = \frac{P_{DC}}{P_{RF}} = \frac{V_{out1}^2 + V_{out2}^2}{R_L \cdot P_{RF}}. \quad (15)$$

Figure 9 presents the simulated PCE versus measured PCE for input powers at 5 dBm, 10 dBm, 17 dBm, 20 dBm, respectively. From the results, we found that

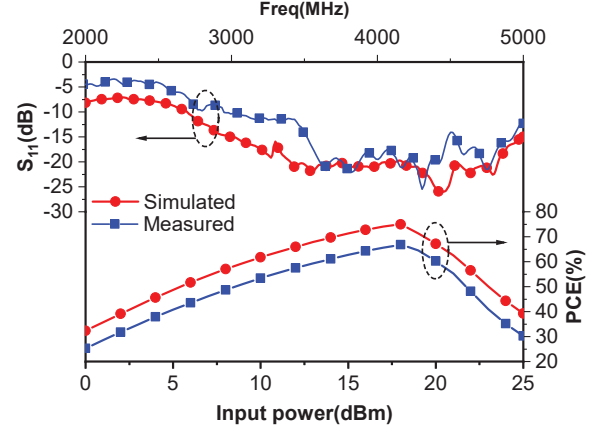


Fig. 8. (Upper lines) Measured and simulated S_{11} of the rectifier. (Lower lines) Measured and simulated PCE versus input power at 3.5 GHz.

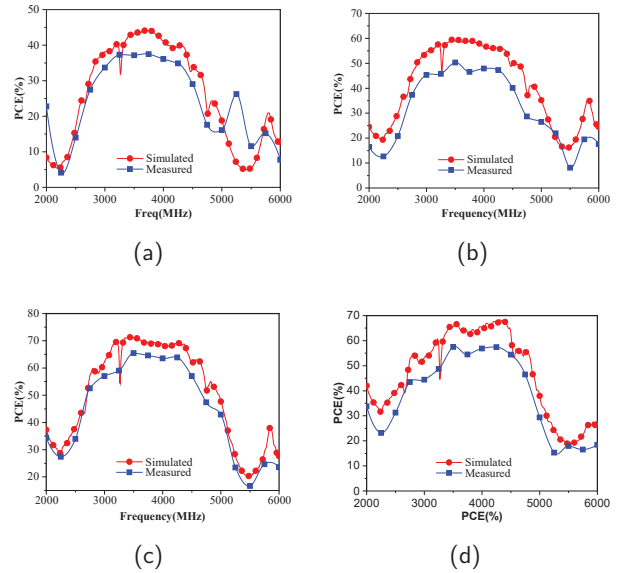


Fig. 9. Measured and simulated PCE variations at different input power levels (a) 5 dBm, (b) 10 dBm, (c) 17 dBm, and (d) 20 dBm.

Table 1: Comparison between the suggested rectifier and related designs

Ref.	Freq.(GHz)	FBW.	Max-PCE	Size(mm^2)
[5]	2.08–2.58	20.8%	80.8%	126×68
[8]	2–3.05	41.5%	75.8%	—
[15]	0.915	—	74.2%	—
[16]	1.7–2.9	50%	76%	56×36
This work	2.7–4.6	52%	75%	94×60

there is a maximum band range of 2.7–5 GHz at an input power of 17 dBm with $PCE > 50\%$.

Figure 8 shows the simulated and measured PCE variation with input power at a frequency of 3.5 GHz. We can see that the maximum conversion efficiency of 77% is obtained when the input power is 19 dBm, and a PCE > 50% is achieved with an input power of 6-24 dBm. Table 1 shows a comparison between the proposed rectifier and some previous similar works. The proposed rectifier has the widest bandwidth and balanced PCE. The difference between the experimental and simulated results is mainly caused by soldering errors and insertion losses of the SMA connectors.

IV. CONCLUSION

A super-broadband rectifier using a WRCN and harmonic cycling is proposed for RF-harvesting. Impedance matching over a wide bandwidth is achieved by using an impedance operation network consisting of three microstrip lines and a WRCN designed via coupled lines. The harmonic cycling structure further improves the PCE of the rectifier, while the bending technique is used to reduce the size of the rectifier. The proposed rectifier achieves a PCE over 50% from 2.7-4.6 GHz at an input power of 17 dBm, and the designed rectifier has a fractional bandwidth of over 50%. The techniques described in this work can also apply to other rectifier circuits.

REFERENCES

- [1] X. Sun, C. Liu, Y.-D. Chen, J. Jing, Z. He, and P. Wu, "Low-power wireless uplink utilizing harmonic with an integrated rectifier-transmitter," *IEEE Microw. Wirel. Compon. Lett.*, vol. 31, no. 2, pp. 200-203, Feb. 2021.
- [2] W. Shi, X. Liu, and Y. Li, "ULA fitting for MIMO radar," *IEEE Comm. Lett.*, vol. 26, no. 9, pp. 2190-2194, Sep. 2022.
- [3] W. Liu, K. Huang, T. Wang, Z. Zhang, and J. Hou, "A broadband high-efficiency RF rectifier for ambient RF energy harvesting," *IEEE Microw. Wirel. Compon. Lett.*, vol. 30, no. 12, pp. 1185-1188, Dec. 2020.
- [4] X. Liu, D. W. Zhang, Y. Li, and T. Jiang, "Low power broadband rectifier with wide dynamic input power range for RF-harvesting," *IEEE AP-S/URSI*, Denver, USA, 2022.
- [5] X. Y. Zhang, Z. Du, and Q. Xue, "High-efficiency broadband rectifier with wide ranges of input power and output load based on branch-line coupler," *IEEE Trans. Circuits Syst. I-Regul. Pap.*, vol. 64, no. 3, pp. 731-739, Mar. 2017.
- [6] H. Sakaki and K. Nishikawa, "Broadband rectifier design based on quality factor of input matching circuit," *Proc. Asia-Pacific Microw. Conf.*, Sendai, Japan, pp. 1205-1207, Nov. 2014.
- [7] C. Song, Y. Huang, P. Carter, J. Zhou, S. Yuan, Q. Xu, and M. Kod, "A novel six-band dual CP rectenna using improved impedance matching technique for ambient RF energy harvesting," *IEEE Trans. Antennas Propag.*, vol. 64, no. 7, pp. 3160-3171, Jul. 2016.
- [8] P. Wu, S. Y. Huang, W. Zhou, W. Yu, Z. Liu, X. Chen, and C. Liu, "Compact high-efficiency broadband rectifier with multi-stage-transmission-line matching," *IEEE Trans. Circuits Syst. II: Express Briefs*, vol. 66, no. 8, pp. 1316-1320, Aug. 2019.
- [9] C. Li and T. Lee, "2.4-GHz high-efficiency adaptive power," *IEEE Trans. Very Large Scale Integr. (VLSI) Syst.*, vol. 22, no. 2, pp. 434-438, Feb. 2014.
- [10] V. Marian, B. Allard, C. Vollaïre, and J. Verdier, "Strategy for microwave energy harvesting from ambient field or a feeding source," *IEEE Trans. Power Electron.*, vol. 27, no. 11, pp. 4481-4491, Nov. 2012.
- [11] Z. Liu, Z. Zhong, and Y. Guo, "Enhanced dual-band ambient RF energy harvesting with ultra-wide power range," *IEEE Microw. Wirel. Compon. Lett.*, vol. 25, no. 9, pp. 630-632, Sep. 2015.
- [12] S. L. March, "Analyzing lossy radial-line stubs (short papers)," *IEEE Trans. Microw. Theory Tech.*, vol. 33, no. 3, pp. 269-271, Mar. 1985.
- [13] J. Kim and J. Oh, "Compact rectifier array with wide input power and frequency ranges based on adaptive power distribution," *IEEE Microw. Wirel. Compon. Lett.*, vol. 31, no. 5, pp. 513-516, May 2021.
- [14] W. Liu, K. Huang, T. Wang, J. Hou, and Z. Zhang, "A compact high-efficiency RF rectifier with widen bandwidth," *IEEE Microw. Wirel. Compon. Lett.*, vol. 32, no. 1, pp. 84-87, Jan. 2022.
- [15] G. Song, X. Liu, and C. Liu, "Wide-range rectifier for wireless power transfer based on power compensation," *IEEE Microw. Wirel. Compon. Lett.*, vol. 31, no. 5, pp. 509-512, May 2021.
- [16] Z. Du, S. F. Bo, Y. F. Cao, J. Ou, and X. Y. Zhang, "Broadband circularly polarized rectenna with wide dynamic-power-range for efficient wireless power transfer," *IEEE Access*, vol. 8, pp. 80561-80571, Apr. 2020.



Xin Liu was born in Gansu, China. He received the B.S. degree in Optoelectronic Information Science and Engineering from the North University of China, Shanxi, China, in 2019. He is currently pursuing the M.S. degree in Electronics Information with the Harbin Engineering University, China. His current research interests include RF circuit design, antenna design, wireless power transmission.



Dawei Zhang received the B.S. and M.S. degree from the University of Electronic Science and Technology of China, Chengdu, China, in 2011 and 2014, respectively, and the Ph.D. degree from Harbin Institute of Technology, Harbin, China, in 2019.

In 2019, he joined the College of Information and Communication Engineering, Harbin Engineering University, as an assistant professor. His current research interests include metamaterials and spoof surface plasmon polaritons.



Yingsong Li received his B.S. degree in Electrical and Information Engineering, and M.S. degree in Electromagnetic Field and Microwave Technology from Harbin Engineering University, 2006 and 2011, respectively. He received his Ph.D degree from

both Kochi University of Technology (KUT), Japan and Harbin Engineering University (HEU), China in 2014. He is currently a Full Professor with the School of Electronic and Information Engineering of Anhui University from March 2022. He was a full Professor in Harbin Engineering University from 2014 to 2022 and a visiting scholar of University of California, Davis from March 2016 to March 2017, a visiting Professor of University of York, UK in 2018, a visiting Professor of Far Eastern Federal University (FEFU) and KUT. Now, he holds the visiting professor position of School of Information of KUT from 2018. He is a Postdoc of Key Laboratory of Microwave Remote Sensing, Chinese Academy of Sciences from 2016 to 2021. Now, He is a Fellow of Applied computational Electromagnetics Society (ACES Fellow), and he is also a senior member of Chinese Institute of Electronics (CIE) and IEEE. He has authored and coauthored about 300 journal and conference papers in various areas of electrical and information engineering. His current research interests include signal processing, adaptive filters, metasurface designs and microwave antennas.

Dr. Li serves as an Area Editor of AEU-International Journal of Electronics and Communications from 2017 to 2020, and he is an Associate Editor of IEEE Access, Applied Computational Electromagnetics Society Journal (ACES Journal) and Alexandria Engineering Journal and Electromagnetic Science. He is the TPC Co-Chair of the 2019 IEEE International Workshop on Electromagnetics (iWEM 2019-2020), 2019 IEEE 2nd International Conference on Electronic Information

and Communication Technology (ICEICT 2019), 2019 International Applied Computational Electromagnetics Society (ACES) Symposium-China, 2019 Cross Strait Quad-regional Radio Science and Wireless Technology Conference (2019 CSQRWC) and TPC Chair of ICEICT 2021-2022. He is also a General Co-Chair of ICEICT 2020 and a General Chair of IEEE 9th International Conference on Computer Science and Network Technology (ICCSNT 2021) and ICCSNT 2022. He is also a TCP member for many international and domestic conference. He also serves as a Session Chair or Organizer for many international and domestic conferences, including the WCNC, AP-S, ACES-China ect. He acts as a Reviewer of numerous IEEE, IET, Elsevier and other international journals and conferences.



Zhixiang Huang received his BS degree in Statistic and Probability and Ph.D. in Electromagnetic Field and Microwave Technology from Anhui University in 2002 and 2007, respectively. He is a Lecturer of Anhui University from 2007 to 2008 and is promoted to Professor

in 2008, and is a visiting scholar in Ames Laboratory, Iowa State University, from 2010 to 2011. Currently, he is a full Professor and the dean of the School of Electronic Information Engineering of Anhui University, founder of Key Laboratory of Electromagnetic Environmental Sensing of Anhui Higher Education Institutes, director of the Young Scientists Club of Chinese Institute of Electronics (CIE), member of the Youth Working Committee of CIE. He is the recipient of the Outstanding Young Talent Project of National Natural Science Foundation of China (NSFC) in 2018 and the Chang Jiang Scholars Program of Ministry of Education of the People's Republic of China in 2022. He is a Senior Member of IEEE. He has more than 100 academic papers in peer-reviewed international/national journals. His current interests include theoretical and computational in electromagnetics and Microwave/RF circuit design, and multiphysics modeling.

